

**NOVEL LIQUID CRYSTAL SELF-ASSEMBLY,  
DRIVEN ASSEMBLY, AND SELF-SHAPING  
IN CONFINED ENVIRONMENTS**

Wei-Shao Wei

A DISSERTATION

in

Physics and Astronomy

Presented to the Faculties of the University of Pennsylvania

in

Partial Fulfillment of the Requirements for the  
Degree of Doctor of Philosophy

2020

Supervisor of Dissertation

---

Arjun G. Yodh, Professor of Physics and Astronomy

Graduate Group Chairperson

---

Joshua R. Klein, Professor of Physics and Astronomy

Dissertation Committee

Tom C. Lubensky, Professor of Physics and Astronomy  
Peter J. Collings, Professor of Physics and Astronomy  
Shu Yang, Professor of Materials Science and Engineering  
Gary M. Bernstein, Professor of Physics and Astronomy

**NOVEL LIQUID CRYSTAL SELF-ASSEMBLY, DRIVEN ASSEMBLY,  
AND SELF-SHAPING IN CONFINED ENVIRONMENTS**

© COPYRIGHT

2020

Wei-Shao Wei

This work is licensed under the Creative Commons Attribution  
NonCommercial-ShareAlike 3.0 License

To view a copy of this license, visit

<http://creativecommons.org/licenses/by-nc-sa/3.0/>

*Dedicated to my family.*

## ACKNOWLEDGMENT

It has been a long journey, and I owe a great debt of gratitude to a large number of people. The work could not be done and I would not be where I am today without their constant support.

First and foremost, I am tremendously grateful to my advisor, Arjun Yodh. Arjun has been my ideal mentor, with his expert guidance, strong support, attention to detail, and the lab philosophy he tries to build. Arjun encourages students to invent and explore their own ideas, but meanwhile makes sure we could justify the ideas in detail, with solid and clear thought. This training gave me rare opportunities to devise skills to address various challenges. Arjun also taught me about communication in science, from writing papers to giving talks. With his patient guidance and frank criticism/encouragement, hopefully, I have progressed significantly toward a better scientist.

During my time at Penn, I had the pleasure of collaborating with many talented experts in soft matter, without whom my research would not be possible. I am especially grateful to Kevin Aptowicz, Gary Bernstein, Peter Collings, Remi Dreyfus, Piotr Habdas, Randall Kamien, Tom Lubensky, Kathleen Stebe, and Shu Yang. They provided great insight and amazing suggestions into my various projects. Moreover, I got valuable advices from them regarding my career plan. I was also lucky to work with my incredible labmates and colleagues; I have not only learned much from them but also enjoyed the everyday life I spent with them. They include Daniel Beller, Coline Bretz, Jing Cai, Sanghoon Chong, Alexis de la Cotte, Zoey Davidson, Sophie Ettinger, Mohamed Amine Gharbi, Matthew Gratale, Analisa Hill, Joonwoo Jeong, Louis Kang, Chandan Kumar, Matthew Lohr, Xiaoguang Ma, Angel Martinez, Francesca Serra, Nima Sharifi-Mood, Charlotte Slaughter, Tim Still, Michio Tanaka,

Yuchen Wang, Yu Xia, and Ye Xu. I would also like to thank the staff of the Physics Department, LRSM, and Singh Center for their support throughout my research.

Of course, my journey in the United States would not begin without supports and advices from my previous mentors in Taiwan. First of all, I would like to thank Keng-hui Lin, my previous advisor. She introduced me into the field of soft matter and shaped my taste of research. The valuable experiences in her lab sparked my interest in experimental science and guided me to become a soft matter researcher. I would also like to thank Chun-Che Chang, Cheng-Hsuan Chen, and Wei-Hsin Sun for their warm suggestions about establishing careers in a foreign country.

Finally, my friends and family - especially my parents and my fiancée, Yi-Yun Ho - I really appreciate your company, love, patience, and support beyond all reasonable expectations. Thank you!

# ABSTRACT

## NOVEL LIQUID CRYSTAL SELF-ASSEMBLY, DRIVEN ASSEMBLY, AND SELF-SHAPING IN CONFINED ENVIRONMENTS

Wei-Shao Wei

Arjun G. Yodh

This dissertation describes experiments which explore assembly and self-shaping behavior of liquid crystals (LCs) in confined environments, and characterize colloidal crystals made via LC-mediated defect interactions. Specifically, we report on: (1) LC textures that arise in the spherical-cap like confinement of a Janus drop; (2) assembly and dynamics of two-dimensional colloidal crystals residing atop of a LC surface, and (3) shape transitions of micro-emulsion drops containing LC oligomers.

The first experiments investigated nematic and smectic LCs confined in the spherical-cap like cavities of Janus droplets. We employed solvent-induced phase separation to make the Janus droplets, and we systematically characterized droplet morphologies, which were shown to be sensitive to the compartment volume ratio and the type/concentration of surfactants in the aqueous background phase. A variety of stable and metastable LC textures were found, including focal conic domains, dislocation rings, and layer undulations. Polarized optical microscopy was employed to analyze director configurations and follow their evolution. The lowest free energy state appears to be a lamellar layered structure with dislocation rings relaxed by smectic layer undulations. Novel drop functionalities such as directional self-propelled motion were also reported.

The second set of experiments investigated two-dimensional crystalline packings of colloidal particles residing at the interface between air and a nematic LC; the interparticle interactions were mediated by defects that extended from the particles on

the surface into the bulk LC. The assembly and dynamics of the colloidal lattices were then studied by video microscopy. Specifically, particle motions including short-time diffusion and crystal phonon modes were measured and demonstrated to depend on the underlying LC viscosity and elastic constants. Displacement correlations enabled characterization of transverse and longitudinal sound velocities of the crystal packings, as well as quantification of the particle interactions produced by the LC defects.

The third set of experiments discovered and probed reversible shape transitions of micro-emulsion drops containing nematic liquid crystal oligomers (NLCOs). We reported spontaneous shape transitions of the drop morphology from spheres to roughened spheres, flowers, and filamentous structures. The control parameters dictating final morphologies included temperature, mean oligomer chain length, and surfactant concentration in the aqueous background. Surprisingly, our experiments and modeling suggested that molecular heterogeneity is a key feature leading to chain-length-dependent oligomer segregation within the micro-droplet that drives the observed transitions. Thus polydispersity, in this case, does not destroy order, rather it drives the transitions. In different sets of experiment with the same system, we permanently locked the resultant NLCO structures into liquid crystal elastomers (LCEs) by UV curing. With this process, and especially using the filamentous structures, we made non-woven, free-standing mats and well-aligned yarns. Currently, work is directed toward exploration of photonic and rheological properties of the self-assembled filamentous nematic networks.

# Contents

Acknowledgment . . . . .	iv
Abstract . . . . .	vi
Table of Contents . . . . .	viii
List of Figures . . . . .	xiii
Preface . . . . .	xvii
Chapter 1 : Introduction . . . . .	1
1.1 Small-molecule Thermotropic Liquid Crystals . . . . .	4
1.2 Liquid Crystal Oligomers and Liquid Crystal Elastomers . . . . .	8
1.3 Outline of Subsequent Chapters . . . . .	9
Chapter 2 : Textures in the Liquid Crystal Compartments of Janus Droplets	11
2.1 Introduction . . . . .	11
2.2 Method and Materials . . . . .	13
2.2.1 Preparation of the Liquid Crystal Janus Droplets . . . . .	13
2.2.2 Analysis of Liquid Crystal Configurations and Textures . . . . .	17
2.2.3 Analysis of Janus Droplet Morphologies . . . . .	17
2.3 Properties of the Liquid Crystal Janus Droplets . . . . .	19
2.4 Nematic Liquid Crystal Textures within Janus Droplets . . . . .	21
2.5 Smectic Liquid Crystal Textures within Janus Droplets after Initial Quench . . . . .	23
2.5.1 Focal Conic Domain Flower-like Textures . . . . .	24

2.5.2	Dislocation Ring Textures . . . . .	27
2.5.3	Smectic Layer Undulation Textures . . . . .	28
2.6	Metastable Smectic-A Textures . . . . .	29
2.7	Metastable Smectic-A Textures Evolve after Annealing and Relaxation	32
2.8	More and Different Liquid Crystal Confinement Geometries: Variable Spherical-cap Morphologies and Patchy Droplets . . . . .	35
2.9	Active Liquid Crystal Janus Droplets . . . . .	37
2.10	Summary and Future Directions . . . . .	39
Chapter 3 : Liquid Crystal Properties from Interfacial Colloidal Dynamics .		41
3.1	Introduction . . . . .	41
3.2	Method and Materials . . . . .	43
3.2.1	Preparation of Colloidal Monolayers at Nematic Liquid Crystal Interfaces . . . . .	43
3.2.2	Optical Microscopy and Particle Tracking . . . . .	46
3.2.3	Displacement Covariance Matrix Method . . . . .	47
3.3	Probing Liquid Crystal Viscosity via Short-time Particle Diffusions .	49
3.4	Phonon Density of States and Dispersion Relations . . . . .	53
3.5	Interparticle Interactions in The Crystal . . . . .	56
3.6	Interparticle Interactions as a Function of Temperature & Liquid Crys- tal Elastic Constant . . . . .	59
3.7	Particle-free Domains and Silica Micro-cubes at Nematic Liquid Crys- tal Interface . . . . .	63
3.8	Summary and Future Directions . . . . .	65
Chapter 4 : Self-shaping Liquid Crystal Micro-emulsions . . . . .		69
4.1	Introduction . . . . .	69

4.2	Method and Materials . . . . .	71
4.2.1	Synthesis of Nematic Liquid Crystal Oligomer Drops . . . . .	71
4.2.2	Drop Morphology Characterization . . . . .	75
4.2.3	Molecular Weight Measurements of Liquid Crystal Oligomers . . . . .	75
4.2.4	Macroscopic Interfacial Tension Measurements . . . . .	76
4.3	Reversible Drop Shape Transition via Temperature Cycling . . . . .	77
4.4	Equilibrium Drop Morphologies as a Function of Mean Oligomer Chain Length and Surfactant Concentration . . . . .	80
4.5	Director Configurations within Spherical and Filamentous Structures . . . . .	83
4.6	Heterogeneity and Chain-length-dependent Oligomer Segregation Drive Drop Shape Transitions . . . . .	85
4.6.1	System Free Energy for Nematic Liquid Crystal Oligomer Drops & Filaments . . . . .	86
4.6.2	Criteria for Drop Shape Transitions Predicted by The Homogeneous Model . . . . .	89
4.6.3	Criteria for Drop Shape Transitions Predicted by The Heterogeneous Model . . . . .	91
4.6.4	Macromer–monomer Mixing Experiments . . . . .	93
4.6.5	Polydispersity and Oligomer Segregation Reduce Interfacial Tension and Facilitate Drop Shape Transitions . . . . .	96
4.7	Analogue in Biological Matter: Polydispersity and Phase-separation Drive Surface Patterning . . . . .	99
4.8	Summary and Future Directions . . . . .	100
Chapter 5 : Liquid Crystal Elastomers from Flower-like and Filamentous Drops		102
5.1	Introduction . . . . .	102

5.2	Method and Materials . . . . .	103
5.2.1	Crosslinking the Nematic Liquid Crystal Oligomer Structures to Make Nematic Liquid Crystal Elastomer Structures . . . . .	104
5.2.2	Cholesteric Nematic Liquid Crystal Oligomer / Elastomer Structures . . . . .	105
5.2.3	Laser Dye Doped Nematic Liquid Crystal Elastomer Filamentous Networks . . . . .	105
5.2.4	Quantum Dot Doped Nematic Liquid Crystal Elastomer Filamentous Networks . . . . .	105
5.2.5	Gold Nanorods Doped Nematic Liquid Crystal Oligomer & Elastomer Filamentous Networks . . . . .	106
5.3	Self-assembled Nematic Liquid Crystal Elastomer Constructions with Desired Morphology . . . . .	106
5.4	Programmable Surface Patterning with Chiral Dopants . . . . .	110
5.5	Photonics in Nematic Filamentous Networks & Fibrous Nematic - Quantum Dot Composites . . . . .	117
5.6	Fibrous Nematic-Gold Nanorod Composites . . . . .	119
5.7	Summary and Future Directions . . . . .	121
Chapter 6 :	Conclusion and Future Directions . . . . .	124
6.1	Textures of Confined Liquid Crystals: Interplay between Elasticity, Surface Anchoring, and Boundary Geometry . . . . .	124
6.2	Self-assembled Colloidal Packings: Interactions Mediated by Topological Defects in Liquid Crystals . . . . .	126
6.3	Shape Transitions of Liquid Crystal Micro-emulsions: Competition between Elasticity and Interfacial Tension . . . . .	127

6.4 Functionalities of Liquid Crystal Templated Composites . . . . .	129
Bibliography . . . . .	131

# List of Figures

Figure 1 :	Molecular arrangement in the isotropic, nematic, and smectic-A phase. . . . .	5
Figure 2 :	Possible nematic and smectic-A configurations in spherical confinement. . . . .	7
Figure 3 :	Main-chain liquid crystal oligomers. . . . .	9
Figure 4 :	Preparation of liquid crystal Janus droplets via solvent-induced phase separation. . . . .	15
Figure 5 :	Morphology profiles of the liquid crystal Janus droplets. . . . .	18
Figure 6 :	Nematic textures within Janus droplets. . . . .	22
Figure 7 :	Smectic-A textures within Janus droplets: focal conic, dislocation ring, and undulation textures. . . . .	25
Figure 8 :	Focal conic textures within Janus droplets at high SDS concentration. . . . .	27
Figure 9 :	Occurrence of different SmA textures with respect to drop size & their evolution after the quench, after annealing, and after annealing/relaxation. . . . .	30
Figure 10 :	Cavity morphologies and interfacial tensions for Janus drops containing different SmA textures after the first quench and after annealing. . . . .	32
Figure 11 :	SmA texture evolution/transition during thermal annealing and relaxation. . . . .	33
Figure 12 :	Control Janus droplet morphology with different surfactants and compartment volume ratio. . . . .	36

Figure 13 : Patchy liquid crystal droplets. . . . .	36
Figure 14 : Self-propelled motion of the nematic liquid crystal Janus droplets.	38
Figure 15 : Hexagonal colloidal lattices at the nematic-air interface. . . . .	44
Figure 16 : Hexagonal colloidal lattices melt upon nematic-isotropic phase transition. . . . .	46
Figure 17 : Short-time diffusion behavior of colloidal particles at the nematic interface. . . . .	50
Figure 18 : Vibrational density of states and dispersion relations of the colloidal packings. . . . .	54
Figure 19 : Dispersion relations and sound velocities of the colloidal packings.	55
Figure 20 : Effective spring constant with respect to interparticle separation.	59
Figure 21 : Effective spring constant and stress as functions of temperature.	60
Figure 22 : Correlation between effective spring constant and liquid crystal elastic constant. . . . .	62
Figure 23 : Hexagonal particle-free region within the 2D colloidal particle lattice packings. . . . .	64
Figure 24 : Packings of silica colloidal cubes at the nematic-air interface. . . . .	64
Figure 25 : Temperature dependence of the phonon behavior. . . . .	67
Figure 26 : Schematics of nematic liquid crystal oligomer drop and filament suspended in water solution. . . . .	72
Figure 27 : Chain length (molecular weight) distribution of nematic liquid crystal oligomer samples measured by size exclusion chromatography (SEC). . . . .	73
Figure 28 : Spontaneous shape transition of nematic liquid crystal oligomer drops. . . . .	77

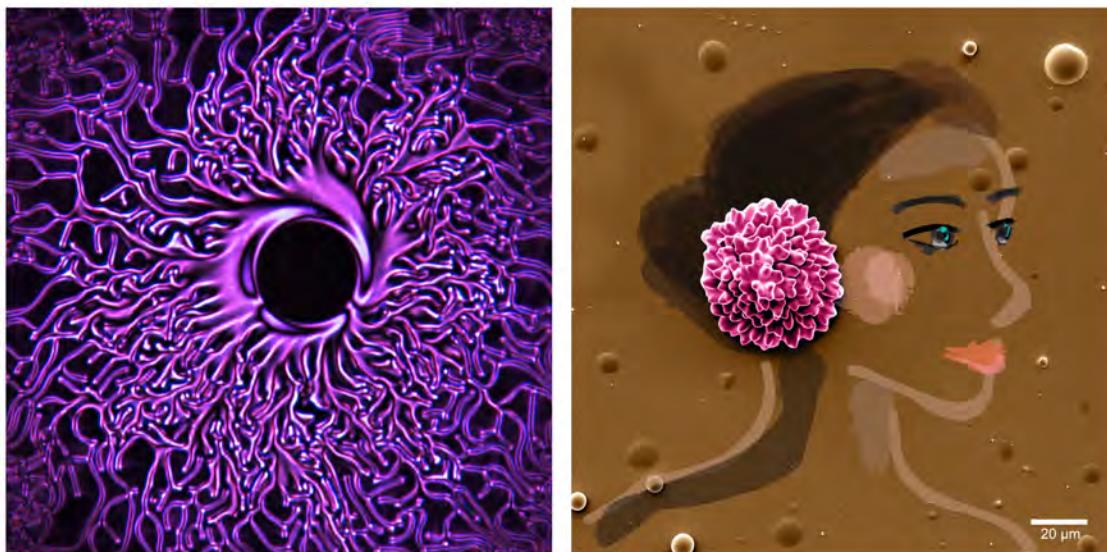
Figure 29 : Reversible shape transitions of nematic liquid crystal oligomer drops during temperature cycling. . . . .	78
Figure 30 : Macroscopic interfacial tension of nematic liquid crystal oligomer pendant drops as function of temperature and oligomerization time (oligomer mean chain length). . . . .	79
Figure 31 : Equilibrium nematic liquid crystal oligomer drop morphologies as function of mean oligomer chain length and surfactant concentration. . . . .	81
Figure 32 : Nematic liquid crystal oligomer structures in aqueous solutions of different surfactants as a function of the mean oligomer chain length, $\langle \ell \rangle$ . . . . .	82
Figure 33 : Aggregated nematic liquid crystal oligomer filamentous structures for SDS concentrations above critical micelle concentration. . . . .	83
Figure 34 : Director configurations within nematic liquid crystal oligomer structures. . . . .	84
Figure 35 : Range of required interfacial tension reduction needed for spontaneous shape transitions of NLCO drops with “physical” saddle-splay modulus. . . . .	91
Figure 36 : Drop morphologies obtained from mixtures of macromers ( $\langle \ell \rangle \approx 9$ ) and monomers (RM82) at different weight ratios in a 0.1 wt% SDS aqueous solution after cooling. . . . .	95
Figure 37 : Well-maintained morphology and director configuration during crosslinking of nematic liquid crystal oligomer structures into nematic liquid crystal elastomers. . . . .	107

Figure 38 : Self-assembled nematic liquid crystal elastomer structures as a function of mean oligomer chain length within drops. . . . .	108
Figure 39 : Self-assembled nematic liquid crystal elastomer fibrous mat. . . . .	109
Figure 40 : Oriented nematic liquid crystal elastomer fiber yarn. . . . .	109
Figure 41 : Cholesteric nematic liquid crystal oligomer drops with spiralling subsurface disclinations. . . . .	112
Figure 42 : Surface grooves associated with subsurface disclinations on cholesteric nematic liquid crystal elastomer spheres. . . . .	113
Figure 43 : Surface roughening coupled with spatial distribution of underlying disclination loops. . . . .	115
Figure 44 : Coiled filamentous structures formed by cholesteric nematics. . . . .	117
Figure 45 : Gold nanorods with various aspect ratios. . . . .	120
Figure 46 : Gold nanorods doped nematic liquid crystal elastomer structures and UV-VIS-NIR absorption spectra. . . . .	120

## PREFACE

*Per sviluppare una mente completa studia la scienza dell'arte, studia l'arte della scienza. Sviluppa i tuoi sensi, impara soprattutto a vedere. Comprendi che tutto é connesso.*

- Leonardo da Vinci



**'Medusa' shaped droplets containing liquid crystal molecules** (left). Selection of National Science Foundation Multimedia Gallery. Credit: Wei-Shao Wei, Felice Macera, and Arjun G. Yodh.

**Girl with a flower** (right). Winning entries of the 2019 National Nanotechnology Coordinated Infrastructure (NNCI) Image Contest: Most Whimsical. Credit: Wei-Shao Wei, Yi-Yun Ho, and Arjun G. Yodh.

# Chapter 1

## Introduction

Soft materials are of fundamental interest from a physics point-of-view and are important ingredients in a variety of every-day products such as paints and gels, and also for more high-tech applications that arise in 3D-printing, actuation, and display technologies. Broadly, these materials are “soft” when pushed and are known to readily assemble and reconfigure in response to confinement geometry, boundary conditions, and environmental stimuli. Currently the creation of functional soft materials, through careful control of constituent interactions and microstructure, is a hot topic in condensed matter physics. To translate the resulting sophisticated concepts from the research lab into practice, however, a detailed understanding of material spatiotemporal characteristics and material responses at the micro- and nano-scales is needed.

Among the many types of soft materials, liquid crystals (LCs) are well known for their ordered molecular configurations, anisotropic macroscopic properties, and reconfigurability due to temperature-dependent phase transitions and interactions with applied fields (electromagnetic, mechanical, etc.). Consequently, fundamental understanding of LCs is still sought. New understanding of LCs is needed for the display technology industry and other more specialized applications, and new fundamental insights continue to stimulate scientific curiosity in the physics community. To this end, my dissertation aims to expand our basic understanding of LCs through novel experiment and analysis. Besides curiosity-driven exploration, some of the unique features of the LCs we uncover might be applied to create new and potentially useful programmable materials.

The majority of the experiments to be described in this thesis focus on how the character of a LC is influenced by surface anchoring, confinement geometry, and interfacial tension. Balance between surface anchoring and LC elasticity drives assembly of new director configurations in confined geometries with particular boundary conditions on the container surfaces. Competition between interfacial tension and LC elasticity facilitates spontaneous shape transitions of micro-droplets to some truly surprising non-trivial morphologies. Finally, some experiments described in this thesis utilize novel interactions induced by LCs on colloidal particles to drive colloidal particle assembly and dynamics.

For example, we characterize LC textures in the novel spherical-cap confinement geometries of Janus droplets, which are difficult to achieve via other approaches. With this unique and well-controlled system, we were able to investigate various topological defects in both the nematic phase (*e.g.*, boojums) [1] and the smectic-A phase (*e.g.*, focal conic domains, dislocations, and smectic layer undulations) [4]. The comparative free energies of the resulting LC textures are explored. The findings suggest new routes for fabricating complex LC structures in drops.

In a second example with similar flavor, we explored shape transitions of micro-emulsion drops containing liquid crystal oligomers (short-chain LC “polymers”). These equilibrium transitions exhibited a rich set of non-spherical drop morphologies that arise from the competition between LC elasticity and interfacial tension. Specifically, upon cooling, the drops evolve reversibly from spheres to roughened spheres, flowers, and branched filaments with controllable diameter. Notably, our observations and modelling revealed that the molecular heterogeneity of the oligomer (its length polydispersity) and length-dependent spatial segregation play a crucial role in the shape transition process, which makes connections to surface patterning in biological matter. The self-assembled nematic structures were then permanently locked into place; that

is, we made liquid crystal elastomers by UV curing drops with desired morphology [3]. I will also briefly describe a few other projects using this system as a platform, which are not as yet ready for publication. This latter research includes steps towards study of nematic liquid crystal oligomer drops with chiral dopants, study of photonic properties of the nematic filamentous networks, and study of fibrous nematic LCs with nanoparticles.

In a third example, we show how two-dimensional (2D) colloidal crystal packings can form at the nematic-air interface through LC-mediated repulsion forces. We characterize these novel 2D particle crystals both structurally and dynamically. Dynamical characterization of colloidal lattices, including short-time particle diffusion and collective vibrational phonon modes, provides an novel way to probe both the phase behavior of these quasi-2D materials and the properties of the underlying LCs [2].

In addition to the work explicitly discussed in this dissertation, I have been involved in broader research efforts of the group, and as a result, I was fortunate to collaborate and contribute to other projects led by my talented colleagues. Examples of this work include LC droplet coalescence, soft-lithography techniques, synthesis of colloidal particles of diverse shapes (*e.g.*, thermo-responsive poly(N-isopropylacrylamide) (PNIPAM) microgel particles, silica rods, faceted hematite micro-cubes, and hollow silica micro-cubes), and more.

The remainder of this introductory chapter will present a brief overview of the primary topics and materials to be discussed in my thesis. The chapter concludes with an outline of the organization of this dissertation.

## 1.1 Small-molecule Thermotropic Liquid Crystals

Liquid crystals (LCs) are technologically important soft phases of matter, wherein molecules exhibit long-range orientational order and sometimes positional order. The molecules in the LC phase diffuse like molecules in normal liquids, but they maintain some degree of orientational order. This degree of internal order is affected by thermal energy and fluctuates about its “average” value, which is called the order parameter. The LC phases are generally quite different from typical crystalline solids; for example, they respond like a fluid to shear forces.

Usually, the constituent molecules of LCs are rod-like or disk-like; these molecules form particular stable liquid crystalline phases in particular temperature ranges. Generally, LCs can be made from either a pure compound or a mixture of compounds. Molecule-based (usually small-molecule-based) LC materials, whose phases change predominantly with temperature variation, are called *thermotropic liquid crystals*. By comparison, *lyotropic liquid crystals* are made by dissolving or suspending anisotropic constituents (like colloidal particles, virus particles, or macro-molecules) in a solvent (*e.g.*, water); in lyotropic LCs constituent concentration, and to a lesser extent temperature, both play roles in determining the stable liquid crystalline phases. In this thesis, I study thermotropic LCs. Nevertheless, since thermotropic LCs and lyotropic LCs share some common properties, the reported phenomena in this thesis could be applicable to lyotropic LC systems as well.

Depending on the detailed molecular ordering, there are many different phases that can be sustained by LCs. Of particular interest herein are the *nematic* and *smectic-A* phases. In the nematic phase, which is the simplest LC phase, the molecules (with anisotropic shape) maintain a preferred (oriented) direction as they diffuse through the sample (see Fig. 1b). The preferred direction is characterized by the

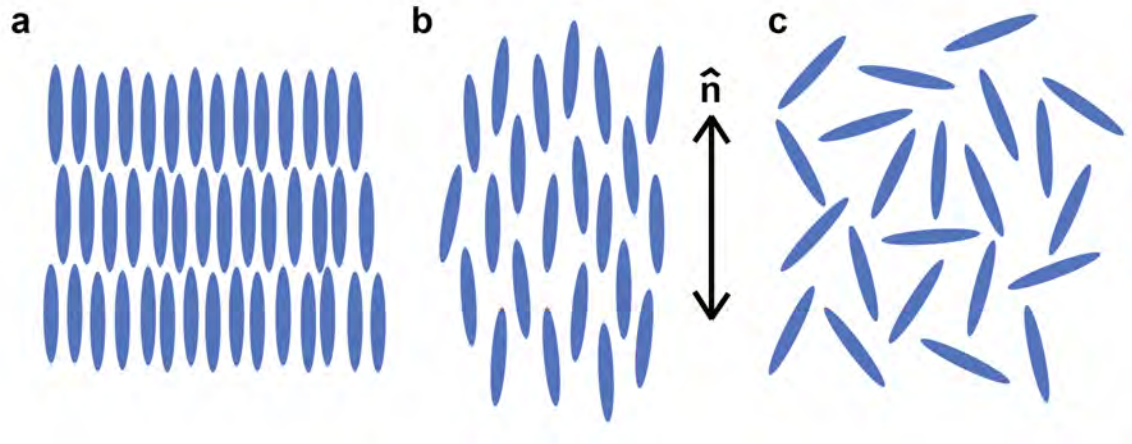


Figure 1: **Molecular arrangement in the smectic-A, nematic, and isotropic phase.** Schematics depicting **a**, smectic-A phase, **b**, nematic phase, and **c**, isotropic phase. The blue ellipses represent molecules. In **(b)**, the average director field,  $\hat{\mathbf{n}}$ , is also illustrated for the nematic.

“director  $\hat{\mathbf{n}}$ ” field (illustrated in Fig. 1b). The molecules in the nematic phase have long-range orientational order, but they are translational disordered, *i.e.*, there is no positional order in the nematic phase. The smectic-A (SmA) LC phase, on the other hand, is slightly more ordered than the nematic; it exhibits orientational and translational order. The constituent molecules of SmA LCs tend to arrange into layers with the average long molecular axis parallel to the layer normal (see Fig. 1a). Note, however, there is no positional order within individual layers; rather, translational order is associated with the stacking of layers.

In large, open, and “ideal” bulk samples, LC molecules align uniformly (on average) to minimize the system free energy. That is, the molecules in the nematic phase typically orient along a single direction (on average). Similarly, in the smectic phases, the molecules orient in one direction (on average) and assemble into sheets/layers, which typically stack in parallel planes to make a one-dimensional soft solid. In practice, a LC sample can also contain regions (defects) wherein the director is undefined.

In this case, for example, the director field can discontinuously change in passing through these singularities. These singular defects can be points, lines, or sheets.

Presently, experiments that confine LCs in containers with controllable geometry and boundary conditions are generating substantial interest. These phenomena are a major focus of this thesis. Therefore, I will briefly introduce typical LC orientation and topological defects in the simplest confinement, a spherical cavity.

If a nematic LC is confined inside a spherical container (*e.g.*, a micro-emulsion droplet) with its director perpendicular to the interface, then a radial configuration can emerge with a point defect called a radial hedgehog (of topological charge  $Q = +1$ ) at the drop center (Fig. 2a). On the other hand, if the director aligns parallel to the boundary, then the so-called bipolar configuration can arise. The bipolar configuration with two point defects at opposite points on the spherical surface are observed in this case (Fig. 2b). The surface topological defects are also known as boojums (with topological charge of  $s = +1$ ). Note,  $Q$  defines the topological charge of a point defect in 3D;  $s$  defines the topological charge of a point defect in 2D or a defect line in 3D. A charge of  $+1$  indicates that  $\hat{\mathbf{n}}$  rotates counter-clockwise by  $2\pi$  in transversing a counter-clockwise path around the defect core.

Shifting gears, SmA LCs confined in spheres with perpendicular anchoring often exhibit an onion layer texture of concentric spherical shells, again with a point defect at the drop center (Fig. 2c). The SmA LCs in planar-anchored sphere, however, can exhibit more complicated and fascinating textures, such as the focal conic domains (FCDs) (Fig. 2d; consult **Section 2.5.1** for further discussion about FCDs). Note, there are other director configurations which could be more stable than the textures shown. The equilibrium textures or configurations are determined by the total free energy of the system, which depends on bulk elastic energy, surface elastic energy, and interfacial energy.

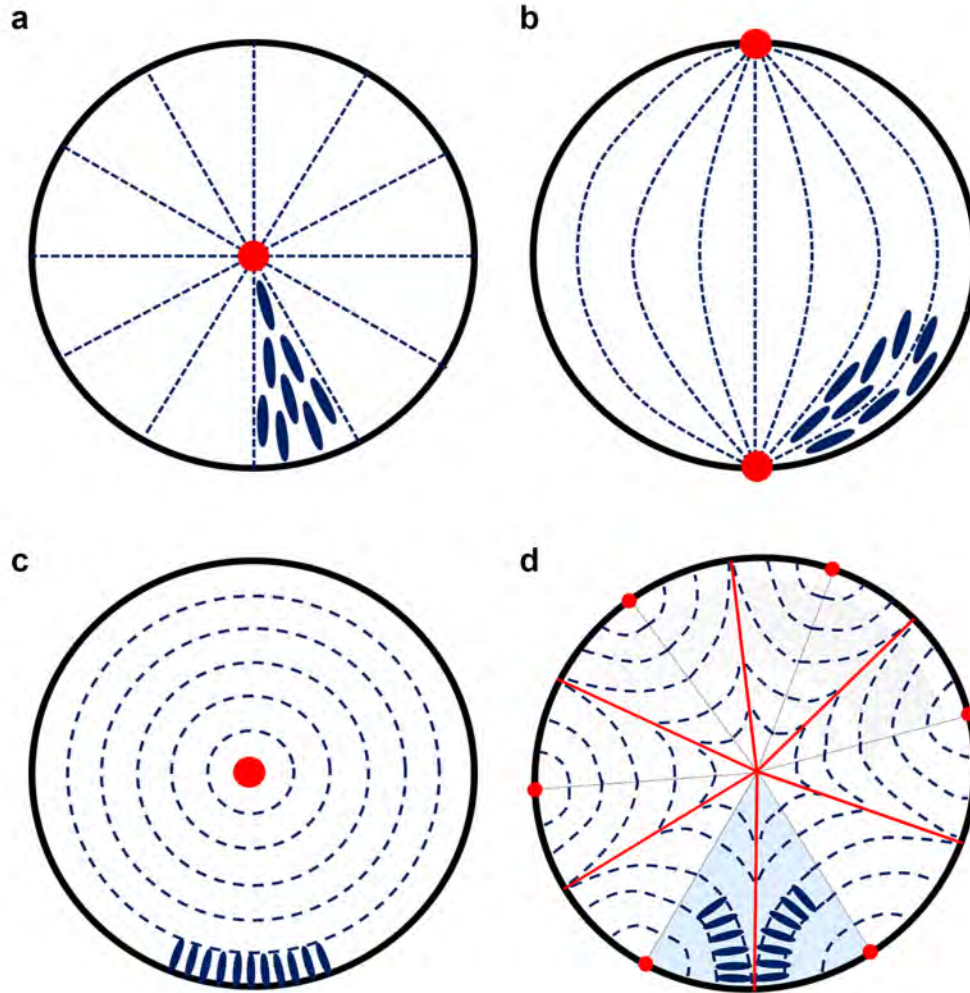


Figure 2: **Possible nematic and smectic-A configurations in spherical confinement.** Schematics of possible director orientations and associated defect textures for confined LCs. **a**, Nematic LC in perpendicular-anchored sphere gives radial configuration with a topological point defect called a radial hedgehog (red dot). **b**, Nematic LC in planar-anchored sphere gives bipolar configuration with two boojum topological defects (red dots). In **(a-b)**, blue ellipses represent LC molecules; dashed lines represent directors. **c**, SmA LC in perpendicular-anchored sphere gives onion-like texture with a point defect at center (red dot). **d**, SmA LC in planar-anchored sphere gives so-called focal conic domains (FCDs). In this case, each FCD (light blue region) contains a straight line defect in the radial direction (red line) and a circular line defect sitting on the sphere surface (represented by two small red dots). The FCDs cover the whole spherical surface to fulfill the homogeneous planar anchoring on the boundary. In **(c-d)**, the dashed lines represent SmA layers, which align perpendicular to local directors.

In **Chapter 2**, we will discuss the nematic and SmA LCs confined in spherical-cap like cavities and will characterize the associated LC configurations and textures. In **Chapter 3**, we will discuss the particle interactions mediated by nematic LC defects.

## 1.2 Liquid Crystal Oligomers and Liquid Crystal Elastomers

While small-molecule thermotropic LCs described in **Section 1.1** have played a central role in the field of LC physics, other types of molecules can form LC phases. An important example along these lines is the liquid crystal polymer (LCP). In this thesis, we work with liquid crystal polymers which have comparatively low molecular weight (*i.e.*, they only consist of a few repeating units); thus, we use the term “oligomers” instead of the word polymers to denote these materials. That is, we explore the behaviors of main-chain liquid crystal oligomers (LCOs), which are rod-like molecules separated by flexible links, as illustrated in Fig. 3. In this case, the imparted classic anisotropic properties of the soft material are due to the alignment of rod-like monomers in the oligomer chain, which in turn affect the alignment of the oligomer as a whole.

Importantly, we shall see, chain length polydispersity is a typical feature of synthetic LCO (and LCP) samples. In **Chapter 4**, we explore micro-emulsion drops containing nematic LCOs (NLCOs). We will show how the feature of molecular heterogeneity (in this case, chain-length polydispersity) offers new degrees of freedom to the system which can profoundly affect drop morphology.

Liquid crystal elastomers (LCEs) are crosslinked liquid crystal polymers (in our case, crosslinked liquid crystal oligomers) with a low overall crosslink density. The

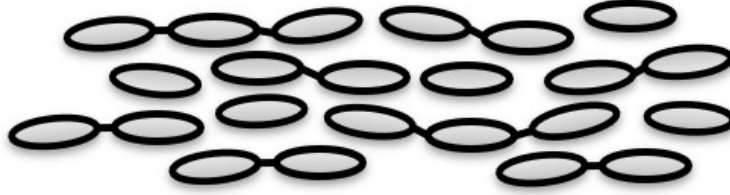


Figure 3: **Main-chain liquid crystal oligomers.** Schematic depicting main-chain liquid crystal oligomer in the nematic phase. The monomers (grey ellipses) are chained together by chain extenders. The concept of chain length polydispersity is illustrated.

weak crosslinking in a LCE, together with its inherent anisotropic mechanical properties, make possible a plethora of spontaneous actuations in response to stimuli (*e.g.*, temperature), including very special responses under stress. These features are well-suited for a wide range of functional materials design applications [5].

Using the system of NLCO drops established in Chapter 4, we will demonstrate in **Chapter 5** that the NLCO structures are readily crosslinked to lock-in nematic order and morphology, setting the stage for interesting future LCEs. Further, various dopants are added into the system as first step towards developing photonic and other functionalities based on the NLCO drops.

### 1.3 Outline of Subsequent Chapters

This thesis is organized as follows. **Chapter 2** presents experiments which explore how LCs rearrange and organize themselves in cavities while satisfying boundary conditions on the cavity surfaces. Specifically, the LC director configurations and defect textures for nematic LC (5CB) and SmA LC (8CB) confined in the spherical-cap like cavities of Janus droplets are characterized. In the 8CB experiments, I also examine the comparative free energy for observed texture patterns and identify the “equilib-

rium” state with the lowest energy. **Chapter 3** introduces another aspect of LCs, *i.e.*, their ability to drive assembly of embedded colloidal particles into microstructures. Specifically, I report on colloidal hexagonal packings at the air-nematic (5CB) interface, wherein interparticle interactions are produced by LC defects that extend from the interface into the underlying bulk LCs. I dynamically characterize the 2D colloidal lattice via video microscopy; the dynamics observed are then connected to the fundamental properties of the underlying LC material such as its viscosity and elastic constants. **Chapter 4** explores the competition between LC elasticity and interfacial tension using micro-emulsion drops containing LC oligomers. Interestingly, when the interfacial energy no longer dominates the system energy, these micro-emulsion drops exhibit shape transitions and evolve into non-trivial morphologies such as branched filamentous network, flowers, and more. The shape transitions are reversible and repeatable via temperature cycling. We discover from our analysis that molecular heterogeneity together with chain-length-dependent spatial segregation of LC oligomers play a key role in reducing interfacial tension, and thereby drive the drop shape transitions. **Chapter 5** further examines application possibilities of the self-assembled filamentous nematic networks obtained in Chapter 4. In particular, I show that the nematic structures are readily crosslinked and locked-in to become elastomers. I begin to explore potential novel functionalities of the setup by doping nematic fibers with chiral dopants, laser dyes, quantum dots, and gold nano-rods. Though unpublished, these last experiments should nucleate future work. Finally, **Chapter 6** summarizes the research presented in this dissertation and briefly elaborates on directions for future study.

# Chapter 2

## Textures in the Liquid Crystal Compartments of Janus Droplets <sup>1</sup>

### 2.1 Introduction

Liquid crystals (LCs) are technologically important soft phases of matter wherein constituent rod- or disk-like molecules retain long-range orientational order and sometimes exhibit translational order too (see details in **Section 1.1**). Much of the current interest in these questions centers on experiments that confine LCs in “containers” with controllable geometry and boundary conditions. These situations offer a novel playground to probe fundamental questions about LC assembly and response to frustration [6, 7, 8].

Both nematic and smectic LC phases are interesting to explore in this context. Recall, the nematic LC phase possesses only orientational order characterized by its director field, and the smectic LC phases form layered structures and are thus endowed with potential to exhibit translational as well as orientational order. For example, in the SmA phase, constituent molecules tend to arrange into layers with their long molecular axis parallel to the layer normal. In large and open bulk samples, these layers typically stack in parallel planes to make a one-dimensional soft solid. Another stacking configuration, found in spheres with perpendicular anchoring, is called an onion texture [9]. In still other confined geometries, with various boundary conditions, SmA LCs self-assemble into more complicated and fascinating textures. One such texture that relieves frustration in a mathematically elegant way, for example, is

---

<sup>1</sup>This chapter is based on a published paper and a manuscript in preparation for publication. In addition to this chapter, for details, interested readers might also want to consult the published paper Ref. [1].

called the focal conic domain (FCD) [10, 11, 12, 13, 14, 15, 16, 17, 18, 19, 20]. In this contribution we explore the complex textures in the nematic phase of the LC 4'-pentyl-4-biphenylcarbonitrile (5CB), and in the smectic-A (SmA) phase of the LC 4'-octyl-4-biphenylcarbonitrile (8CB), within the spherical-cap like cavities of Janus droplets containing LC and silicone oil.

In this Chapter, we first briefly report on the synthesis methods and observations associated with the nematic LC Janus droplets (of 5CB), which we reported for the first time in Ref. [1]. In the Janus droplet with homeotropic boundary conditions, a hedgehog point defect forms in the LC compartment. By contrast, with planar anchoring conditions, the nematic reconfigures and exhibits a single surface point defect called a boojum near the pole of compartment.

In the second (and main) part of this chapter, we explore SmA LC textures of 8CB in compartments of Janus droplets with homeotropic boundary conditions; these compartments hold potential to support a variety of textures [4]. Synthesis of the smectic LC Janus drops is similar to the synthesis of nematic LC Janus drops, but the resulting LC textures that form are very different from the nematic phases. Our experiments reveal formation of three classes of director/layer configurations in the LC compartment of the Janus drops. Upon formation of the initial Janus droplets, flower textures (FCDs), ring textures (dislocation rings), and textures with both undulations and dislocation rings, can all arise. Notably, the FCD packing and resulting textures have not been previously observed in emulsion droplets with homeotropic anchoring conditions. Without further disturbance, these textures are stable. However, annealing of the drops enables us to drive the system towards its lower free energy states. Our observations suggest that the lowest free energy state is a texture with dislocation rings and smectic layer undulations. The FCD and dislocation ring textures are metastable. We experimentally map out the drop conditions for which

particular textures are more (or less) likely to form, and we rationalize these findings. The study provides insight about frustration relief and suggests novel routes for guiding smectic LCs into useful forms, which could have value for functional LC materials.

## **2.2 Method and Materials**

### **2.2.1 Preparation of the Liquid Crystal Janus Droplets**

The scheme we employ to fabricate droplets with immiscible LC and non-LC compartments is described in detail in Ref. [1, 4]. Note, the syntheses of both nematic and smectic LC Janus drops are the same except for employing 5CB or 8CB as the LC ingredient. Generally, the final morphology of the drop is sensitive to several factors including compartment volume ratio, the properties of the immiscible fluids such as their interfacial tension, surfactant type, and surfactant concentration in the background aqueous phase. Here we deploy either 5CB or 8CB as the LC compartment (with its temperature-dependent phase behavior) and silicone oil (polydimethylsiloxane, PDMS) as the isotropic compartment, respectively.

The LC Janus droplets were made in three steps: (1) we first prepared (spherical) emulsion droplets containing fully miscible homogeneous mixtures of 8CB (or 5CB), PDMS, and hexane, and we suspended these precursor organic liquid drops in an aqueous solution; (2) we next made Janus droplets from the emulsion-drop precursor via solvent-induced phase separation within individual droplets; (3) we thermally annealed the samples to enable the Janus droplets to evolve to their lowest free energy state.

## Step 1

A 1:1 by weight mixture of 4'-octyl-4-biphenylcarbonitrile (8CB, Kingston Chemicals Ltd.) and polydimethylsiloxane (silicone oil PDMS, viscosity 10,000 cSt at 25 °C, Sigma-Aldrich) was dissolved in hexane (organic solvent, Fisher Scientific) to make a homogeneous organic phase mixture. Note, for the nematic Janus drops, 8CB was replaced by 4'-pentyl-4-biphenylcarbonitrile (5CB, Kingston Chemicals Ltd.), *i.e.*, in this case we dissolved a 1:1 by weight mixture of 5CB and PDMS in hexane. The total concentration of 8CB (or 5CB) and PDMS within hexane is 5% (wt/vol). Because the density of 8CB (or 5CB) and PDMS is similar, the mass ratio is well approximated as the volume ratio. Surfactants, sodium dodecyl sulfate (SDS, Sigma-Aldrich) or poly(vinyl alcohol) (PVA, Sigma-Aldrich), were dissolved in deionized water to make the background continuous aqueous phase with a surfactant concentration of 0.1% by weight (below the critical micelle concentration, CMC, for SDS). All chemicals were used as received, without further purification/modification.

The fully miscible homogeneous organic liquid mixture was then converted into a micro-emulsion droplet suspension in the background aqueous solution via two different methods. The first method entailed simply shaking the organic liquid mixture in the aqueous solution to create a polydisperse distribution of droplets. The second method used capillary microfluidics [21] to create monodisperse droplets. The volume fraction of the 8CB(5CB)/PDMS/hexane organic liquid mixture in the SDS (PVA) aqueous solution was approximately 10%. At this stage, the suspended droplets have spherical shape and contain a homogeneous miscible mixture of 8CB (5CB), PDMS, and hexane (see the left panel of Fig. 4a and Fig. 4b).

## Step 2

The 8CB(5CB)/PDMS/hexane droplets suspended in SDS (PVA) aqueous solution were collected into uncovered glass wells. The sample wells were then stored

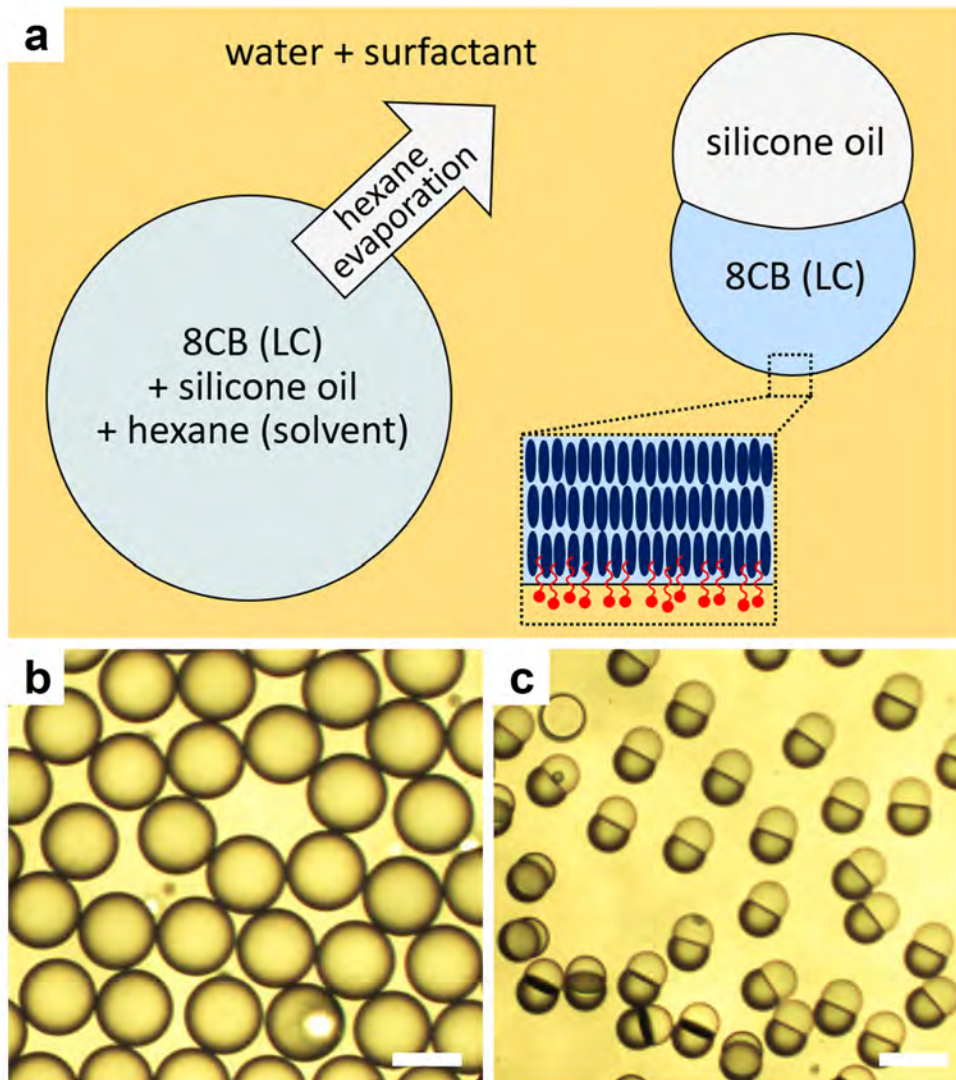


Figure 4: **Preparation of liquid crystal Janus droplets via solvent-induced phase separation.** **a**, Schematic shows how solvent-induced phase separation leads to formation of Janus droplets with two immiscible compartments: LC (8CB or 5CB) and silicone oil (PDMS). The initial droplet (left) after emulsification contains a homogeneous organic liquid mixture of LC (8CB or 5CB), silicone oil (PDMS), and hexane. The droplet is stabilized by a surfactant and suspended in the aqueous solution. Evaporation of the organic solvent, hexane, through the background phase gives the target Janus droplet (right). Inset: A closer look of the surfactant-stabilized 8CB-water interface. Dark blue ellipses represent 8CB molecules; the SmA layers are illustrated. **b-c**, Bright-field microscopy images of **(b)** the initial homogeneous droplets and **(c)** the final Janus droplets after phase separation. In **(c)**, the darker droplet compartment corresponds to 8CB. Scale bar: 50  $\mu\text{m}$ .

overnight, *i.e.*,  $\sim 12$  hours, in a custom-built chamber at 100% relative humidity. This setup expedites evaporation of hexane from the droplets and minimizes evaporation of water from the surfactant solution. Throughout the process of hexane evaporation, we believe that the evaporation of water from the solutions containing SDS or PVA surfactant was negligible.

The complete evaporation of hexane causes separation of the immiscible 8CB (5CB) LC and PDMS within the drops. Then formation of the Janus droplets readily occurs (see the right panel of Fig. 4a and Fig. 4c). The Janus droplets made by shaking had diameters ranging from 10 to 70  $\mu\text{m}$ ; the monodisperse droplets made via capillary microfluidics typically had a radius of 15.4  $\mu\text{m}$  that depended on dimensions of the microfluidics set-up and the fluid flow rates. We transferred the Janus droplet suspensions to rectangular capillaries (0.4 mm height and 4 mm width, VitroCom), sealed them with glue, and stored them at room temperature for 24 hours before observation.

Note, at this stage, we have generated the “quenched” Janus droplets with smectic 8CB (or nematic 5CB) confined in the spherical-caps. (A further discussion about the meaning of quench is given in **Section 2.5**.) Analysis of the resultant LC configurations/textures and droplet morphologies were then carried out.

### Step 3

The samples obtained in **Step 2** were first studied optically. Subsequently, they were annealed (quickly heated to 45  $^{\circ}\text{C}$  and then slowly cooled to room temperature). This annealing procedure enhances the probability of generating equilibrium LC textures. We define these latter stage drops as “annealed” Janus droplets. The resultant annealed LC textures and droplet morphologies were again studied and analyzed using optical microscopy.

Lastly, some of the annealed Janus droplets were stored and allowed to relax at

room temperature for another few days, and then they were optically checked again.

### **2.2.2 Analysis of Liquid Crystal Configurations and Textures**

Sample cells containing SmA LC Janus droplets (or nematic LC Janus droplets) were observed with a Leica DMIR13 inverted optical microscope in bright-field and polarization optical microscopy (POM) modes. Leica N Plan 10 $\times$ , Leica PL Fluotar L 63 $\times$ , and Leica PL APO 100 $\times$  objectives were used. Crossed-polarizers and full-wave retardation plates were deployed in the microscope to characterize LC director configurations within the droplets (Fig. 5a).

Note, because of the slight density difference between the two compartments, Janus droplets rotate and align with the denser material (8CB or 5CB) closer to the surface of the earth. Thus, optical images taken by the inverted optical microscope are mostly bottom-view images of droplets, wherein the LC filled spherical-cap cavity resides symmetrically in the part of the drop closest to the earth surface. Note, LC birefringence and the curved interfaces of the droplet typically cause some image distortion.

### **2.2.3 Analysis of Janus Droplet Morphologies**

Side-view images of SmA LC Janus droplets, aligned by gravity, were also recorded using a small and portable Bausch and Lomb monocular microscope operating in bright-field mode; this microscope was equipped with a 43 $\times$  air objective. We obtained these measurements by turning the monocular microscope (together with the mounted sample cell) on its side and then taking side-view images of the Janus

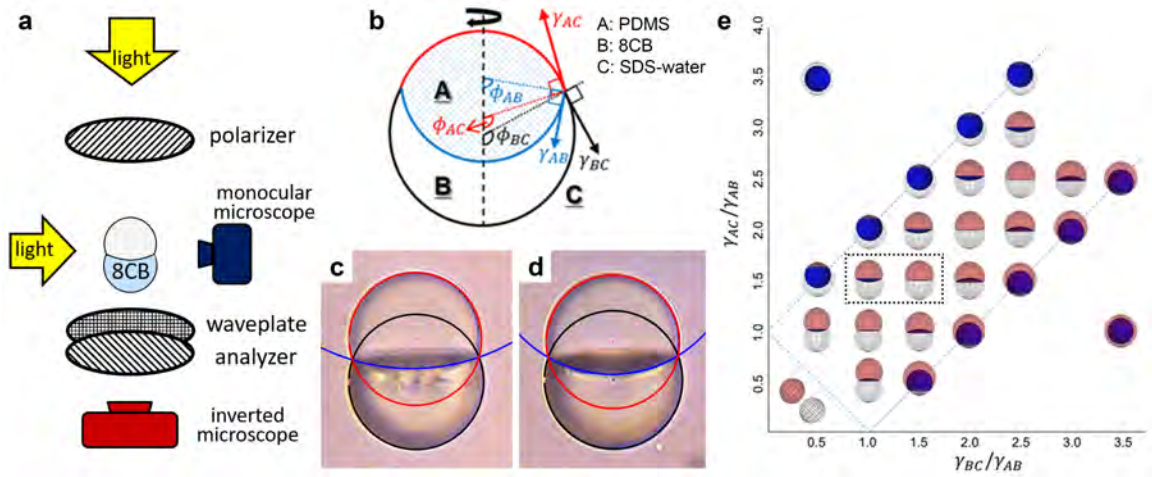


Figure 5: **Morphology profiles of the liquid crystal Janus droplets.** **a**, Schematic of the experimental setup. Bottom-view and side-view images of individual Janus droplet were taken by an inverted optical microscope (dark red, with crossed polarizers and full-wave retardation plate) and a turned monocular microscope (dark blue), respectively. **b**, Schematic of a side-viewed Janus droplet (A: PDMS, B: 8CB, C: SDS aqueous solution). At the three-phase boundary,  $\gamma_{AB}$ ,  $\gamma_{BC}$ , and  $\gamma_{AC}$  denotes interfacial tension for the 8CB-PDMS, 8CB-water, and PDMS-water interfaces, respectively. **c-d**, Exemplary side-view images of SmA Janus droplets containing **(c)** FCD flower textures and **(d)** dislocation ring textures. Representative circle fits used to extract the interfacial tension ratios are also illustrated. Drop radius:  $15.4 \mu\text{m}$ . **e**, The droplet morphology state diagram with respect to interfacial tension ratios. The volume ratio between LC and PDMS is fixed to be unity. Blue dashed lines represent the boundaries in a Janus droplet, in a core-shell (top left and bottom right) droplet, and in two detached droplets (bottom left). Black dashed square roughly denotes our experimental regime. In **(b-e)**, black, red, and blue interfaces correspond to 8CB-water, PDMS-water, and 8CB-PDMS interface, respectively. Note, schematics **(b)** & **(e)** were initially generated by Joonwoo Jeong and are adapted from Ref. [1].

droplets (Fig. 5a). We determined and analyzed the droplet morphologies by fitting the drop profiles as detailed below.

Morphologies of the compartments within Janus droplets are determined by the relative values of the interfacial tension between the two immiscible compartment liquids (*i.e.*, 8CB/5CB and PDMS) and the third immiscible background liquid (*i.e.*, the SDS-water solution). In equilibrium, the three-phase boundary adopts a unique configuration, requiring a vector sum of zero for the three interfacial tensions (known as Neumann’s triangle; see Fig. 5b). Experimentally, the three interfacial tensions  $\gamma_{8CB-PDMS}$ ,  $\gamma_{8CB-water}$ , and  $\gamma_{PDMS-water}$  are characterized by the contact angles at the junction point. We determined the contact angles by fitting each phase boundary to an arc [22] (see examples in Fig. 5c and Fig. 5d). Specifically, the arc is the best fit for a set of three points on each interface, including the two intersection points on the three-phase boundary. We excluded data when the two intersection points are not readily apparent, when there is recognizable disagreement between the best fit and corresponding interface, or when the calculated volume ratio between compartments substantially disagrees with experimental parameters. Note, the latter two situations could arise from Janus droplets whose symmetry axes are not fully aligned with gravity, or from image distortions arising near the 8CB-PDMS boundary (*e.g.*, due to LC birefringence).

## 2.3 Properties of the Liquid Crystal Janus Droplets

The resultant LC Janus droplets, which are tens of microns in diameter and dispersed in water containing SDS or PVA surfactant, were analyzed primarily by

optical microscopy. As detailed in **Section 2.2.1**, the Janus droplets were made via a phase separation scheme (Fig. 4a). The SDS molecules absorbed at the 8CB-water (or 5CB-water) interface create a strong preference for homeotropic anchoring, wherein the local LC director is perpendicular to the surface. Thus, for the smectic LC (8CB), the local SmA layers prefer to align parallel to surfaces (Fig. 4a inset). For the sample with PVA surfactant, planar anchoring is preferred at the interface, wherein local director is parallel to the surface.

Recall, initially, each surfactant-stabilized emulsion droplet (left panel of Fig. 4a and Fig. 4b) has spherical shape and contains LC, PDMS, and hexane. Importantly, both LC and PDMS are well dissolved in hexane at this stage. The organic solvent then evaporates from the individual droplets. After complete evaporation of hexane, the immiscible 8CB (or 5CB) and PDMS phases separate, forming Janus droplets with two compartments (right panel of Fig. 4a and Fig. 4c).

As discussed in **Section 2.2.3**, the morphologies of Janus droplets are determined by the relative interfacial tension between  $\gamma_{8CB-PDMS}$ ,  $\gamma_{8CB-water}$ , and  $\gamma_{PDMS-water}$ . The three interfacial tensions are characterized by the contact angles at the junction point (see Fig. 5b), and we determine the contact angles by fitting each boundary separating the two phases to an arc [22] (Fig. 5c and Fig. 5d). Note, in this analysis, we are assuming that the orientational order and elasticity of the LCs do not substantially affect the three-phase boundary, *i.e.*, the interfacial energy is assumed to determine the cavity geometry.

By choosing the interfacial tension ratios carefully, three possible droplet morphologies can be achieved: complete engulfing (the core-shell droplet), partial engulfing (the Janus droplet), and non-engulfing (two detached droplets) [1, 23]. The theoretical droplet morphology state diagram is illustrated in Fig. 5e; it presents these possibilities with respect to interfacial tension ratios, while the volume ratio between

two compartment phases is fixed to be unity. Among the controllable parameters, the ratio between interfacial tensions can be tuned by employing different compartment ingredients, or by employing a different type and amount of surfactant molecules adsorbed at the interface. Here, we focus on the rich set of LC configurations that a *single* droplet morphology supports. Specifically, in **Section 2.4**, we are going to discuss the case of 5CB-PDMS with a 1:1 volume ratio and in a 0.1 wt% PVA and SDS aqueous solution. In **Section 2.5 - Section 2.7**, we will discuss the combination of 8CB-PDMS with a 1:1 volume ratio and in a 0.1 wt% SDS aqueous solution.

## 2.4 Nematic Liquid Crystal Textures within Janus Droplets

In the absence of external fields, it is well known that the director configurations of LCs in confinement are determined by the balance of the bulk LC elasticity and surface anchoring on the cavity boundaries [24, 25]. In this section, we briefly report on the Janus drops with nematic compartments, the simplest LC phase. This will serve as a model system for easier understanding of our later discussions.

As exhibited in Fig. 6, the perpendicular anchoring at the 5CB-PDMS interface and tangential anchoring at the 5CB-PVA water solution interface cause the nematic LCs to reconfigure, giving rise to a single surface point defect, boojum, near the (south) pole of the LC compartment. The nematic Janus droplet in a SDS aqueous solution, by contrast, sustains a hedgehog point defect in the LC compartment because the 5CB-SDS water solution interface and the 5CB-PDMS interface both have homeotropic anchoring.

The observed surface boojum and bulk hedgehog point defect are both well

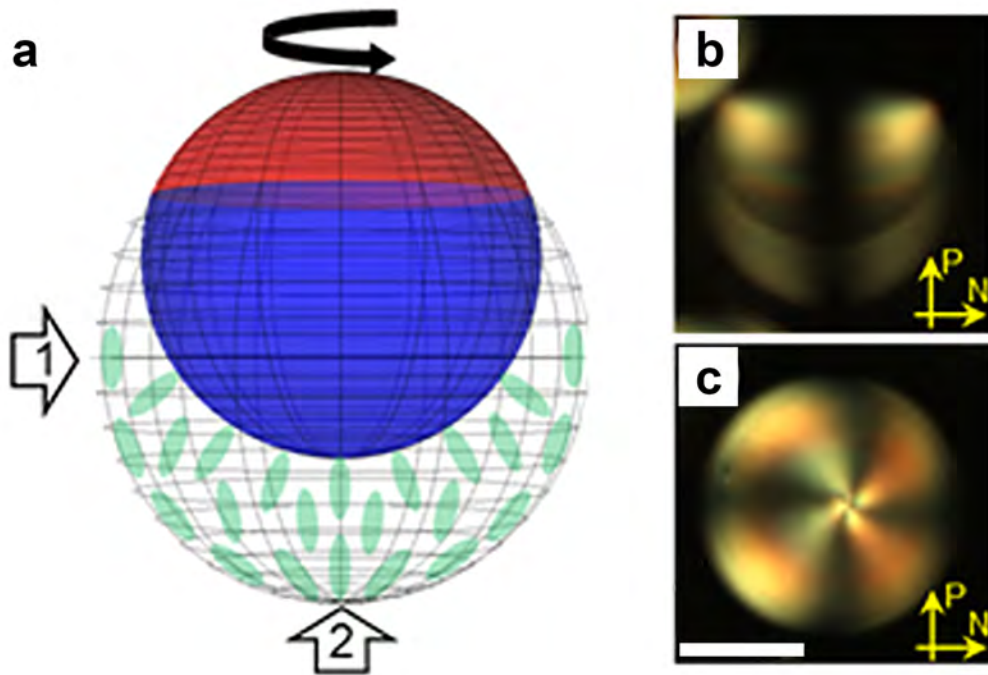


Figure 6: **Nematic textures within Janus droplets.** **a**, Schematic of a 5CB-PDMS Janus droplet in a 0.1 wt% PVA water solution. The green rods represent LC mesogens with directors parallel to the 5CB-water interface but perpendicular to the 5CB-PDMS interface. **b**, Side-view (direction 1) polarization optical microscopy (POM) image of the Janus drop. **c**, Bottom-view (direction 2) POM image of the Janus drop. Scale bar:  $20 \mu\text{m}$ . Note, these figures were initially created by Joonwoo Jeong and are adapted from Ref. [1].

studied and typically observed in spherical LC droplets with uniform planar and homeotropic anchoring, respectively. Thus the unique spherical-cap geometry, generated in the Janus drop and employed here, does not play an important role in creating new LC textures. Thus, for the rest of this chapter, we will mainly focus on the Janus droplets with smectic LC compartments, which are much more interesting.

However, after discussion of the smectic systems, we will briefly summarize additional findings about the nematic LC Janus drops that were reported in Ref. [1]. This discussion is in **Section 2.8** and **Section 2.9**. Note, this phenomenology observed in the nematics could be applied to the smectic systems too, which could lead to interesting future work.

## 2.5 Smectic Liquid Crystal Textures within Janus Droplets after Initial Quench

Our platform for fabricating the Janus LC droplets permitted the control of compartment morphology and boundary conditions needed to manipulate smectic LC textures. For these drops, when the hexane evaporates during first formation of the Janus drops, a turbulent-like/vigorous mixing was observed in the droplet as it transformed from a homogeneous mixture to the targeted phase-separated stage. Here we adopt the term, “quench”, to denote this whole initial process. Note, the quench includes a rapid transformation from a disordered state (*i.e.*, no LC ordering) to an ordered LC state in the final compartment configuration. Note also, this quench is not thermal (temperature is not changed), but it has an effect that is similar to a temperature quench. When the LC is dissolved in the hexane (together with PDMS) the system is isotropic, but when the solvent (hexane) is completely removed, then

the LC exists in the SmA phase.

We analyzed the SmA LC textures using bright-field optical microscopy and polarization optical microscopy (POM) (see Fig. 5a), and we found them to be of three types after the quench. The LC configurations were either flower-like FCD textures (Fig. 7a; **Section 2.5.1**), dislocation ring textures (Fig. 7b; **Section 2.5.2**), or the combination of undulation and dislocation ring textures (Fig. 7c; **Section 2.5.3**). Note, the images shown in the figure are bottom-views of the droplets. In the following subsections, we describe and characterize these texture patterns.

### 2.5.1 Focal Conic Domain Flower-like Textures

Amongst all SmA configurations, the FCD flower-like texture is perhaps the most visually striking (Fig. 7a). Previously, FCDs have been observed within planar-anchored substrates [10, 11], free-standing droplets on surfaces [12], pinned liquid menisci [13, 14, 15, 16], planar anchored spherical micro-emulsion drops [17, 18, 19] and planar anchored Janus droplets [20]. In some of these situations, FCDs hold potential for application [14, 26, 27, 28, 29]. In our Janus drop compartments, which have *homeotropic* anchoring, the packing that generates the texture is comprised of adjacent FCD “petals” arranged symmetrically around the central axis of the droplet. Within each individual FCD, SmA layers wrap around a pair of disclination (defect) curves which are conjugate conic sections: an ellipse, characterized by its eccentricity, and a hyperbola branch that passes through one focus of the ellipse. These two (3D-spanning) disclinations then project onto the focal plane, giving the texture its iconic dot-within-ellipse pattern which we observe in the bottom-view image.

Previously, contiguous FCD textures have only been observed in spherical and Janus emulsion droplets with parallel anchoring conditions [17, 18, 19, 20]. In fact,

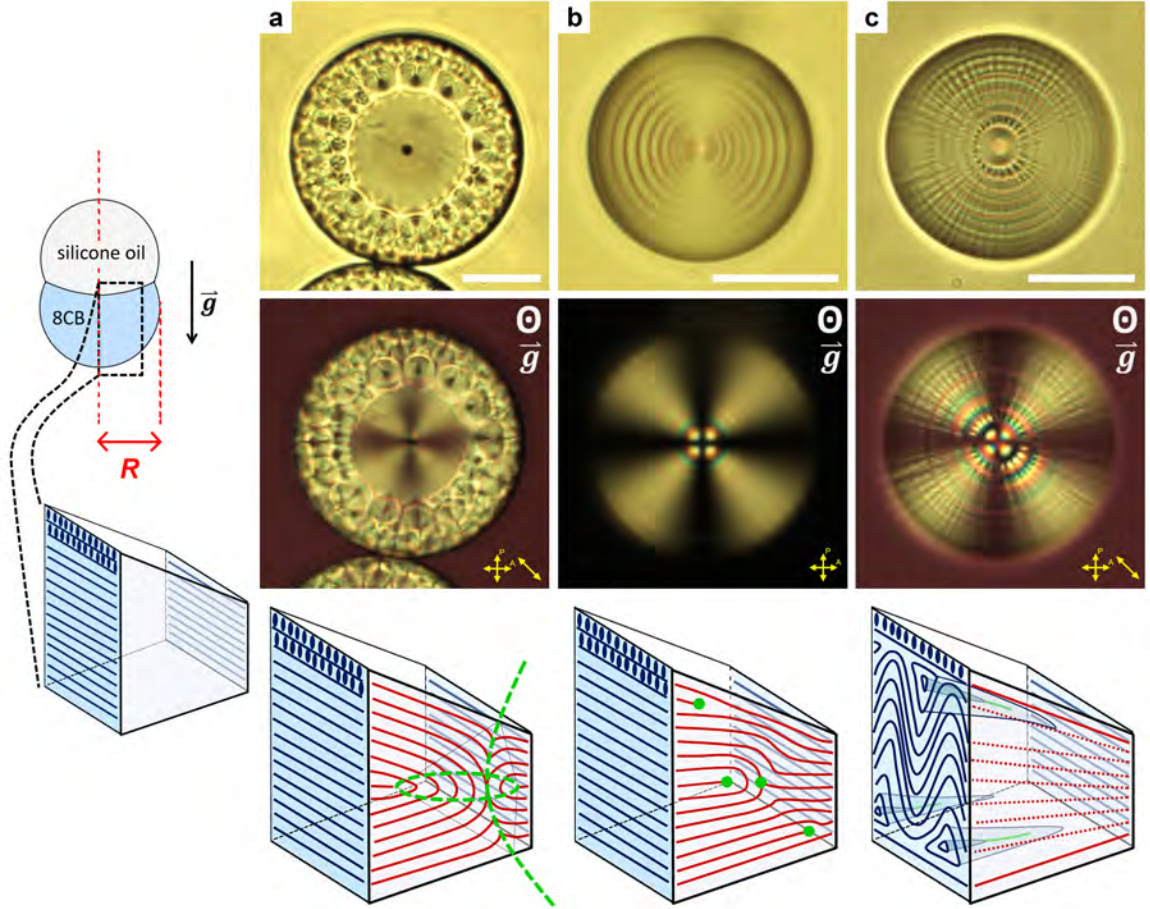


Figure 7: **Smectic-A textures within Janus droplets: focal conic, dislocation ring, and undulation textures.** The bottom-view bright-field (first row) and POM (second row) images of common textures for SmA LC confined in the spherical-caps of Janus droplets, after the initial quench (phase separation). The observed textures include **a**, FCD flower-like textures, **b** dislocation ring textures, and **c**, textures with both undulations and dislocation rings. Scale bar:  $20 \mu\text{m}$ . The vector  $\vec{g}$  in the figures denotes the direction of the gravitational acceleration. Note, the drop size is defined by the radius,  $R$ , of the LC compartment as illustrated in the left panel sketch. Inset schematics (side-view, illustrated in left panel sketch) show how SmA layers arrange themselves in order to accommodate the mismatch of smectic layer numbers between drop center and edge. In **(a)**, the ellipse and hyperbola disclinations (green dashed curves) of the FCD are illustrated. In **(b)**, the core region of the edge dislocation could correspond to the end of a broken layer (green dots at top and bottom), or to where the defect core splits into two disclinations of opposite signs (pair of green dots at center). In **(c)**, only layer undulations are illustrated for simplicity (*i.e.*, coexisting dislocation rings are not included in the schematic). The suggested segments of disclinations extending along the drop radius are also illustrated (green segments).

it is somewhat unexpected to find FCDs in homeotropic-anchored Janus droplets at all. In our system, homeotropic anchoring arises at both 8CB-water and 8CB-PDMS interfaces and causes the SmA layers to reconfigure parallel to the local surface curvature. Since the layer thickness is fixed, in the spherical-cap like geometries, more layers are required near the drop center compared to the drop edge. A spatial mismatch of layer number thus arises at various positions within the drop. The energy cost of changing the SmA layer thickness is typically considerably greater than that of layer bending [17]. Thus, one way for the SmA layers to ameliorate layer number mismatch frustration is to generate FCDs between cavity center and edge. A schematic of this texture is shown in the inset of Fig. 7a. Notably, these FCDs, that appear in our SmA LC Janus droplets, are “geometry-driven” rather than “anchoring-driven” as in prior micro-emulsion work [17, 18, 19, 20].

Within this cavity, we find that FCDs pack in an interesting and uncommon manner, *i.e.*, their ellipse disclination long-axes orient radially from a common point on the symmetry axis of droplet, by forming rings of FCDs. As suggested by Meyer *et al.* [12] and Beller *et al.* [15], such FCD flower textures (packing with non-zero eccentricity) have hyperbolae that diverge away from the structural center with no obvious intersection. Meantime, the virtual branches of the hyperbolae intersect at a common apex located on the structural symmetry axis. This observation is in contrast to the case wherein FCDs spontaneously assemble and tile space following the law of corresponding cones (LCC) [17, 30, 31, 32, 33]; additionally, our observed textures cannot be explained by the traditional tilt grain boundary model [33] due to the deformed interface. In light of these factors, our observations are best explained as a construction of alternating belts of FCDs, joined smoothly onto a family of concentric spheres which share either common base or apex [15].

Finally, for completeness we studied Janus droplets suspended in water at high

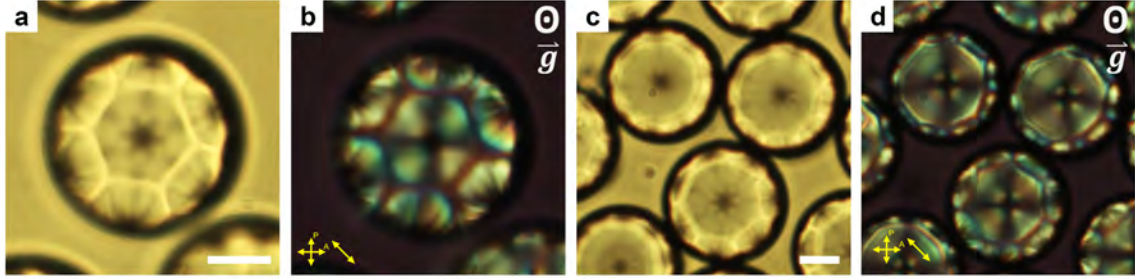


Figure 8: **Focal conic textures within Janus droplets at high SDS concentration.** **a-b**, The bottom-view bright-field and POM images of SmA Janus droplets in 0.5 wt% SDS water solution (above CMC). Notice that the FCDs within each droplet extend to the drop surface, showing configurations different from the low SDS concentration (Fig. 7a). **c-d**, Under the same conditions, another sample of Janus droplets exhibited similar FCD textures. Scale bar: 10  $\mu\text{m}$ .

SDS concentration (above CMC). In this case, the FCDs extend to the surface and exhibit bud-like internal textures (see Fig. 8). Further characterization is necessary to identify the director configurations and is a subject of future work.

### 2.5.2 Dislocation Ring Textures

The mismatch of SmA layer numbers between Janus drop cavity center and edge can accommodate textures that are simpler than the FCDs. For example, the frustration due to layer mismatch can also be relieved by introduction of edge dislocation defects (Fig. 7b). In smectics, the core region of the edge dislocation could correspond to the end of a broken layer, or to where the defect core splits into two disclinations of opposite signs [34, 35].

Within the spherical-cap cavity of our Janus droplets, the smectic layer number difference is readily accommodated by a series of dislocations; these dislocations extend in circular contours along the direction perpendicular to the drop radial vectors. Exemplary SmA layer configurations showing these dislocations are depicted in inset

of Fig. 7b. As long as the LC compartment/cavity retains symmetry with respect to the central drop axis, each individual dislocation will form a closed-loop centered on the central symmetry axis. This property gives rise to the ring textures observed in the droplet bottom-view (see Fig. 7b).

### 2.5.3 Smectic Layer Undulation Textures

Both the FCD flower and dislocation ring textures require energetically costly disclinations. The strain and elastic energy density grow large as one approaches the singular defect cores. It is thus important to consider whether/how this elastic distortion energy could be decreased. Would it be possible, for example, for “defect-free” LC textures to span all or parts of the compartment cavity while still satisfying cavity geometrical and topological constraints? The answer is yes. One possible energetically cheaper solution, which appears to arise experimentally, is a third type of texture with radial undulations of the smectic layers.

Such undulating textures exhibit periodic radial striped patterns in the transmission image as observed from the droplet bottom-view (see Fig. 7c). The bright-dark alternation between stripes suggests that the local optical axis is rotated from its original uniform orientation (associated with the dislocation rings), *i.e.*, the axis points in different directions in adjacent stripes. This characteristic appearance of the radial wrinkles is likely due to the SmA layer undulation (a buckling instability); layer undulation is a common occurrence when layers with a preferred uniform spacing are subject to dilative stress above a certain threshold [36, 37]. In such cases, the free energy of the smectic LC is minimized by generation of undulating layers. In the present case, this stress arises from the spherical-cap geometry, a scenario similar to that previously proposed for systems with various shapes [38, 39, 40, 41].

By contrast to the FCD textures and dislocation ring textures, which are accommodated by topological defects, here if the layer number in a given slice (cross-section) of the spherical-cap is constant, then the geometrical constraint is equivalent to a dilation; dilation can cause the LC director to bend. This dilative stress will be more severe closer to the drop center. Since director bending is prohibited in the SmA phase, once above a critical stress, the SmA layers will undulate to fill space and relax stress. As schematically indicated in inset of Fig. 7c, the smectic layers buckle progressively and increasingly along radial direction toward droplet center (*i.e.*, along the direction of maximum cavity thickness change). Our measurements also suggest that segments of disclinations extending along droplet radius could potentially arise to fill the troughs between adjacent buckles. As a result, the corresponding “effective” thickness at drop center could be greater than simply the sum of individual smectic layers to best accommodate the spherical-cap geometry.

Note, the pure undulation scenario described above is best suited to cavities with small thickness gradients. In practice, the SmA layer undulation texture can combine with dislocation ring texture to fulfill the geometrical requirements of our Janus droplets. Our observations suggest that this type of combination texture does indeed arise in practice and is actually the lowest free energy texture for our system (see **Section 2.6** and **Section 2.7**).

## 2.6 Metastable Smectic-A Textures

In **Section 2.5**, we described, classified, and explained three types of SmA LC textures that typically form after the first quench to create the Janus LC drops. Here we report on measurements of the occurrence and character of the SmA textures as a function of droplet size, defined by the radius,  $R$ , of the 8CB compartment (illustrated

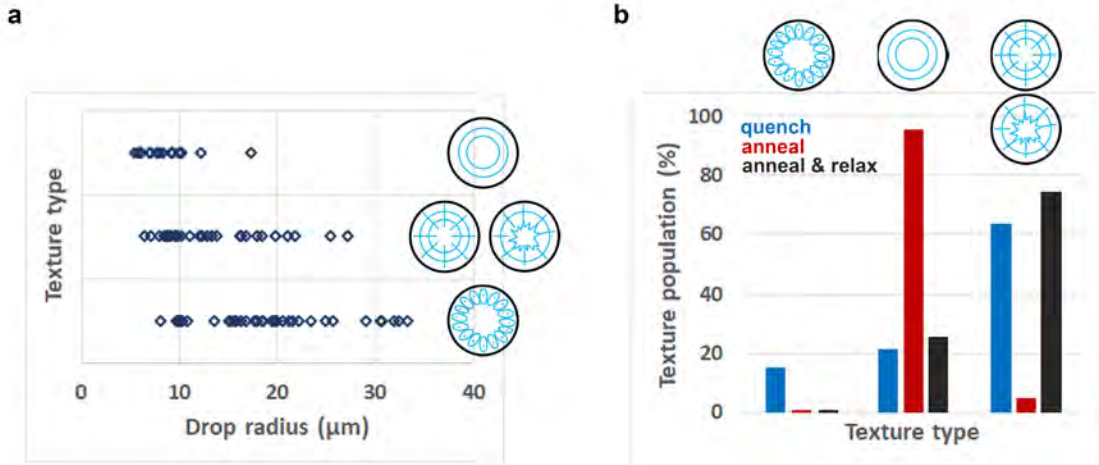


Figure 9: **Occurrence of different SmA textures with respect to drop size & their evolution after the quench, after annealing, and after annealing/relaxation.** **a**, Occurrence of FCD flower textures (bottom row), textures of undulations and dislocation rings (middle row), and dislocation ring textures (top row) as a function of Janus droplet size. These samples were made by the simple shaking method, and the observations were made after the first quench. **b**, The population (percent occurrence) of each texture type measured after the first quench (blue bar), after annealing (red bar), and after annealing and further relaxation (black bar). Left, middle, and right columns represent FCD flower textures, dislocation ring textures, and textures of undulations and dislocation rings, respectively. These data were gathered from a pool of  $> 1,000$  droplets with monodisperse radius  $R = 15.4 \mu\text{m}$ , fabricated by microfluidics.

in the left panel sketch of Fig. 7). As indicated in Fig. 9a, the very largest drops only sustain FCD textures; similarly, the very smallest drops only sustain dislocation ring textures. For an intermediate range of drop sizes ( $R \approx 10 \sim 20 \mu\text{m}$ ), all three textures are found.

The occurrence frequency behavior of the different textures raises questions about SmA texture stability and free energy. Here we are most interested in ranking the free energy of these different textures. To elucidate this issue, we employed a microfluidics setup to fabricate Janus droplets with monodisperse size  $R = 15.4 \mu\text{m}$ , thereby enabling systematic analysis of the population of each texture type. The blue bars of

the bar chart in Fig. 9b exhibit the percentage of occurrence of FCD flower textures, dislocation ring textures, and undulation textures (which typically coexist with dislocation ring textures) from a pool of  $> 1,000$  droplets. The observations show that after quenching, for the intermediate-size drops, more than 50% have a radial undulation texture; among the rest, the dislocation ring texture is a little more likely than the FCD texture. Moreover, all configurations are stable over time in the absence of perturbations. These clues suggest that several *metastable* SmA textures can form, and that those with undulations have the lowest free energy.

We also explored the possibility that different cavity geometries could be associated with particular metastable textures. Specifically, we fit the phase boundaries of Janus droplet cavities (see details in **Section 2.2.3**), and from these fits we calculated interfacial tension ratios. These studies suggest that somewhat different cavity morphologies arise for droplets that contain different textures (Fig. 10a). Distinguishing between droplets that contain dislocation rings or undulations plus dislocation rings is difficult, but droplets with FCDs were relatively easy to distinguish from the other two cases.

The plot of  $\gamma_{8CB-PDMS} - \gamma_{8CB-water}$  (Fig. 10a) suggests that the occurrence of FCD textures is accompanied by larger interface tension on both 8CB-water and 8CB-PDMS boundaries, but especially at the 8CB-water interface. This larger interfacial tension effect could be caused by the FCD textures, or it could arise during drop formation (the quench and rapid mixing process) and thereby create a cavity geometry that slightly favors formation of FCD textures. An increase in interfacial tension could be caused, for example, by deviation of LC directors near the surface from preferred homeotropic anchoring, which in turn would diminish the occurrence of well-aligned interfacial molecular packings [42, 138, 139, 143, 144]. The FCDs could induce more serious interfacial distortions than either dislocations or layer undula-

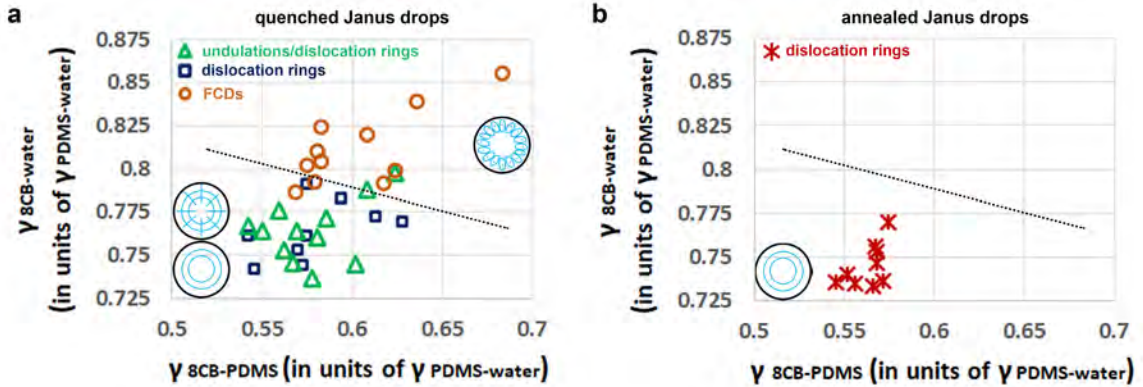


Figure 10: Cavity morphologies and interfacial tensions for Janus drops containing different SmA textures after the first quench and after annealing. The experimentally determined ratios between interfacial tensions are connected to the Janus drop cavity morphologies. **a**, Plot of  $\gamma_{8CB-PDMS} - \gamma_{8CB-water}$  for the Janus drops after the quench (and concurrent phase separation). The green triangles, blue squares, and orange circles indicate drops containing textures of undulations plus dislocation rings, dislocation ring textures, and FCD flower textures, respectively. The black dotted line roughly separates regimes of FCD drops and dislocation/undulation drops and is drawn to guide the eye. **b**, Plot of  $\gamma_{8CB-PDMS} - \gamma_{8CB-water}$  for Janus drops after annealing. For this case, only drops containing dislocation ring textures were observed (represented by red stars). The same black dotted line as shown in (a) is given for comparison. Note, both  $\gamma_{8CB-PDMS}$  and  $\gamma_{8CB-water}$  are represented in units of  $\gamma_{PDMS-water}$ , which is fixed.

tions; the greater distortion is associated with less ordered interfaces, which leads to larger interfacial tensions.

## 2.7 Metastable Smectic-A Textures Evolve after Annealing and Relaxation

As noted in **Section 2.6**, the three observed SmA textures after the first quench appear to suggest the existence several metastable textures. To address the question of metastability, we employed a thermal annealing process. In essence, the thermal

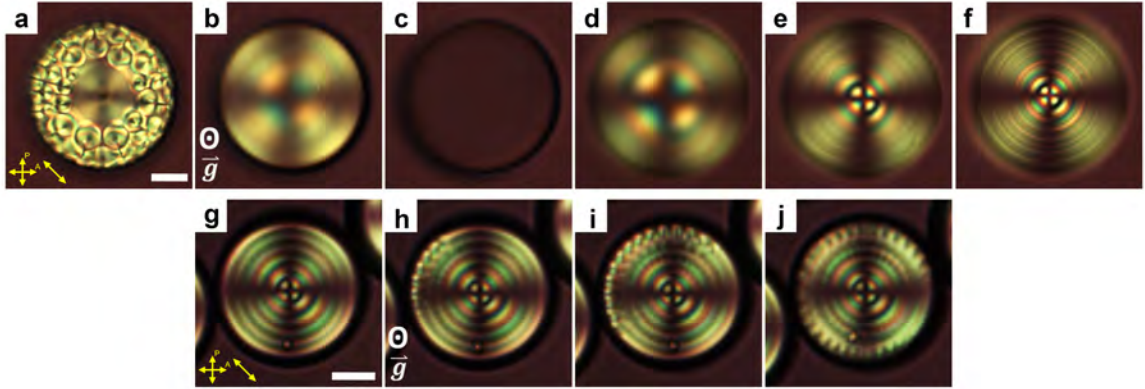


Figure 11: **SmA texture evolution/transition during thermal annealing and relaxation.** FCD flower textures (achieved after the initial quench) melt as the system temperature is increased so that the 8CB undergoes a phase transition from **a-c**, SmA phase through nematic phase to the isotropic phase. **d**, The temperature is then decreased slowly again, so that the LCs “pre-align” with a radial configuration in the nematic phase. **e-f**, Further cooling then leads to formation of dislocation ring textures in the SmA phase. Note, the FCD textures do not reoccur after annealing. **g-j**, Occasionally, smectic undulations could be observed to appear on top of the existing dislocation rings and further “relax” the SmA droplets into their final equilibrium states. Note, the image snapshots in (**a-f**) and (**g-j**) were taken from different droplets. Also, the focal plane varies slightly between images, which leads to an apparent slightly different drop size. Scale bar: 10  $\mu\text{m}$ .

annealing process heated 8CB into its isotropic phase and then cooled slowly so that 8CB condensed sequentially into its nematic phase and finally its SmA phase. Such heating-cooling schemes provide an opportunity for the LC molecules to rearrange and achieve their lowest free energy configuration in the cavity.

Interestingly, by far the most common texture of the annealed drops had the dislocation ring texture (see red bars in Fig. 9b). FCD textures were never observed after annealing. We thus conclude that the FCD textures are metastable and are the most energetically costly texture of the three. An exemplary droplet displaying the texture transition from FCD flower textures (forming upon quench) to dislocation

rings (after annealing) is shown in Fig. 11a-f.

Although the data are not fully unambiguous, we propose that formation of metastable FCDs upon quench is due to rapid-turbulent-like/vigorous mixing within the droplet that occurs during phase separation (as discussed at the very beginning of **Section 2.5**). Vigorous hydrodynamic flows randomize the system transiently during the quench, and the (relatively) short time interval for formation of ordered states likely prevents the SmA LC from reaching its equilibrium configuration. In addition, once formed, the high viscosity of 8CB makes texture reformation kinetics extremely slow. The annealing procedure, by contrast, melts the LC compartment into disordered isotropic phase and then cools slowly enough to permit the system to remain close to equilibrium. Importantly, the “pre-alignment” of LC directors in the nematic phase, *i.e.*, at early stage of the cooling process, helps lock the LC molecules into their final alignment in the bulk. Note, in the nematic phase, the LCs exhibit a radial configuration with a point defect at drop cavity center. As the temperature decreases further, the SmA layers then rearrange based on an already partially ordered structure. We confirmed the more consistent and narrowly distributed morphology of these annealed Janus droplets by fitting their phase boundaries, which agree well with the quenched droplets containing dislocation rings (red stars in Fig. 10b).

Finally, when these annealed Janus droplets which mostly contain dislocation rings are further “relaxed” at room temperature for another few days (without interruption), we found that a large portion of the droplets undergo another texture transformation into the combination state of dislocation rings with undulations (see black bars in Fig. 9b). Evidently, the transition arises because the existing SmA structures and dislocation disclinations cannot fully satisfy the geometric and anchoring boundary conditions. As a result, further modulation in the smectic phase is desirable to lower free energy. Since extra smectic layers or disclinations cost energy,

and because layer undulation is a fast relaxation in the presence of stress [24, 41, 43], the texture layer undulations gradually increase from droplet edge toward center, corresponding to the radial striped patterns as characterized in **Section 2.5.3**, until the boundary conditions are completely fulfilled (see Fig. 11g-j).

## 2.8 More and Different Liquid Crystal Confinement Geometries: Variable Spherical-cap Morphologies and Patchy Droplets

The primary experiments in this thesis focused on the LC configurations, common to both nematic and smectic phases, that our Janus drops could support. As a result, we have emphasized a *single* “snowman-like” drop morphology with a 1:1 compartment volume ratio in **Section 2.4** through **Section 2.7**. However, our procedure for fabricating LC Janus droplets permits fine-tuning of compartment morphology and boundary conditions. In this section, we summarize these possibilities and describe some related research that we have carried out along these lines. This work further develops a platform for future LC studies with Janus and Janus-like drops.

As indicated in the droplet morphology state diagram (see Fig. 5e; also consult **Section 2.3**), the detailed morphologies of Janus droplets are determined by the relative interfacial tension between three phases, which can be controlled by employing different types and amounts of surfactant molecules. For example, Fig. 12a and Fig. 12b shows how a change in surfactant type in the background aqueous phase leads to different droplet morphologies. Moreover, Fig. 12b, Fig. 12c, and Fig. 12d show that the drop morphology can be tuned by varying the volume ratio between

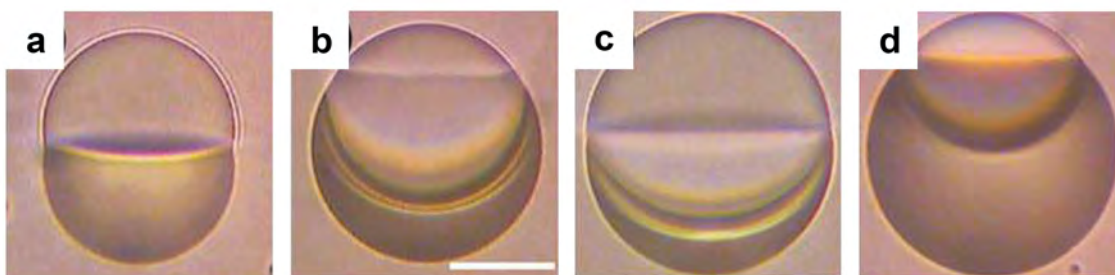


Figure 12: **Control Janus droplet morphology with different surfactants and compartment volume ratio.** The detailed morphologies of Janus droplets can be controlled by the type/concentration of surfactant in the water solution, and by the volume ratio between LC and PDMS. (Side-view) Exemplary nematic (5CB) droplets are demonstrated **a**, within a 0.1 wt% SDS solution and **b-d**, within a 0.1 wt% PVA solution. Drops with different LC to PDMS volume ratio are also shown: **a-b**, 1:1, **c**, 1:3, **d**, 3:1. The lower parts of droplets are the LC (5CB) compartments. Scale bar: 20  $\mu\text{m}$ . Note, these figures are initially created by Joonwoo Jeong and are adapted from Ref. [1].

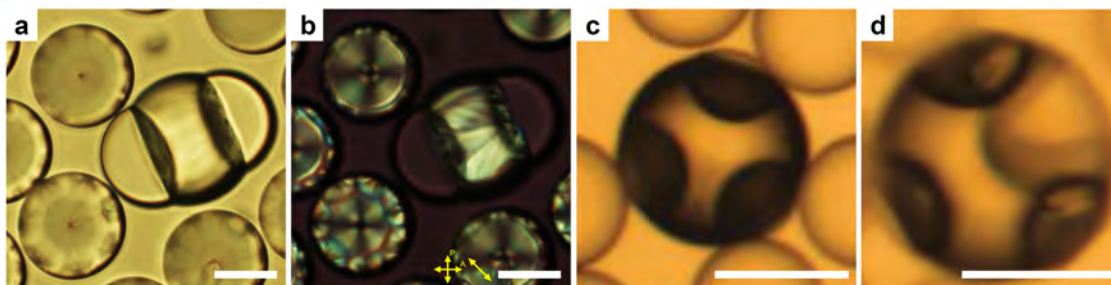


Figure 13: **Patchy liquid crystal droplets.** **a-b**, Bright-field and POM images of a (side-view) smectic patchy droplet and several (bottom-view) Janus drops. The patchy droplet is merged from two Janus drops with the 8CB to PDMS volume ratio set to be 1:1, suspended in a 0.5 wt% SDS solution. Scale bar: 30  $\mu\text{m}$ . **c-d**, Bright-field images of nematic droplets with 3 and 4 PDMS patches. The component Janus drops are with a 5CB to PDMS volume ratio set to 3:1, suspended in a 0.1 wt% PVA solution. Scale bar: 50  $\mu\text{m}$ . Note, images (c) & (d) were initially generated by Joonwoo Jeong and are adapted from Ref. [1].

LC and PDMS compartment.

In addition to managing shapes of Janus droplets, the coalescence of Janus drops provides a unique route to creating richer LC confinements. In particular, neighboring Janus drops could merge by coalescence of their LC compartments and evolve to patchy colloidal particles/droplets with various patch numbers. The resultant drops are thus LC droplets with two, three, or even four PDMS patches, as shown in Fig. 13. Interestingly, our preliminary experiments suggest that the multiple PDMS compartments in individual drop always repel each other, arranging the patches into equiangular coordinations. The observed repulsive interaction may arise from the elastic distortion of the underlying LCs, which has a similar mechanism as in the system we discuss in **Chapter 3**.

The demonstrated droplet morphologies are sensitive to the surfactant type/concentration in the background aqueous phase, the compartment volume ratio, and the coalescence of multiple Janus droplets. Manipulation of any/all of these factors enables synthesis of even more complex geometrical confinements for LCs in drops. Further characterization of the nematic and smectic LCs confined in these novel cavities and their associated texture/defect patterns will be subjects of future work.

## 2.9 Active Liquid Crystal Janus Droplets

Lastly, we briefly report on an unusual dynamical behavior of Janus droplets which arises from the anisotropic property of the two compartments. Previously, LC or oil drops dispersed in certain highly concentrated surfactant solutions were demonstrated to exhibit self-propelled motion; the mechanism for this self-propelled motion is believed to be related to the Marangoni stress [44, 45]. Briefly, the micelle-

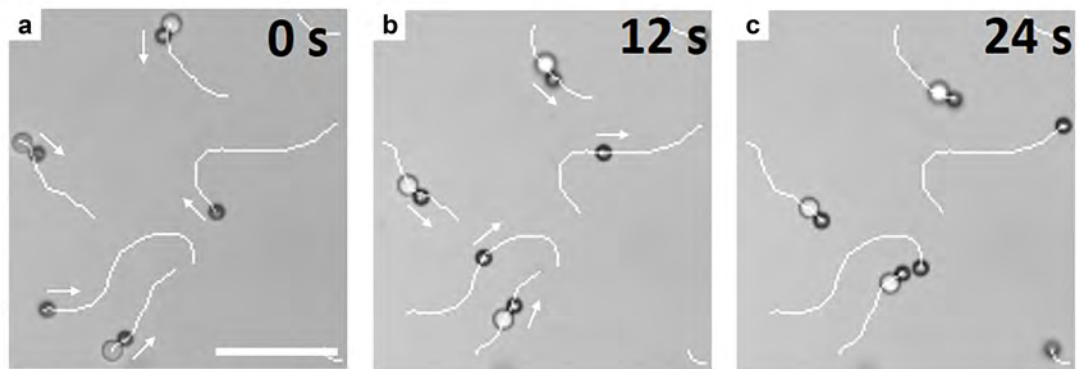


Figure 14: **Self-propelled motion of the nematic liquid crystal Janus droplets.** Dispersed in a 10 wt%  $C_{14}TAB$  solution, our nematic LC Janus droplets exhibit self-propelled motion at a speed of  $\sim 10 \mu\text{m/s}$ . The leading (and darker) parts of the Janus drops are 5CB compartments. Note, some detached nematic LC droplets are also shown in the field-of-view; they swim approximately twice as fast as the Janus droplets, but the direction of their motions is not well defined as in the Janus LC drop. The overlaid white solid lines and arrows indicate the droplet trajectories and directions of motion, respectively. Scale bar:  $100 \mu\text{m}$ . Note, these figures are initially created by Joonwoo Jeong and are adapted from Ref. [1].

assisted solubilization of dispersed materials (*e.g.*, LC or oil micro-droplets) in the background water phase leads to a spatial gradient in the packing fraction of adsorbed surfactant molecules on/around the drops, which in turn gives rise to Marangoni stress. The stress then promotes hydrodynamic flows both inside and outside the droplet and causes the swimming behavior.

Inspired by this mechanism and benefiting from the different solubilities of the nematic LC (5CB) and PDMS compartments of our Janus droplets, we are able to produce directional self-propelled motion. Specifically, we placed nematic LC Janus drops into the concentrated 10 wt% tetradecyltrimethylammonium bromide ( $C_{14}TAB$ ) solution, wherein the nematic LC compartment slowly dissolved into the water solution while the PDMS compartment remained inactive. Consequently, the self-propelled motion of LC Janus droplets is always directional; the drop is propelled

by the “truck-like” nematic LC compartment with the attached PDMS compartment as the “trailer” (Fig. 14). The reported dynamical behaviors could thus offer new avenues for applications of Janus colloids and active soft matter.

## 2.10 Summary and Future Directions

We created nematic and SmA LC Janus droplets, consisting of two immiscible compartments: PDMS and either the nematic LC 5CB or the smectic LC 8CB. We allowed the LC in the cavities to relax to its stable/metastable textures, and we experimentally analyzed the resulting textures and their relative free energies. With the help of POM, we observed a single surface boojum and a hedgehog point defect within nematic LC Janus drops with planar and homeotropic anchoring, respectively. By contrast, smectic LC Janus drops (with homeotropic anchoring) exhibit a much more complicated behavior. Three categories of smectic textures were recognized, including FCD flowers, dislocation rings, and undulations plus dislocation rings. All observed textures (either with or without topological defects) arise to fulfill geometric constraints and interfacial (homeotropic) boundary conditions. The frustration relief was driven primarily by the need to accommodate layer number mismatch between drop center and edge.

Importantly, the explored cavity geometry, boundary condition, and synthesis procedure lead to occurrence of a variety of *metastable* smectic textures. During formation of Janus drops, the fast and vigorous phase-separation process prevents the smectic from reaching its equilibrium state. Thermal annealing, on the other hand, drives the system towards lower free energy states. Evidently, the FCD flowers are the most energetically costly texture and are associated with larger LC-water interfacial

tension, while the texture with dislocation rings plus smectic layer undulations is energetically cheapest and is associated with smaller LC-water interfacial tension. For comparison, previous studies typically suggested that LCs confined in micro-emulsions would quickly settle into a single equilibrium configuration. Our findings are unusual in this respect and offer new routes for crafting sophisticated self-assembled structures of SmA LCs. Moreover, to the best of our knowledge, the only existing way to generate FCDs in suspended droplets requires interfacial *planar anchoring*. Ours is the first work to report on “geometry-driven” FCD textures in a homeotropic-anchored micro-emulsions, thereby expanding possibilities to study smectics in more complex confinements.

Looking to the future, the study of texture formation dynamics could teach us more about how smectic layers accommodate confinement geometries. Our preliminary observations suggested that the smectic textures always form and suffuse the entire cavity in a sequential manner (see Fig. 11e-f & Fig. 11g-j). More work is still needed to gain quantitative understanding of energetics of observed metastable textures as well as detailed packing rules for FCDs. Moreover, it would be interesting to explore how these smectic textures configure and reconfigure due to either external fields or tunable boundary conditions. Finally, the ability to precisely control LC defect/texture formation and evolution opens up new possibilities for assembling functional materials in a programmable arrangement.

# Chapter 3

## Liquid Crystal Properties from Interfacial Colloidal Dynamics <sup>2</sup>

### 3.1 Introduction

Creation of specific spatial arrangements of micron- and nanometer-size colloidal particles is an important feature of colloidal science. Colloidal crystals for example, can form thermodynamically as an equilibrium process or as a result of so-called directed assembly. Two-dimensional colloidal packings, in particular, occupy a special place in our community for a variety of reasons but perhaps mostly because they are model systems for study of hexatic phase which resides “between” a liquid and a crystalline solid. Colloidal particles at traditional liquid interfaces are known to form ordered and disordered structures driven by electrostatic [46, 47, 48, 49, 50], magnetic [51, 52, 53], and capillary forces [54, 55, 56, 57]. Liquid crystals (LCs) have also been employed to affect colloidal assemblies; interparticle interactions in this context are unusually interesting because they can be mediated by localized topological defects.

More specifically, particles at liquid crystal interfaces exhibit self-assembly driven by elastic interactions that arise in the underlying anisotropic fluid [58, 59, 60, 61, 62, 63]. For example, micron-sized colloidal particles form patterns on the LC-water/air interface ranging from hexagonal lattices to chain-like dipole structures [58, 61, 62, 63, 64]. Most of the previous work on these systems investigated the effects of anchoring conditions and geometry on colloidal structure formation. The dynamics associated with these structures, however, was largely unexplored until our work. Moreover,

---

<sup>2</sup>This chapter is based on our published work. In addition to this chapter, for details, interested readers might also want to consult the published paper Ref. [2].

though LC-induced particle potentials have been studied with optical tweezers in simple two-particle systems [63], the interparticle interactions characteristic of many-particle systems have never been measured.

In this contribution, which is published, we explore dynamics and packings of colloidal particles confined to the interface bounded on one side by air and on the other side by the thermotropic nematic liquid crystal (NLC) 4-cyano-4'-pentylbiphenyl (5CB). The resulting ensemble of colloidal particles differs qualitatively from other classic two-dimensional (2D) systems [46, 47, 48, 49, 51, 53] in that the interparticle forces are mediated via liquid crystalline defects which extend from under each particle into the bulk LC, *i.e.*, into the underlying semi-infinite medium. Thus, the experimental system offers a unique sample for study of 2D phase transitions, for study of exotic particle dynamics, and for study of crystal phonons and LC defect interactions in a regime wherein many-body effects can be important.

Here we employ video microscopy and particle tracking to measure short-time particle diffusion and vibrational phonon modes of the 2D crystals at the NLC-air interface. The full phonon density of states of the ordered lattice at the interface exhibits Debye behavior at low frequencies and van Hove-like singularities at higher frequencies. Sound velocities are readily extracted from the phonon dispersion relations, and interparticle interactions in the crystals are derived from the covariance matrix of particle displacements. All of these parameters are investigated as a function of temperature up to the nematic-isotropic LC transition. The variation of the resulting Brownian dynamics and potentials are consistent with the measured temperature dependence of 5CB elastic constants and viscosity [65, 66, 67, 68, 69, 70, 71, 72, 73, 74, 75].

Finally, qualitative observations of structural melting are reported. Information thus gained takes valuable steps towards using this class of particle ensemble at the NLC-air interface to probe phase behavior phenomenology of quasi-2D materials and

to probe properties of the underlying LC.

## 3.2 Method and Materials

### 3.2.1 Preparation of Colloidal Monolayers at Nematic Liquid Crystal Interfaces

The particle monolayer was made by trapping dry micron-sized silica particles at the interface between air and the bulk nematic phase 5CB following schemes described in Ref. [63]. Briefly, circular-shaped wells ( $\approx 1.5$  cm in diameter) were fabricated by mounting a spacer with thickness of  $100 \mu\text{m}$  onto a glass slide. The wells were then filled with the LC 5CB (Kingston Chemicals). Silica microparticles (nominal diameter  $d = 1.0 \mu\text{m}$ , Duke Standards) were surface-functionalized with dimethyloctadecyl [3-(trimethoxysilyl)propyl] ammonium chloride (DMOAP, Sigma-Aldrich; 5 wt% in a 1 : 9 by weight mixture of water and ethanol). This functionalization induces homeotropic anchoring of 5CB LC mesogens on the particle surfaces. After being aerosolized by an air pulse, the particles settled through the air and were adsorbed on the air-exposed surface of 5CB (see Fig. 15a). The bottom glass slide was also treated with a 5 wt% DMOAP solution for homeotropic anchoring.

The whole system was heated to the nematic-isotropic transition temperature,  $T_{NI} \approx 35 \text{ }^\circ\text{C}$ , for a short time and then cooled before the colloidal particles were spread. This heating-cooling scheme provides an opportunity for the LC mesogens to rearrange and helps to ensure uniform director alignment in the vertical direction within the bulk LC, *i.e.*, before particles are introduced. In total, these cautionary measures help to minimize alignment complications caused by the bottom well surface and by disorder that can arise during sample loading (*i.e.*, the procedures help to ensure uniform homeotropic alignment of the 5CB film as sketched in Fig. 15a).

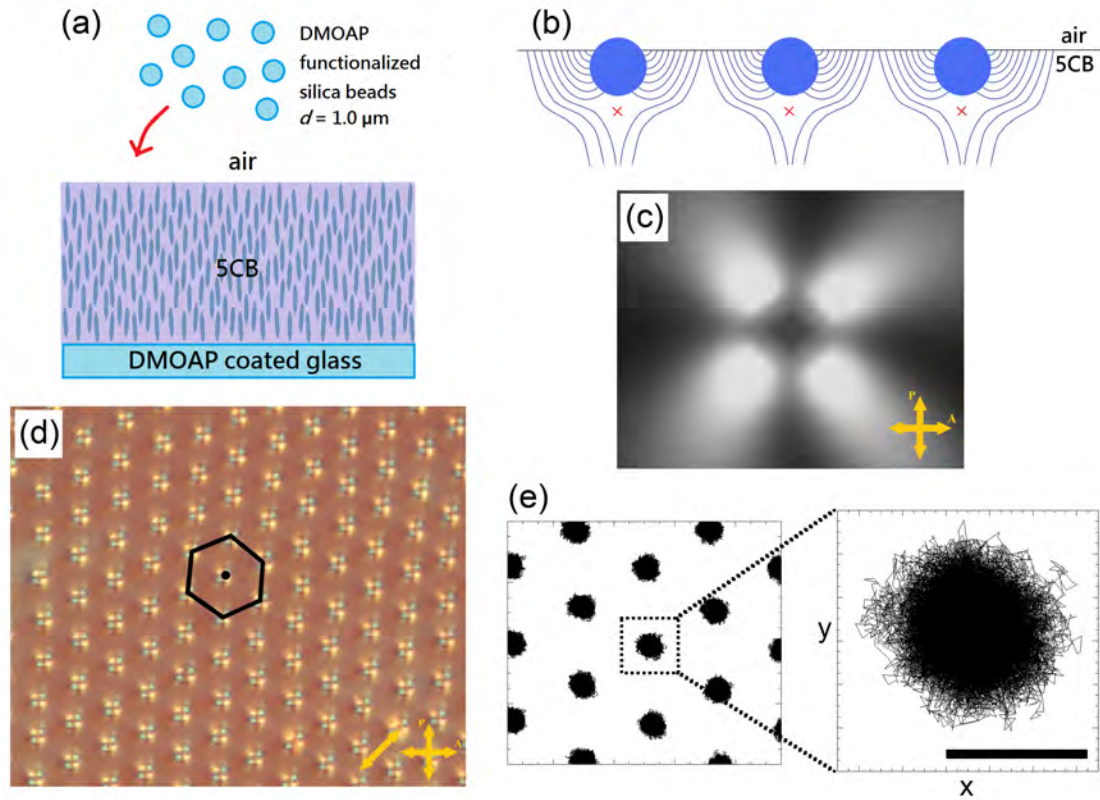


Figure 15: **Hexagonal colloidal lattices at the nematic-air interface.** **a**, DMOAP functionalized silica colloids spread at the air-5CB interface. **b**, The cartoon schematic depicts a possible local deformation of director alignment and a point hedgehog defect beneath each particle in the underlying LC. This cartoon is a faithful representation of the actual particle configuration, *i.e.*, with the majority of particles submerged. **c**, Under cross-polarizers and in the top-view, four bright lobes around each particle exhibit the optical effects of the radial alignment of LC mesogens (below the surface). **d**, Self-assembled hexagonal lattices form at large surface-particle density. Here the full-wave retardation plate is employed to distinguish northwest-southeast lobes (yellow/orange) and northeast-southwest lobes (blue), thereby further clarifying the local alignment of LC molecules. **e**, Trajectories of a few colloidal particles within the whole field-of-view are shown. The scale bar represents  $1 \mu\text{m}$ , and all particles have a diameter of  $1 \mu\text{m}$ .

Moreover, since the thickness of NLC film ( $\approx 50 \mu\text{m}$ ) is much larger than the colloidal particle diameter, the system dynamics are barely sensitive to the NLC film thickness and the analyses of the problem is simplified. A glass coverslip was also added over the well to minimize air flow effects.

After the microparticles settle at the air-NLC interface, defects form to satisfy anchoring conditions on the particle surface and at the air-NLC interface [76]. One possible director configuration (shown in Figs. 15b and 15c) is produced by a point defect beneath each particle.

Macroscopic ordered patterns of such particles spontaneously form after the samples stabilize over a few days. This particle self-assembly arises from an interplay between long-range LC-mediated interparticle elastic repulsion and a very weak gravitational confinement induced by the curved interface near the well edge. The weak gravitational confinement, in particular, ensures that a large surface-particle density is maintained.

Our experiments focus primarily on properties of particles in the resulting 2D hexagonal crystal (see Fig. 15d), which typically occupies  $\approx 20\%$  of the sample well area. Grain boundaries and defects sometimes arise too and thus further sub-divide the crystalline region into smaller “domains” with cross-sections of approximately several hundred micrometers. The temperature of the system is controlled by an indium tin oxide coated glass heating stage with mounted thermocouple. Most of the measurements were carried out at temperatures below  $T_{NI}$  of 5CB.

When the LC undergoes a phase transition from the nematic to the isotropic phase, the aligned nature of LC mesogens vanishes, which in turn leads to the disappearance of defects. As a result, LC-mediated long-range interparticle repulsive forces disappear. This effect causes the crystalline hexagonal pattern to melt as shown in Fig. 16. Once the LC is in the isotropic phase, the colloidal particles experience un-

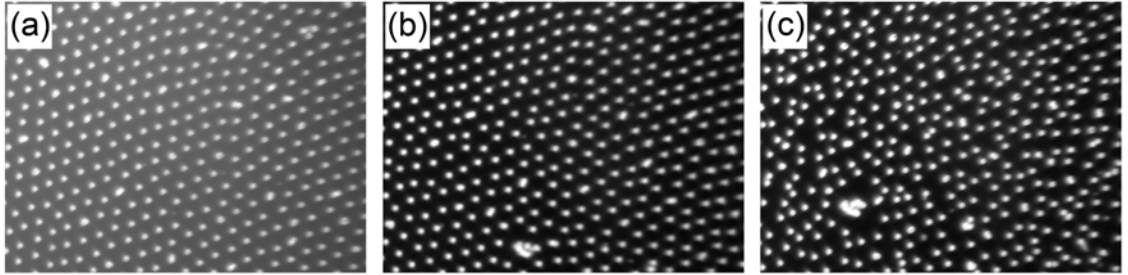


Figure 16: **Hexagonal colloidal lattices melt upon nematic-isotropic phase transition.** As the temperature increases, the underlying LC 5CB undergoes a phase transition from **a**, an orientationally ordered nematic phase (temperature below  $T_{NI}$ ) to **b**, a disordered isotropic phase (temperature above  $T_{NI}$ ). The corresponding LC-mediated interparticle repulsive forces weaken and eventually vanish due to loss of mesogen alignment, and concurrently, **c**, the crystalline hexagonal pattern of colloids begins to melt a few seconds after the phase transition temperature is reached. Particles have a diameter of  $1 \mu\text{m}$ .

constrained Brownian motion but eventually aggregate when particles come into close contact. This aggregation at very short range is possibly caused by weak capillary attractions between particles due to a very small deformation of the interface [77] around isolated beads, but it could also be due to other more direct interactions or combinations thereof.

### 3.2.2 Optical Microscopy and Particle Tracking

Sample wells were observed with a Leica DMRXA optical microscope in bright-field, dark-field, and polarization modes. Leica N Plan 10x, Leica PL Fluotar L 63x, and Leica PL APO 100x objectives were used. Crossed-polarizers and full-wave retardation plates were deployed in the microscope to characterize director configurations around the colloidal particles.

Sample images were acquired at 22 frames per second using dark-field video mi-

croscopy. Approximately 80,000 frames were utilized for most of the analyses. The only exception was the data set for the study of short-time particle diffusion; in that case, data was taken more rapidly, *i.e.*, at 110 frames per second with  $\approx 2,000$  frames in total. Higher frame rates are needed to resolve short-time diffusive behavior. Approximately 750 particles are contained within the field-of-view, *i.e.*, wherein data were acquired, which corresponds to approximately 2,250 nearest-neighbor particle pairs. Trajectories of colloidal particles in the field-of-view were obtained via standard particle tracking techniques [78]; a typical particle trajectory is shown in Fig. 15e.

### 3.2.3 Displacement Covariance Matrix Method

We employed the displacement covariance matrix method [79, 80, 81, 82, 83] to derive vibrational (phonon) properties of our dense particle packing. Briefly, we extracted displacement vectors,  $\mathbf{u}(t)$ , from the track file. This vector contains the displacement components of each particle in each frame (*i.e.*, at each timepoint,  $t$ ), measured with respect to its equilibrium (steady-state) position. The time-averaged displacement covariance matrix,  $C$ , was calculated as follows:

$$C_{ij} = \langle u_i(t)u_j(t) \rangle_t \quad , \quad (3.1)$$

where  $i, j$  denote particle numbers as well as coordinate components (*i.e.*, x and y directions in 2D). In the harmonic approximation, the stiffness matrix  $\kappa$  is related to  $C$  by

$$\kappa_{ij} = k_B T (C^{-1})_{ij} \quad , \quad (3.2)$$

where  $k_B$  is the Boltzmann constant and  $T$  represents the temperature. Its elements  $\kappa_{ij}$  give the effective spring constants between particles  $i$  and  $j$ , including both x- and y-components. In the past [79, 80, 81, 82, 83], this analysis has been employed for isolated systems. However, for lattice structure with boundary confinements (*e.g.* our case), the effect of stress in the system must also be considered [84, 85]. In this case, the x- and y-components for each particle pair  $\alpha, \beta$  are extracted from the elements  $\kappa_{ij}$  using a  $2 \times 2$  submatrix:

$$\bar{\kappa}_{\alpha\beta} = \begin{bmatrix} \kappa_{\alpha\beta}^{xx} & \kappa_{\alpha\beta}^{xy} \\ \kappa_{\alpha\beta}^{yx} & \kappa_{\alpha\beta}^{yy} \end{bmatrix} . \quad (3.3)$$

Diagonalizing  $\bar{\kappa}_{\alpha\beta}$  gives two sets of eigenvalues and eigenvectors; one set is directed along the bond  $b$  between particle pair (denoted as  $\kappa_{eff}$ ) while the other set has direction perpendicular to the bond (denoted as  $\sigma_t/r$ ). The former (parallel) eigenvalue is the effective spring constant for this specific colloidal particle pair, and the latter (perpendicular) eigenvalue is related to the stress divided by the center-to-center separation of the two interacting particles,  $r$ .

Finally, we obtain the dynamical matrix,  $D_{ij}$ , of the system from

$$D_{ij} = \frac{\kappa_{ij}}{m} , \quad (3.4)$$

where  $m$  is the particle mass. Diagonalization of  $D_{ij}$  gives the eigenvalues and eigenvectors of the vibrational phonons of the system. (Note, the system characterized by this procedure is the so-called shadow particle system with the same interactions and geometry as the experimental system, but absent damping.) We encourage the interested reader to consult Refs. [79, 80, 81, 82, 83] for details about the method, including its strengths and limitations [86, 87, 88, 89]. To our knowledge, the present

analysis is the first to incorporate the effects of confinement stresses. The eigenvalues of the dynamical matrix are the square of the eigenfrequencies,  $\omega$ , of the phonon modes, and the eigenvectors indicate the displacement amplitude for each particle associated with each mode. The accumulated number of modes,  $N(\omega)$ , is defined as the number of vibrational modes with frequency less than or equal to  $\omega$ , and the derivative of  $N(\omega)$  with respect to  $\omega$  is the phonon density of states (DOS), *i.e.*, the number of vibrational modes per unit frequency (energy) interval.

In carrying out this covariance procedure, caution must be taken because several factors can introduce errors. All of these procedures have been carefully described by Chen *et al.* [90]. Notably, we use a linear extrapolation method [83] to account for the effects of finite sampling on the mode frequencies.

### 3.3 Probing Liquid Crystal Viscosity via Short-time Particle Diffusions

Once fabricating the system, we first report on its diffusion dynamics. We calculated the particle mean square displacement (MSD) from the individual trajectories as shown in Fig. 17a. The plateau at long time delays is caused by spatial caging of particle motion due to its local hexagonal confinement cage in the ordered structure. At the early times we expect the MSD to grow linearly with time, and, indeed, the particles at the air-NLC interface exhibit fairly linear short-time MSD curves.

We varied temperature, and we fit the short-time MSD at each temperature to derive temperature-dependent Brownian dynamics (Fig. 17b). The linear fits gave the short-time diffusion coefficient,  $\mathfrak{D}$ , as a function of temperature (Fig. 17c). The observation that  $\mathfrak{D}$  increases with temperature is sensible; higher temperature implies

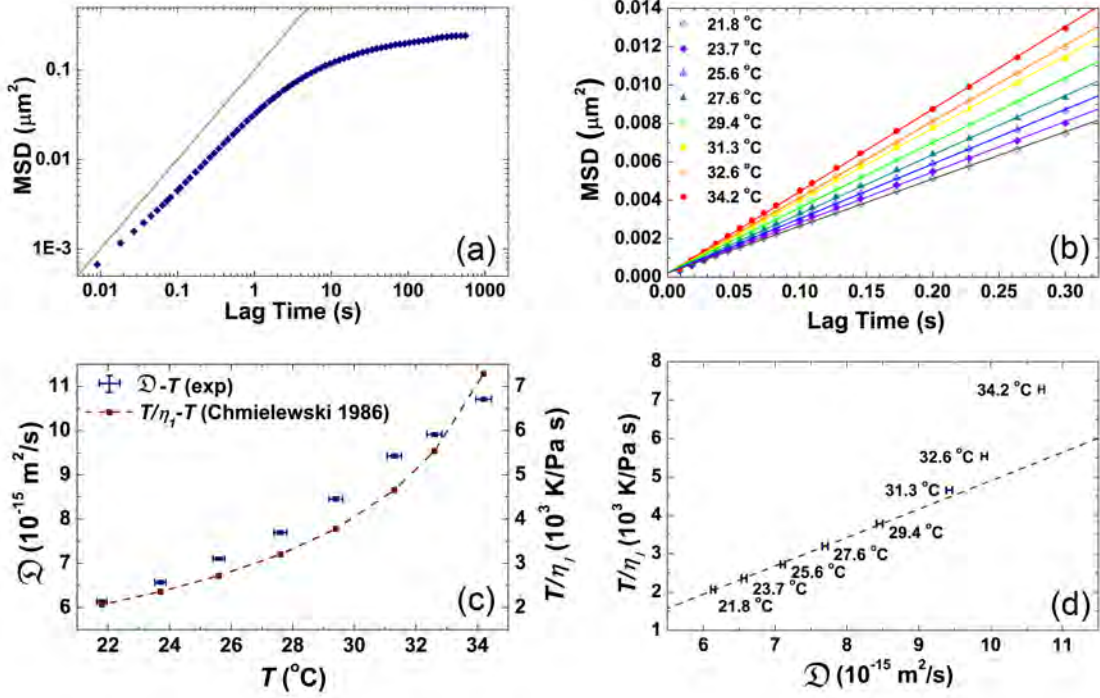


Figure 17: **Short-time diffusion behavior of colloidal particles at the nematic interface.** **a**, The mean square displacement (MSD) is calculated from colloidal particle trajectories. At short times, diffusive behavior is observed (MSD grows linearly with time; the grey solid line has slope = 1). The plateau at long time intervals is caused by lattice caging effects. **b**, The linear fit of the short-time MSD at each temperature gives **c**, a corresponding short-time diffusion coefficient,  $\mathfrak{D}$ , as a function of temperature (blue dots with error bars);  $\mathfrak{D}$  increases with increasing temperature. The dark-red dashed curve shows  $T/\eta_1$  as a function of temperature from previous work [70]. **d**, A linear correlation between  $\mathfrak{D}$  and  $T/\eta_1$  is exhibited over most of the temperature range probed, confirming a Stokes-Einstein model; deviation from linearity is evident when the temperature approaches the nematic-isotropic transition.

weaker elastic forces and viscosity and thus faster diffusion. To quantitatively explain this tendency, we apply a very simple model that assumes particle diffusion at the interface is dominated by the bulk LC. In this case, the diffusion coefficient is described by the Stokes-Einstein relation [91],

$$\mathfrak{D} = \frac{k_B T}{6\pi R \eta} \quad , \quad (3.5)$$

where  $\eta$  is the viscosity of 5CB, and  $R$  is the colloidal particle radius. Generally, for diffusion in a LC, the anisotropic nature of the viscosity should be considered [92, 93, 94], and an anisotropic drag force is predicted [95, 96, 97]. However, the particle motions in the present situation are largely in-plane, and therefore we need only consider the viscosity  $\eta_1$  for which the LC director is perpendicular to the direction of particle motion and parallel to the direction of velocity gradient. This approach, while approximate, is sensible because the particle motions are restricted in 2D by the air-NLC interface.

As a further check we note that because colloidal particles do not distort the shape of LC interface significantly, the Young equation should still provide guidance for the behavior of the anisotropic liquid [77]. (Note, although the NLC with homeotropic anchoring yields a modified Young equation [98], the air-5CB interfacial energy is large enough to justify neglect of the modified term.) In this case, the vertical position of colloids is simply controlled by the contact angle between silica particle and the air-5CB interface. Taking account the balance between tension forces at the three-phase contact line (particle-air, particle-LC, and air-LC interface), and including the effects of gravity and buoyancy, the geometric calculation gives a contact angle  $\approx 33$  degrees, which, further, agrees well with experimental measurements via surface profiler [77]. This contact angle then implies that more than 90% of the particle volume is immersed

in 5CB. For these reasons, it is plausible that a single LC viscosity could dominate the drag force for the particles, *i.e.*, Eq. (3.5) should capture most of the diffusion physics. For comparison, we also show the dark-red dashed curve in Fig. 17c,  $T/\eta_1$ , plotted as a function of temperature [70]; it follows roughly the same trend as our experimental diffusion coefficient data (blue dots with error bars).

Assuming a linear correlation between  $\mathfrak{D}$  and  $T/\eta_1$ , the linear fit gives  $R \approx 0.54 \mu\text{m}$  as shown in Fig. 17d, a value close to the actual particle size  $R = 0.5 \mu\text{m}$ . Note, here we have taken one value of  $\eta_1$  for our calculation [70] while the measured viscosity values of 5CB vary somewhat across all previous work [69, 70, 71, 72, 73, 74, 75]. Of course, different  $\eta_1$ 's will give slightly different fitted  $R$ 's. Further, we observed a deviation from linearity when the temperature approaches the nematic-isotropic transition. This deviation can be explained by a possibly larger hydrodynamic particle radius caused by a comparatively stable surface-induced orientationally-ordered layer near the colloid-LC interface [99]. Alternatively, a temperature-dependent effective viscosity arises from different vertical positions of particles at the interface; these position variation could be induced by changing surface tension forces with increasing temperature, *i.e.*, that produce a different weighting between LC and air viscosities.

Thus, the short-time particle diffusion dynamics of our system are revealed to follow a bulk Stokes-Einstein relation with the temperature dependence of  $\eta_1$  following that of bulk nematic 5CB. Ultimately, the air-exposed part of particle and interfacial effects should be considered for more precise analyses. For comparison, a single homeotropic anchored particle in its bulk nematic counterpart exhibits a slightly smaller diffusion coefficient than our experimental measurement at the air-NLC interface, possibly due to a larger effective viscosity. The difference is within 20% [96, 97]. Note also, the 3D Stokes-Einstein model is an approximation, and, ideally, it should be modified with a correction factor that accounts for the interface [100].

### 3.4 Phonon Density of States and Dispersion Relations

As noted in the Method and Materials section, the phonon modes of the collective system with hexagonal order were calculated from the colloids' displacement correlations [79, 80, 81, 82, 83]. From this data we derive the phonon density of states (DOS) as a function of frequency  $\omega$ . According to Debye model, the DOS of a crystal should scale as  $\omega^{n-1}$  at low frequencies, where  $n$  is the dimension of the system [101]. Therefore, in the case of a 2D crystal, the DOS should grow linearly with the phonon frequency. The DOS of the 2D hexagonal lattice of particles at the air-NLC interface indeed follows the Debye model at low frequencies, as shown in Fig. 18a.

In the higher frequency regimes, the DOS deviates from Debye scaling and displays two peaks that are remnants of van Hove singularities (Fig. 18a). These features arise from transverse and longitudinal vibrational modes at the edge of the first Brillouin zone; they have been observed in other 2D colloidal crystal experiments with different interaction potentials [90, 101, 102].

Using the solutions of  $D(\omega)$ , we also calculated the phonon dispersion relation  $\omega(q)$  for the system, where  $\mathbf{q}$  represents the phonon wave vector. We extract  $\omega(q)$  by Fourier decomposition of eigenvectors along high-symmetry crystallographic directions. The details of the method are described in the literature [103, 104] and were recently applied to soft colloidal crystals [90] and glasses [105]. The phonon dispersion relation for our crystal is shown in Fig. 18b. Slopes of the transverse and longitudinal branches in the long-wavelength limit near the center of the Brillouin zone give the transverse and longitudinal sound velocities,  $c_T = 24.0 \pm 0.4$  mm/s and  $c_L = 60.2 \pm 0.4$  mm/s, respectively (see Fig. 19). The group velocity for both branches becomes zero

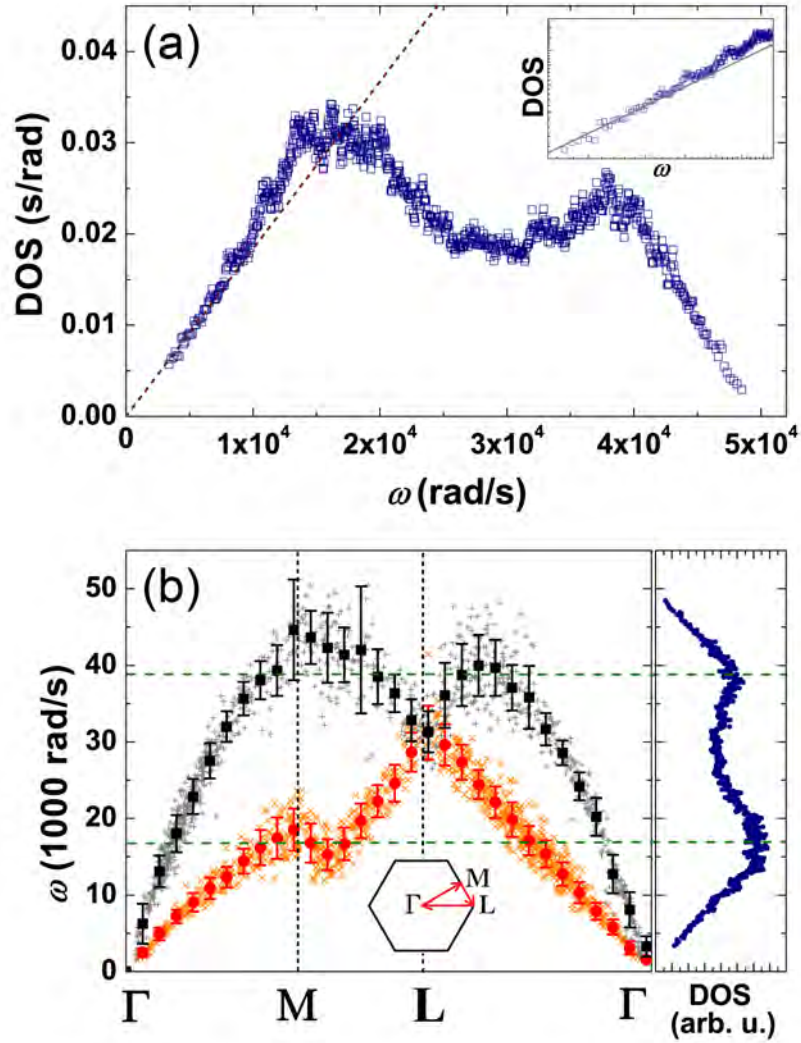


Figure 18: **Vibrational density of states and dispersion relations of the colloidal packings.** **a**, The vibrational density of states (DOS) of the hexagonal crystals of particles at the air-NLC interface is shown as a function of frequency  $\omega$ . At low frequencies, the DOS grows approximately linearly with phonon frequency, *i.e.*, the Debye scaling  $\text{DOS} \propto \omega$ . In higher frequency regimes, the DOS deviates from Debye scaling and displays remnants of van Hove singularities. Inset: For the regime where  $\omega < 1.5 \times 10^4$  rad/s, the data is re-plotted with both axes logarithmically scaled. The grey solid line has slope = 1, which is predicted by the Debye model. **b**, Dispersion curves for transverse (red/orange) and longitudinal (black/grey) modes along high-symmetry directions, including raw data (crosses) and binned data (solid circles and squares with error bars). The DOS plot is shown again for easy comparison of frequencies. The measurement was performed at room temperature, 21.8 °C. Inset: High-symmetry directions in reciprocal space.

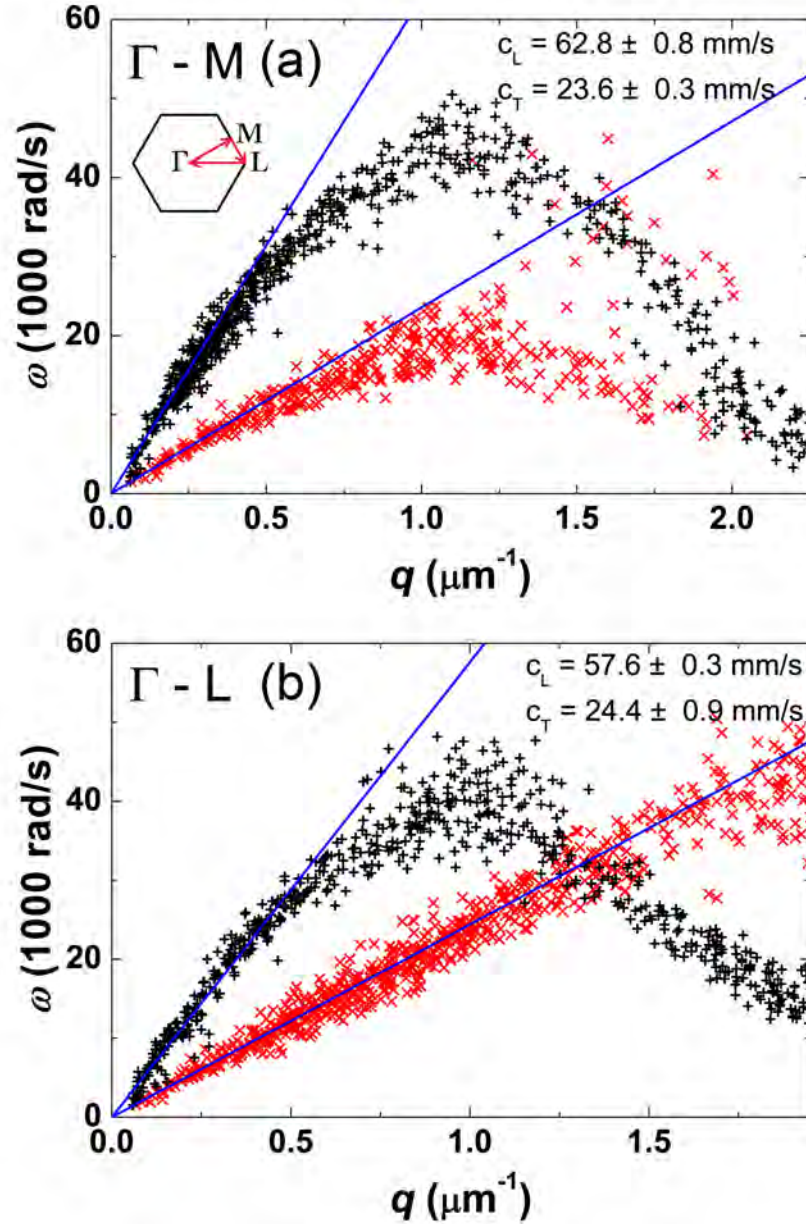


Figure 19: **Dispersion relations and sound velocities of the colloidal packings.** **a**, Dispersion curves for transverse (red) and longitudinal (black) modes along one of the two high-symmetry directions,  $\Gamma$ -M. The blue solid lines are the linear fits for linear dispersion (*i.e.*, low frequency) regimes, whose slopes give the sound velocities  $c_T = 23.6 \pm 0.3$  mm/s and  $c_L = 62.8 \pm 0.8$  mm/s, respectively. **b**, The same process is applied to direction  $\Gamma$ -L and gives  $c_T = 24.4 \pm 0.9$  mm/s,  $c_L = 57.6 \pm 0.3$  mm/s. Inset: High-symmetry directions in reciprocal space.

at the edges of the Brillouin zone, and the frequencies wherein these features are observed correspond to those of the van Hove singularities in Fig. 18a.

With these sound velocities at hand, we are able to perform other self-consistency checks. For example, according to the Debye model, for a 2D system [106]

$$\text{DOS}(\omega) \equiv \frac{dN(\omega)}{d\omega} = \frac{L^2}{2\pi c^2} \times \omega \quad , \quad (3.6)$$

where  $L^2$  is the area size of the system and  $c$  is the sound velocity. Eq. (3.6) assumes  $c_T$  and  $c_L$  are the same, but in practice they are often different. For both the transverse and longitudinal branches, substitution of the system size and the calculated sound velocities gives a slope of  $(19.6 \pm 0.3) \times 10^{-8} \text{ s}^2/\text{rad}^2$  and  $(123.4 \pm 4.1) \times 10^{-8} \text{ s}^2/\text{rad}^2$ , respectively, for the low frequency linear dispersion in the corresponding DOS plots. Their sum can be tested against our experimental low frequency DOS curve (Fig. 18a). Indeed, the calculated slope of  $(143.0 \pm 4.1) \times 10^{-8} \text{ s}^2/\text{rad}^2$  is close to the one obtained from the experimental fitting,  $(183.6 \pm 1.5) \times 10^{-8} \text{ s}^2/\text{rad}^2$ , as shown by the dark-red dashed line. Small deviations may arise due to the anisotropic nature of the sound velocities within these crystals, but the data quality does not justify their consideration at this time.

### 3.5 Interparticle Interactions in The Crystal

Line defects (disclinations) and point defects (hedgehogs) are singular regions within nematically ordered media. In the NLC bulk with homeotropic boundary conditions at two ends of planar cell, the director field is uniform. By analogy with electrostatics, the total topological charge in this case is zero. When a spherical particle with homeotropic anchoring is added into the system, a topological +1 charge

is introduced and distortions of the uniform field arise to satisfy anchoring constraints on the particle surface. Since the director field in the cell is uniform at large distance, the nematic creates a defect of charge -1, *i.e.*, a point defect (hyperbolic hedgehog) or a line defect (Saturn ring) to compensate the particle's +1 charge.

The elastic interactions between particles in bulk LCs have been understood, calculated [145], and checked by experiment [107, 108, 109]. However, the situation for colloidal particles at air-NLC interfaces is more complex and less studied. In fact, the forces between particles at interfaces are still debated, with different studies describing and observing different interaction behaviors [58, 59, 60, 61, 63, 110, 111].

Our displacement covariance experiments provide measurements of  $\kappa_{eff}(r)$  for the silica particles in the hexagonal lattice at the air-NLC interface (see Eqs. (3.2) and (3.3)). Ideally, the form of the interparticle potential may be directly assessed from measurement of  $\kappa_{eff}$  as a function of  $r$  at fixed temperature. Further, since the temperature can be varied, the same procedure can be carried out repeatedly at different temperatures to explore effects of the temperature-dependent elastic coefficients of 5CB. From the covariance matrix method, the calculated  $\kappa_{eff}(ij)$  are the spring constants between particles with different center-to-center separation and with boundary confinement. In principle, one can obtain information about interactions between first nearest neighbors, second nearest neighbors, etc.

Here, due to signal-to-noise limitations, we focus only on adjacent particles, *i.e.*, the nearest neighbor particles. Further, although a weak gravitational confinement was introduced to maintain large surface-particle density in the central region of the sample, the central region is large and flat. Therefore, we neglect gravity and the curved interface near the well edge in our analysis; had the curvature of LC surface within the field-of-view been significant, then the interparticle separations would have varied smoothly within the field-of-view [63]. By sampling over the full field-of-view

and checking the pair correlation functions, we confirmed that no systematic tendency exists for variation of interparticle separation,  $r$ . Currently, we have no evidence to indicate that other interparticle attractions, *e.g.*, that have been discussed and debated in previous work exist in our system [60, 61, 58, 59, 110].

Combining data from different temperatures, we plot the effective spring constant versus interparticle distance (Fig. 20). Note, we plot  $\kappa_{eff}T/K$  versus  $r$ ; the temperature  $T$  and the elastic coefficient  $K$  are included to normalize temperature effects that arise between data from different measurements (see **Section 3.6** for  $K$  values used). Also, since we observed deviations from linear correlation between  $\mathfrak{D}$  and  $T/\eta_1$  when the temperature approached the nematic-isotropic transition, we only include data for the lowest five temperatures shown in Fig. 17d.

Previous experiments on this system class measured the interaction between two isolated particles with optical tweezers [63]. Here we aim to use displacement correlations to quantitatively demonstrate the dominant form of interaction between colloidal particles in the dense packings at the air-NLC interface. Unfortunately, as shown in Fig. 20, the dynamic range of particle separation,  $r$ , is quite small. Thus, differentiation between various interaction models using these data is very difficult. In the plot we show the best fitting which gives a power law with exponent of  $-3.43 \pm 2.41$ . Power laws of  $-5$  and  $-7$  arising, respectively, from dipole-only and quadrupole-only interactions lie within the error bars of our data. Therefore, the data is not of sufficient quality to make claims about the form of the interaction between particles; neither the simple dipole form, nor the simple quadrupole form, nor other complex forms convincingly describe the data. We must leave such determinations to future work which can acquire data offering a much larger dynamic range of  $r$ .

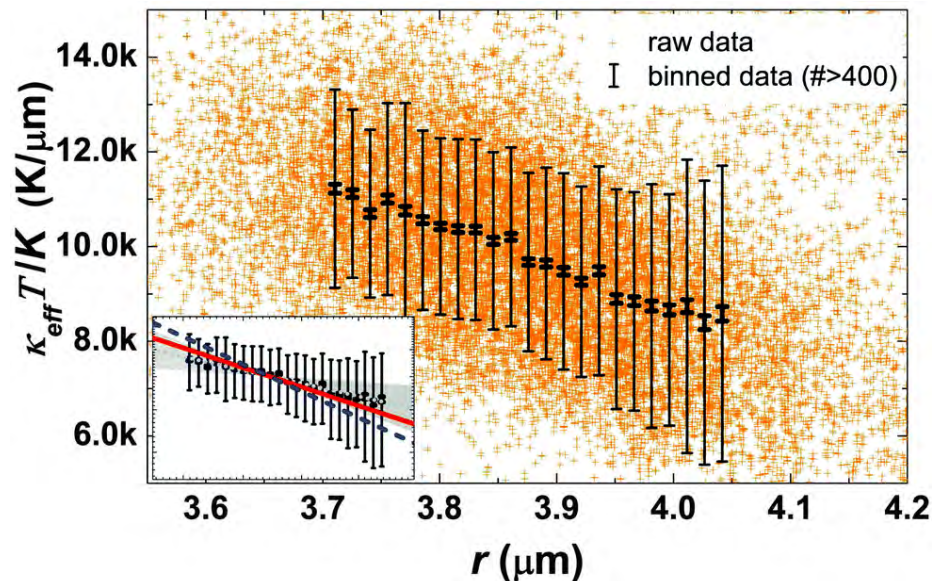


Figure 20: **Effective spring constant with respect to interparticle separation.** The effective spring constant  $\kappa_{eff}$  (together with corresponding normalization factors  $T$  and  $K$ ) between adjacent particles for the lowest five temperatures in Fig. 17d is plotted as a function of interparticle separation  $r$ . The orange crosses exhibit raw data, and the black error bars represent the average  $\kappa_{eff}T/K$  values, standard deviations (thin lines), and standard errors (thick lines) within each 0.1 pixel bin with a filtering condition that insures only bins with more than 400 data points are recorded. Inset: The binned data is re-plotted with both axes logarithmically scaled. Grey shadow region shows the best linear fit, a power law of  $-3.43 \pm 2.41$ . The quadrupole only ( $-7$ , blue dashed line) and dipole only ( $-5$ , red solid line) power laws are also presented.

### 3.6 Interparticle Interactions as a Function of Temperature & Liquid Crystal Elastic Constant

Though we were unable to determine the exact form of the interparticle potential, our experimental measurement still enables investigation of the temperature dependence of  $\kappa_{eff}$  (effective spring constant) and  $\sigma_t/r$  (stress divided by the center-to-center interparticle separation). We explored these variations with temperature. The average value of the spring constant,  $\kappa_{eff}$ , was obtained from data at each tem-

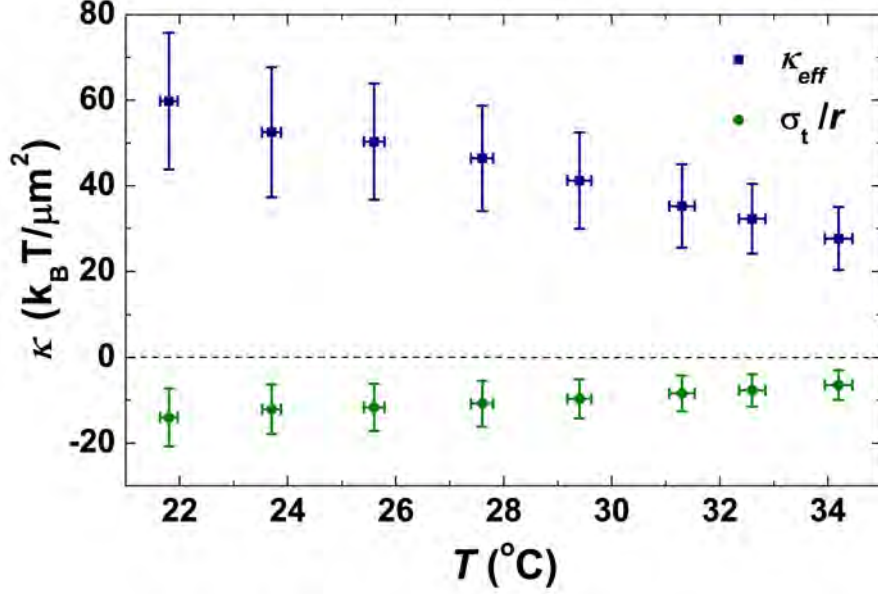


Figure 21: **Effective spring constant and stress as functions of temperature.** Our measurement of the average stiffness of the effective spring,  $\kappa_{eff}$ , is shown with the blue squares as a function of temperature. The green circles show the stress term,  $\sigma_t/r$ , as a function of  $T$ .

perature as the system evolved towards the nematic-isotropic transition. The blue squares in Fig. 21 show that the stiffness of effective springs decreases with increasing temperature in this range. Note, the vertical “error bars” do not represent measurement errors; rather, they are the standard deviation of  $\kappa_{eff(ij)}(T)$  when fitted to a Gaussian distribution.  $\sigma_t/r$  is also expressed as a function of  $T$  (green circles) and is shown to decrease in magnitude as temperature increases.

Quantitatively,  $\kappa_{eff}$  is the second derivative of the potential energy of the spring on bond  $b$  while  $\sigma_t/r$  is the derivative of potential divided by interparticle separation [85]. Since the potential is proportional to the temperature-dependent elastic coefficient  $K$  [145, 111], the spring constant  $\kappa_{eff}$  (as well as the stress term  $\sigma_t/r$ ) is expected to be temperature-dependent.

The LC’s effective spring constant is proportional to  $K$ . Previous work provides

experimental data which exhibits an approximate relation between elastic coefficients and temperature. The primary results are expressed through the dependence of the splay ( $K_{11}$ ), twist ( $K_{22}$ ), and bend ( $K_{33}$ ) elastic coefficients of 5CB as a function of the order parameter  $S$  [65], which in turn depends on temperature [69]:

$$K_{11} = 5.98 \times S^{2.15} \quad , \quad (3.7)$$

$$K_{22} = 2.70 \times S^{1.96} \quad , \quad (3.8)$$

$$K_{33} = 11.78 \times S^{2.65} \quad , \quad (3.9)$$

$$S = \left( 1 - \frac{T}{T_{NI} + 0.25} \right)^{0.18} \quad . \quad (3.10)$$

We employ the one-constant limit of the Frank free energy to keep the calculation simple [145]. A single elastic coefficient of 5CB,  $K$ , may be used in the theory; in practice, we use the arithmetic mean of 5CB splay, twist, and bend elastic coefficients for  $K$ . Note, in our system, the LC twist likely has only a minor effect. Thus, another possible way to do these calculations is to neglect  $K_{22}$  and take the arithmetic mean of  $K_{11}$  and  $K_{33}$  to derive  $K(T)$ . This latter approach causes  $K$  to increase by a factor of  $\approx 1.3$ . It does not alter the main observed trends, but it will change the fitted coefficients for the potential.

Following Eqs. (3.7)-(3.10), we plot the one-constant approximated elastic coefficient versus temperature as the dark-red dashed curve in Fig. 22. The figure again shows our experimental spring constant data ( $\kappa_{eff}$ ) versus temperature for reference. Since measurements of the elastic coefficients of 5CB vary somewhat for those reported in previous publications, we also reproduce the experimental measurements from different work [65, 66, 67, 68, 69] as black dotted curves in the plot. Comparing

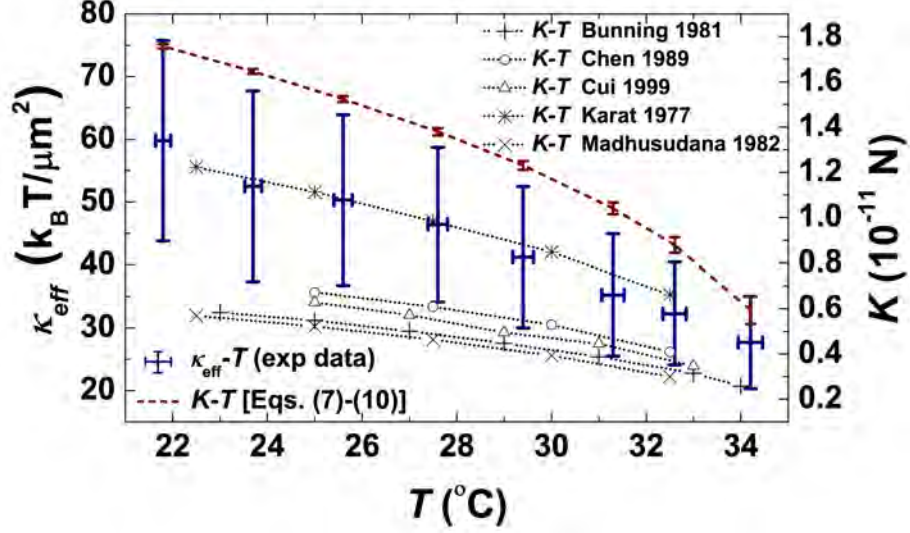


Figure 22: **Correlation between effective spring constant and liquid crystal elastic constant.**  $\kappa_{eff}$  data (shown in Fig. 21) is re-plotted; the dark-red dashed curve gives the one-constant approximated elastic coefficient,  $K$ , versus temperature following Eqs. (3.7)-(3.10). Experimental measurements of  $K$  from previous work are also reproduced on the plot as black dotted curves [65, 66, 67, 68, 69].

the general tendencies of these curves, the positive correlation between  $\kappa_{eff}$  and  $K$  is apparent.

This result can be understood qualitatively when one considers the effect temperature has on the nematic order and elastic energy of the LC. As the temperature increases, the nematic order and elastic energy of the LC decrease. As the nematic order and elastic energy decrease, the interaction between particles mediated by the LC medium weakens, *i.e.*, the effective spring constant between particles decreases.

Here we use the temperature dependence of elastic coefficients to explain our observations about the behavior of the temperature-dependent effective spring constant. Alternatively, this general formalism also provides an approach to assess the value of  $K$ . For example, when the exact potential form (*i.e.*, the relation between  $\kappa_{eff}$  and  $K$ ) are resolved via the method described in **Section 3.5**, then simply performing

the covariance procedure can lead to measurement of LC elastic coefficient. Notice, however, almost all current theories employ the one-constant limit of the Frank free energy; thus this method provides average  $K$  instead of individual  $K_{11}$ ,  $K_{22}$ , and  $K_{33}$ .

### 3.7 Particle-free Domains and Silica Micro-cubes at Nematic Liquid Crystal Interface

We have discussed the structure and dynamics of colloidal monolayer packings at the nematic-air interface. In this section, we briefly report on two related observations which are worth exploring in the follow-up experiments

The first set of observations concerns “clean” regions without particles that were sometimes observed within the interfacial 2D hexagonal colloidal lattices (see Fig. 23). The particle-free region exhibits a hexagonal shape with both rounded and sharp corners. Occasionally, we observed a single particle trapped at the structural center or the particle-free hexagon. These surprising assembly patterns could be associated with “impurities” adsorbed at the nematic-air interface. The contaminant, for example, could be residual DMOAP molecules used for colloid/glass treatment or the dirt (pollution) suspended in air. The adsorbed contaminant at the 5CB-air interface then prohibits particles from occupying the region on the surface. The hexagonal shape of the clean region, on the other hand, suggests a connection to the hexagonal symmetry of the lattice elsewhere on the sample interface. At this point, the origin of this behavior is a mystery that should prove interesting to understand.

In our second set of experiments, we replaced the spherical particles trapped at the 5CB-air interface with micron-sized silica colloidal cubes. The hollow and nano-porous silica cubic colloids were synthesized in three steps, following schemes

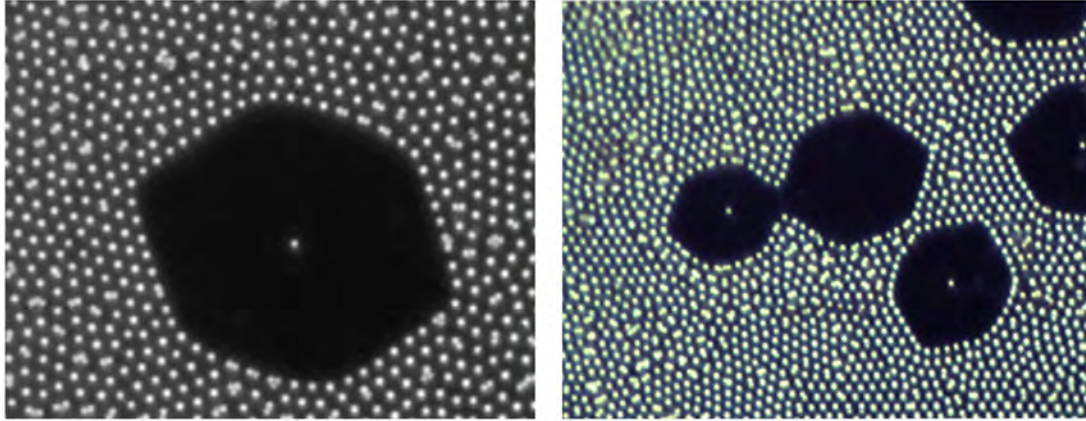


Figure 23: **Hexagonal particle-free region within the 2D colloidal particle lattice packings.** Dark-field images of a particle-free (clean) region at the sample interface within the 2D hexagonal colloidal lattice. Occasionally, a single particle was found trapped at the structural center of the particle-free region. These regions could originate from impurities absorbed at the nematic-air interface, but at present we do not have evidence for this effect. Particles have diameter of  $1.0 \mu\text{m}$ .

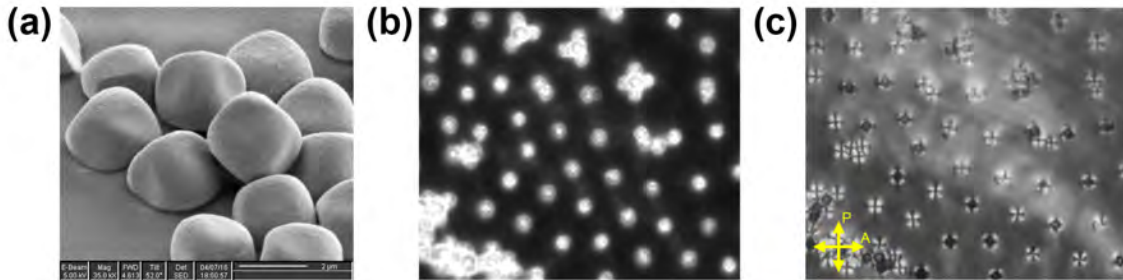


Figure 24: **Packings of silica colloidal cubes at the nematic-air interface.** **a**, Scanning electron microscope (SEM) image of exemplary hematite micro-cubes. Scale bar:  $2 \mu\text{m}$ . **b-c**, Dark-field and POM image of self-assembled hexagonal lattice of colloidal micro-cubes at the 5CB-air interface (with the same field-of-view). The cubes have size around  $2.3 \mu\text{m}$ .

described in Ref. [112, 113]: (1) syntheses of hematite micro-cubes (Fig. 24a); (2) creation of templated hematite cubes with an amorphous silica shell; (3) dissolution of hematite core by hydrochloric acid. These silica micro-cubes were then aerosolized by an air pulse and adsorbed onto the air-exposed surface of 5CB, as described in **Section 3.2.1**.

As exhibited by Fig. 24b-c, the micro-cubic colloids self-assemble into hexagonal lattice. This lattice is similar to the packings formed by spherical micro-particles. Though it has been reported that complex LC defect structures could emerge around colloidal cubes (compared to spheres) embedded in nematic [114, 115], we did not observe evidence of such (different) interparticle interactions in our preliminary experiment. A potential explanation is that the contributions from faceted colloidal boundaries are weak, perhaps because of the large interparticle separation or the round corners/edges of micro-cubes. The cubes trapped at the interfaces could also behave differently from cubes in the bulk. Further work is needed to further characterize the system.

## 3.8 Summary and Future Directions

We have created self-assembled monolayers of particles at the air-NLC interface and have analyzed the diffusion and vibrational phonon modes of crystalline packings of colloidal particles. These measurements provide quantitative insight about the LC-defect-mediated interparticle interaction effects. On short timescales, the particles exhibited diffusive motion with diffusion coefficients consistent with a Stokes-Einstein model wherein the effective viscosity is predominantly that of 5CB. The phonon density of states (DOS) exhibited Debye scaling at low frequencies and van

Hove-like singularities at higher frequencies. The dispersion relations for transverse and longitudinal vibrational modes, and their corresponding sound velocities, were also calculated. Moreover, the dependence of these interactions on particle separation was quantitatively analyzed, but the data did not permit accurate determination of potentials. Finally, the temperature dependence of these interparticle forces was consistent with expectations based on previous (temperature-dependent) measurements of the splay, twist, and bend elastic moduli.

In the process of performing this research, we also explored the temperature dependence of the phonon behavior. A rough analysis shows that the range of eigenfrequencies becomes wider, and the distribution of effective spring constants broadens as the system temperature decreases (see Fig. 25a). Some of these observations are sensible. The effective spring constant, for example, becomes larger with decreasing temperature due to an increase in magnitude of the elastic constants; this effect, in turn, should lead to an increase in the full frequency range of the DOS (see Fig. 25b). Other possible sources of increased broadening include increased disorder induced by factors such as non-uniform particle wetting and slow relaxation of LC-particle contact lines [116] especially at lower temperatures. The resultant heterogeneities could thereby contribute to the observed distribution broadening of effective spring constants and DOS.

Moreover, the data also suggests that the system has a broader distribution of nearest-neighbor interparticle separations at lower temperatures, *i.e.*, even though the basic hexagonal symmetry of the lattice persists. Further, sound velocities in the crystal are observed to decrease with increasing system temperature. At higher temperature, smaller effective spring constant is consistent with a lattice containing weaker bonds between neighboring particles, which gives rise to smaller sound velocities. These phenomena deserve more attention and should be explored in future

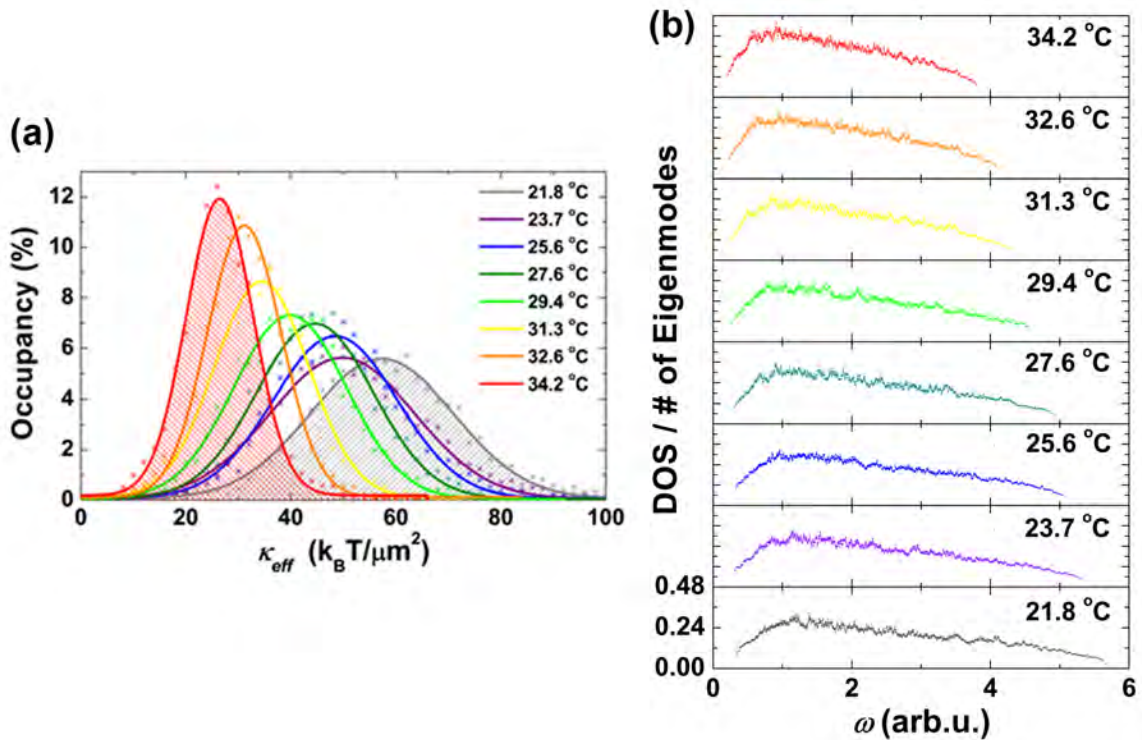


Figure 25: **Temperature dependence of the phonon behavior.** Our temperature-dependent study shows that as the system temperature decreases, the range of eigenfrequencies becomes wider, which arises from the distribution broadening of effective spring constants as shown in the plot. The effective spring constant becomes larger with decreasing temperature, since the elastic constants increase with decreasing temperature. This effect, in turn, leads (at least in part) to **a**, a shifting (and some broadening) of the  $\kappa_{eff}$  distribution and thus to **b**, a broader width for the DOS with respect to frequency. Moreover, several mechanisms may also induce such disorder, including non-uniform wetting (caused by uneven DMOAP functionalization or uneven surface roughness of colloidal particles) and slowly-relaxed contact lines of colloids at interfaces. The hypothesis is that, since the relaxation is slower at lower temperature due to a larger LC viscosity, the contact line needs more time to relax and would be slightly more “zigzag” (caused by non-uniform wetting) when we observed. The resultant heterogeneities could then contribute to a broadening of the  $\kappa_{eff}$  distribution.

experiments.

Looking to the future, the 2D system we have created and studied offers new ways to explore interesting questions. For example, with improvements and larger system size, it should be possible to investigate phase transitions and possible hexatic states in a new class of 2D crystal mediated by elastic defects that penetrate asymmetrically into the surrounding media. In a different vein, using other types of LCs or particles, it should be possible to create situations wherein the particles submerge less into the LC; in this case, variation in particle diffusion will be interesting to study. More work is needed to understand the phonon DOS variation with temperature, which at least partially reflects quenched disorder (albeit while maintaining the hexagonal lattice); this scenario potentially offers an experimental technique for study of connections between phonon spectra and disorder.

Finally, experiments with better signal-to-noise, for example due to larger dynamic range of particle separations, are needed for precise determination of interparticle potentials. Setups such as a wedge-shaped well with capability of changing LC level could be employed for this purpose. The ability to vary lattice spacing provides us with the possibility to check for attractive interactions and to investigate how crystal vibrational behavior is altered by different interparticle separations.

# Chapter 4

## Self-shaping Liquid Crystal Micro-emulsions<sup>3</sup>

### 4.1 Introduction

Most liquid crystal (LC) research we have described thus far either focuses on how to tune and control the molecular alignment of the LC constituents, or on how to employ the LCs (LC alignment) to assemble colloidal particles at an interface (**Chapter 2** and **Chapter 3**). In this chapter we focus on a different phenomenon. In particular, we study the effects of the competition between bulk LC elasticity and interfacial tension in drops containing LC oligomer mixtures. We discover that these effects can lead to spectacular self-organization or “shape transitions” of LC micro-emulsion drops; the drops start spherical and evolve to acquire highly non-trivial internal and external structure.

Briefly, it is well known that the shapes of liquid drops depend on the balance between interfacial energy and bulk energy. In our daily life, droplets containing isotropic liquid (*e.g.*, water and oil) are most often spherical because spheres minimize interfacial energy at fixed bulk volume; the system bulk energy is not considered because it is usually independent from geometry. The spherical shape can be changed, however, by filling or covering the drops with selected materials. Liquid crystalline materials, in general, happen to be ideal candidates for the trick because of their significant bulk anisotropic elasticities, which vary with confinement size and geometry. Once the interfacial tension is no longer dominant, *i.e.*, with reduced contribution

---

<sup>3</sup>This chapter is based on our published work. In addition to this chapter, for details, interested readers might also want to consult the published paper Ref. [3].

from interfacial tension, the anisotropic LC bulk elasticity then becomes more important for determining drop shape, increasing the potential for spontaneous shape transitions as detailed in the following sections.

In the work presented in this chapter (which is published), the consequences of molecular heterogeneity on nematic liquid crystal oligomer (NLCO) drops in *equilibrium* are revealed to promote reversible shape transitions to a rich variety of non-spherical morphologies with unique internal structure. Surprisingly, polydispersity of the LC oligomers does not destroy order, as it often does in inanimate matter; rather, polydispersity drives remarkable and reversible shape transitions of the drop. Note, heterogeneity in traditional materials can induce subtle effects [121, 122, 123], but most often polydispersity tends to disrupt order and impede self-assembly and state transformation.

Previously, shape transitions of homogeneous liquid drops with *monodisperse* ingredients have been reported in equilibrium [124, 125, 126, 127, 128, 129] and *non-equilibrium* studies [130, 131, 132], with the latter producing filaments at active interfaces, albeit randomly without control. Our experiments employ suspended drops composed of *polydisperse* NLCOs. We find that variation of oligomer chain length distribution, temperature, and surfactant concentration alters the balance between NLCO elastic energy and interfacial energy, and drives formation of these nematic structures that range from roughened spheres to “flower” shapes to branched filamentous networks with controllable diameters. The branched structures with confined LC director fields can be produced *reversibly* over areas of at least one square centimeter and can be converted into liquid crystal elastomers (LCEs) by ultraviolet (UV) curing.

Remarkably, observations and modeling reveal that *chain length polydispersity* plays a crucial role in driving these morphogenic phenomena, via spatial segregation.

This insight suggests new routes for encoding network structure and function in soft materials.

## 4.2 Method and Materials

Our experiments employ NLCO drops, tens of micrometers in diameter, dispersed in water containing sodium dodecyl sulfate (SDS) surfactant. SDS creates a strong preference for homeotropic anchoring, wherein the nematic director (molecular orientation) is perpendicular to the drop surface (Fig. 26a). Each surfactant-stabilized NLCO emulsion contain a mixture of 1,4-bis-[4-(6-acryloyloxyhexyloxy)benzoyloxy]-2-methylbenzene (RM82) monomers and RM82 oligomers [133] with variable chain lengths (Fig. 26a, see Fig. 27a for details of chain length distribution). Importantly, compared to small molecule LCs, chain length *polydispersity* of the NLCOs offers new degrees of freedom which can profoundly affect drop morphology, and the NLCOs are readily crosslinked to lock-in nematic morphologies.

### 4.2.1 Synthesis of Nematic Liquid Crystal Oligomer Drops

The employed NLCO emulsions were made in three steps: (1) preparation of emulsion drops containing monomer / chain-extender mixtures and suspended in an aqueous phase; (2) oligomerization within individual drops to link LC monomers together into liquid crystal oligomers (LCOs); (3) creation of final NLCO drop suspensions in water, which are observed by video microscopy as a function of temperature.

#### **Step 1: Preparation of emulsions containing precursors.**

A 1:1 mixture of 1,4-bis-[4-(6-acryloyloxyhexyloxy)benzoyloxy]-2-methylbenzene (monomer RM82, Wilshire Technologies) and n-butylamine (chain-extender, Sigma-

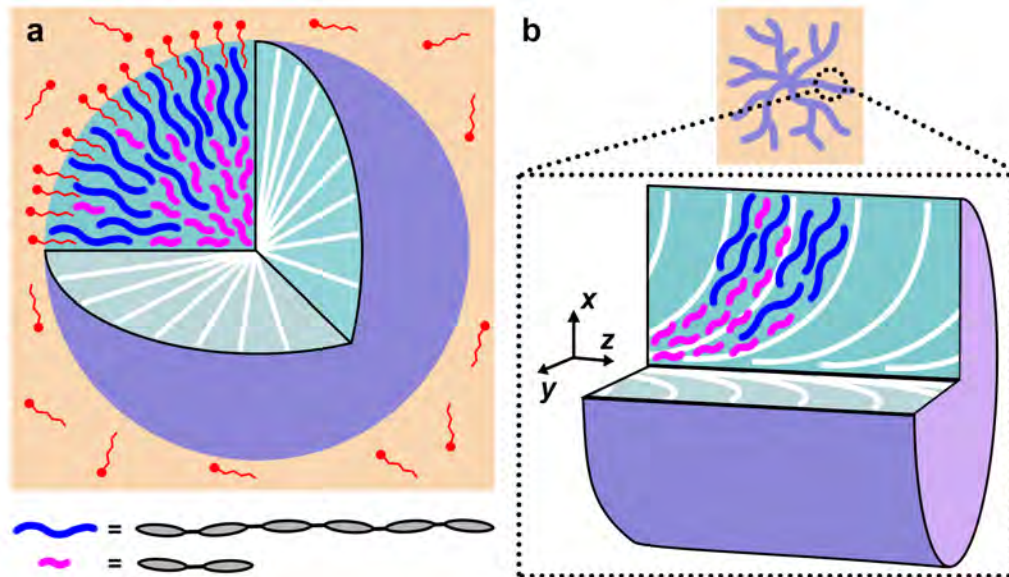


Figure 26: **Schematics of nematic liquid crystal oligomer drop and filament suspended in water solution.** **a-b**, The schematics depict a surfactant-stabilized NLCO sphere and filament (purple) in a background aqueous phase (orange). White lines on cross sections represent nematic director. The concept of spatial segregation by oligomer chain length is illustrated. Inset: For simplicity, long-chain/short-chain species (blue/pink solid tilde) are represented by hexamers and dimers, respectively (grey ellipses represent monomers). The  $z$ -axis in **(b)** is parallel to the filament axis pointing away from structural center.

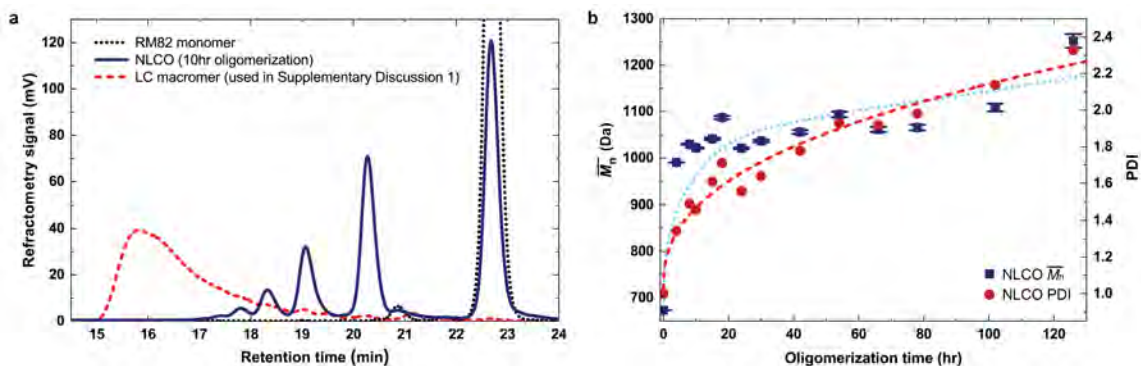


Figure 27: **Chain length (molecular weight) distribution of nematic liquid crystal oligomer samples measured by size exclusion chromatography (SEC).** **a**, The NLCO source samples are shown to be a mixture of monomers, dimers, trimers, tetramers, and other oligomers (blue solid line, peak appearing at longer retention time represents shorter chain length). In step-polymerization processes, when the extent-of-reaction is less than 0.9, then monomers dominate the overall molar fraction. For comparison, LC macromers (used in the supporting experiment in **Section 4.6.4**) synthesized following the schemes of Ware et al. [133] are also included in the plot; the latter show longer mean chain length and very few (if any) short-chain components (red dashed line). Furthermore, since our system is made in an aqueous solution, the polymerization rate is expected to be slower. For reference, the black dotted line shows the peak for pure RM82 monomer. **b**, Calculated from SEC data (example in **(a)**), the number-average molecular weight ( $\overline{M}_n$ , blue solid square) and polydispersity index (PDI, red solid circle) of the NLCOs are shown as function of oligomerization time. Both  $\overline{M}_n$  and PDI increase with oligomerization time. The dotted (for  $\overline{M}_n$ ) and dashed (for PDI) curves are to guide the eye. (For comparison, the LC macromer synthesized following the schemes of Ware et al. [133] and used in **Section 4.6.4** has  $\overline{M}_n \approx 6,900$  Da and PDI  $\approx 1.3$ .)

Aldrich) was dissolved in chloroform (Fisher Scientific); weight of chloroform is 3x the weight of RM82. A 0.2 wt% (by RM82 concentration) antioxidant, butylated hydroxytoluene (BHT, Sigma-Aldrich), was also added.

The resulting organic phase mixture was then made into a micro-droplet emulsion in an aqueous solution. This was achieved by adding surfactant to the mixture of water and organic-phase and then shaking to create polydisperse drops with diameters ranging from 10 to 100  $\mu\text{m}$ . Three different types of surfactant were employed: negatively charged sodium dodecyl sulfate (anionic surfactant SDS, Sigma-Aldrich), positively charged hexadecyltrimethylammonium bromide (cationic surfactant C<sub>16</sub>TAB, Sigma-Aldrich), and neutral polyoxyethylene (20) sorbitan monolaurate (Tween 20, Fisher Scientific). Although phenomena with SDS surfactant is reported in most of the work, experiments using the other two surfactants exhibited behavior similar to that of SDS-based systems; spontaneous shape transitions are not restricted to a certain type of surfactant. However, in considering surfactants, it is important that homeotropic anchoring of the NLCOs is still favored. All chemicals were used as received, without further purification or modification. At this stage, the suspended drops contain unchained monomers.

## **Step 2: Oligomerization within drops.**

The RM82 / n-butylamine (chain-extender) / chloroform – SDS / water droplet suspension is next placed in a water bath at 90 °C for oligomerization. During this process, the organic solvent (chloroform) evaporates completely from each emulsion drop, and then the n-butylamine begins to link the diacrylate RM82s in chains via a self-catalyzed “aza-Michael addition” reaction. Afterward, resultant emulsion drops are composed of main-chain LCOs. The degree of oligomerization (*i.e.*, the mean oligomer chain length  $\langle \ell \rangle$ ) is controlled by reaction time.

We note that the LCO chain length distribution is broad and has a shorter mean

oligomer chain length,  $\langle \ell \rangle$ , compared to previous liquid crystal elastomer work [133] (see Fig. 27).

### **Step 3: Cooling of the Nematic liquid crystal oligomer drops.**

After the reaction, a small volume of the suspension (*i.e.*, the NLCO emulsion) is pipetted into a pre-heated glass well, sealed with coverslip and glue, and then cooled to 20 °C on a hotplate at a rate of -1 °C/min. The suspension is then annealed (*i.e.*, quickly re-heated to 90 °C and then slowly cooled to 20 °C again) before the drop morphology experiments are carried out.

Note, compared to pure RM82 monomer, which forms a nematic only above 86 °C (nematic in the 86-116 °C temperature range), the present LCOs exhibit a wide nematic window that extends below room temperature (*i.e.*, at least between 20-90 °C).

## **4.2.2 Drop Morphology Characterization**

Sample cells containing NLCO drops were observed with a Leica DMIR13 inverted optical microscope in bright-field and polarization modes. Leica N Plan 10x, Leica PL Fluotar L 63x, and Leica PL APO 100x objectives were used. Crossed-polarizers and full-wave retardation plates were deployed in the microscope to characterize director configurations within the drops.

## **4.2.3 Molecular Weight Measurements of Liquid Crystal Oligomers**

To further characterize the LCO samples, most of the remaining emulsion solution was centrifuged (2,000 relative centrifugal force, RCF) at 15 °C and washed with

deionized (DI) water several times to remove surfactant. It was then vacuum dried to remove water.

Part of the resultant bulk sample was then dissolved in tetrahydrofuran (THF; stabilize with 250 p.p.m. BHT, Alfa Aesar) at a concentration of 1.5 mg/mL for molecular weight analyses. The molecular weight analyses were performed using standard size exclusion chromatography (SEC, Tosoh Bioscience EcoSEC) with flow rate of 1.0 mL/min and with three analytical columns in series: TSKgel G2000HXL, TSKgel G2500HXL, and TSKgel G3000HXL. A standard polystyrene sample (MW = 48,100 Da, Sigma-Aldrich) was also added during the SEC measurements for calibration purposes.

#### 4.2.4 Macroscopic Interfacial Tension Measurements

The interfacial tension between the NLCO drop surfaces and the background aqueous phase were measured macroscopically using the pendant drop method [134, 135]. The pendant drop technique works by carefully analyzing the shape of a large (millimeter-size) liquid drop hanging from a capillary tube (*i.e.*, the flat tip syringe needle), when it is about to detach from the capillary tube. The shape of the hanging drop depends on gravity, on cohesive forces of the drop within the background medium, and on the interfacial tension.

Our pendant drop tensiometry employs a homemade temperature-regulated chamber, which enabled us to measure the system interfacial tension as a function of temperature. Each target NLCO bulk sample was injected into a syringe coupled with a flat tip needle. The pendant NLCO drop was made in a 0.1 wt% SDS water solution in the temperature-regulated chamber. High contrast images of the drop contour were obtained while the temperature was slowly decreased. The densities of the bulk

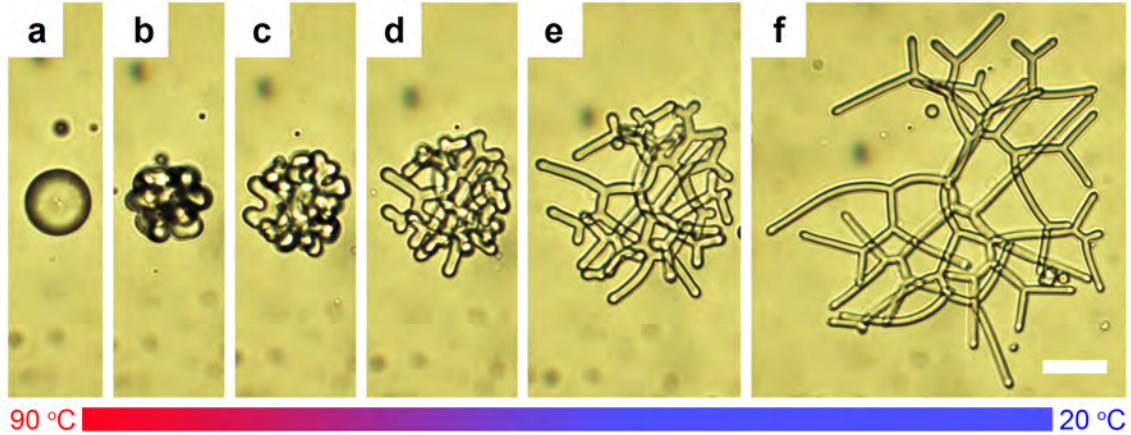


Figure 28: **Spontaneous shape transition of nematic liquid crystal oligomer drops.** **a-f**, A surfactant-stabilized NLCO drop in a background aqueous phase spontaneously (and reversibly) evolves from sphere to an extended filamentous drop as temperature is reduced. Scale bar is 20  $\mu\text{m}$ .

NLCO were also measured at the different temperatures. Finally, using the methods and software created by Daerr et al. [135], we fitted the drop contour for each sample at each temperature using the densities of the bulk NLCO and of the surrounding medium. With this information, the interfacial tension can be deduced.

### 4.3 Reversible Drop Shape Transition via Temperature Cycling

As a short reminder, here we study NLCO drops dispersed in water containing SDS surfactant. Essential features of the drop shape transitions are shown in Fig. 28. At a high temperature ( $\sim 90$  °C), while still in the nematic phase, the NLCO drop is spherical (Fig. 28a, see also Fig. 26a). In this situation, interfacial energy is large compared to bulk director elastic energy. Upon cooling, the surface tension and bulk elasticity vary, and excess interface is created. This interplay destabilizes the drop,

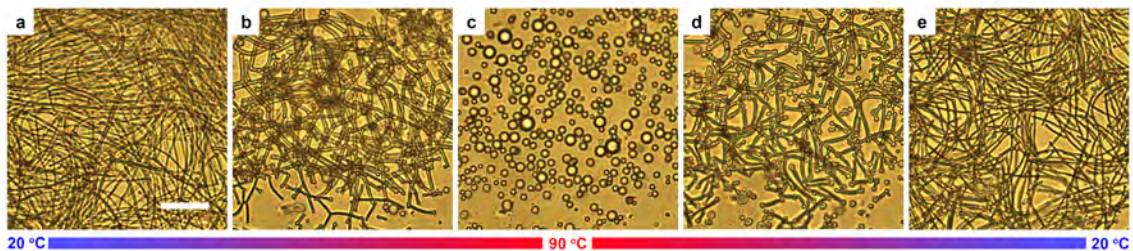


Figure 29: **Reversible shape transitions of nematic liquid crystal oligomer drops during temperature cycling.** **a-c**, When temperature increases from room temperature (20 °C) to higher temperatures (*e.g.*, 90 °C), the NLCO filamentous structures reversibly evolve back into spherical micro-droplets. **c-e**, Then, during re-cooling, the spherical micro-droplets evolve back into filamentous structures. The drop morphology can be transformed repeatedly, remaining quantitatively similar. Here, multiple small drops evolve in the field-of-view; data in **Fig. 28a-f** showed only one large evolving drop. Scale bar: 20  $\mu\text{m}$ .

facilitating spontaneous polymorphic transitions to non-spherical *equilibrium* structures (see exemplar images in Fig. 28a-f; see corresponding director configuration schematics in Fig. 26a-b; interested reader can also consult Supplementary Video 1 of Ref. [3] or check the online version <https://www.nature.com/articles/s41586-019-1809-8>). These polymorphic shape transitions are reversible and repeatable via temperature cycling (see Fig. 29; interested reader can again consult Supplementary Video 2 of Ref. [3] or check the online version <https://www.nature.com/articles/s41586-019-1809-8>).

Arguably, the major factor driving these shape transitions is the interfacial tension,  $\gamma$ , which decreases with decreasing temperature. This trend was confirmed in pendant drop experiments using large, *millimeter-size* NLCO drops (Fig. 30; check experimental details in **Section 4.2.4**), and it has been reported in other systems [129, 136, 137]. The decrease in  $\gamma$  is believed to arise from greater molecular ordering at the interface [129, 136, 138, 139]. In our case, surfactant-induced anchoring and the stronger alignment of NLCOs at lower temperatures enhance interfacial ordering.

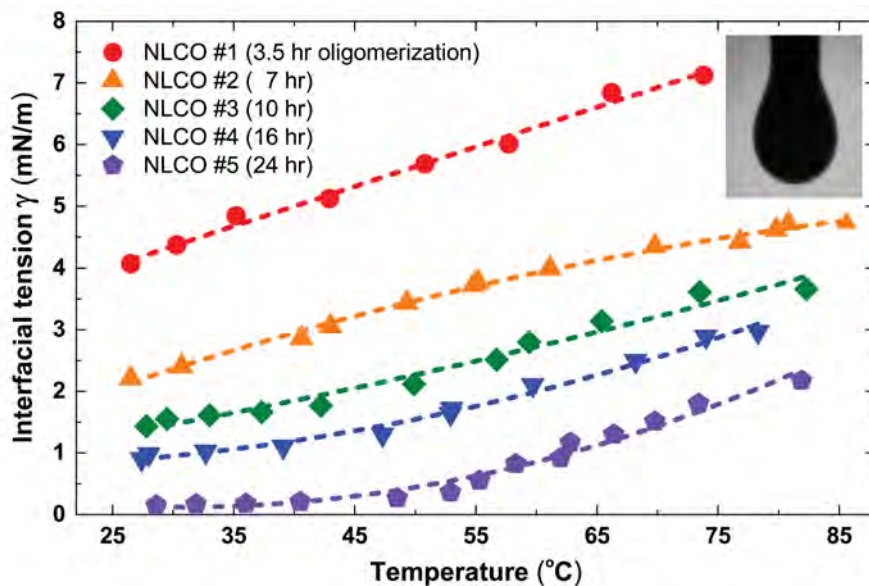


Figure 30: Macroscopic interfacial tension of nematic liquid crystal oligomer pendant drops as function of temperature and oligomerization time (oligomer mean chain length). The NLCO drop has homeotropic anchoring at the interface in an aqueous solution consisting of 0.1 wt% SDS. The interfacial tension  $\gamma$  decreases with decreasing temperature and increasing NLCO mean oligomer chain length  $\langle \ell \rangle$  (consult **Fig. 27b** and **Fig. 31f** for relation between oligomerization processing time and  $\langle \ell \rangle$ ). Inset: Optical image of a NLCO pendant drop hanging from a flat tip syringe needle (1.26 mm OD) in a 0.1 wt% SDS aqueous solution.

Additionally, NLCO elastic constants increase with decreasing temperature [140]. Thus, with reduction of  $\gamma$ , the anisotropic bulk elasticity becomes more significant in determining drop shape, increasing potential for spontaneous shape transitions [124].

## 4.4 Equilibrium Drop Morphologies as a Function of Mean Oligomer Chain Length and Surfactant Concentration

To elucidate the consequences of these competing effects, we constructed a morphology “state” diagram from samples that experienced the same heating-cooling cycles. Fig. 31a-d exhibit the repeatable drop morphologies: smooth/roughened spheres, flowers, large and small diameter ( $d$ ) filament networks. The “state” diagram is shown in Fig. 31e as a function of surfactant concentration and mean oligomer length,  $\langle \ell \rangle$ , which increases with total oligomerization time.

Consider the effects of NLCO average chain length. Though all samples are poly-disperse, the samples prepared with longer oligomerization processing times contain a larger ratio of long-chain to short-chain oligomers and have longer  $\langle \ell \rangle$  (Fig. 31f). Larger NLCO elastic constants are expected for longer  $\langle \ell \rangle$  [141, 142]. Interfacial oligomer assembly with longer  $\langle \ell \rangle$  also tends to reduce  $\gamma$  (see Fig. 30); longer NLCOs increase oligomer chain hydrophobicity, which induces more ordered interfacial molecular packing [143, 144]. These trends favor drop morphologies with large surface area at lower temperatures. More quantitatively, the measurements indicate a crossover transition to non-sphericity occurs when  $\langle \ell \rangle \approx 1.5$  times the monomer length in 0.1 wt% SDS solutions.

Other factors modify surface tension and affect the “state” diagram. In contrast to

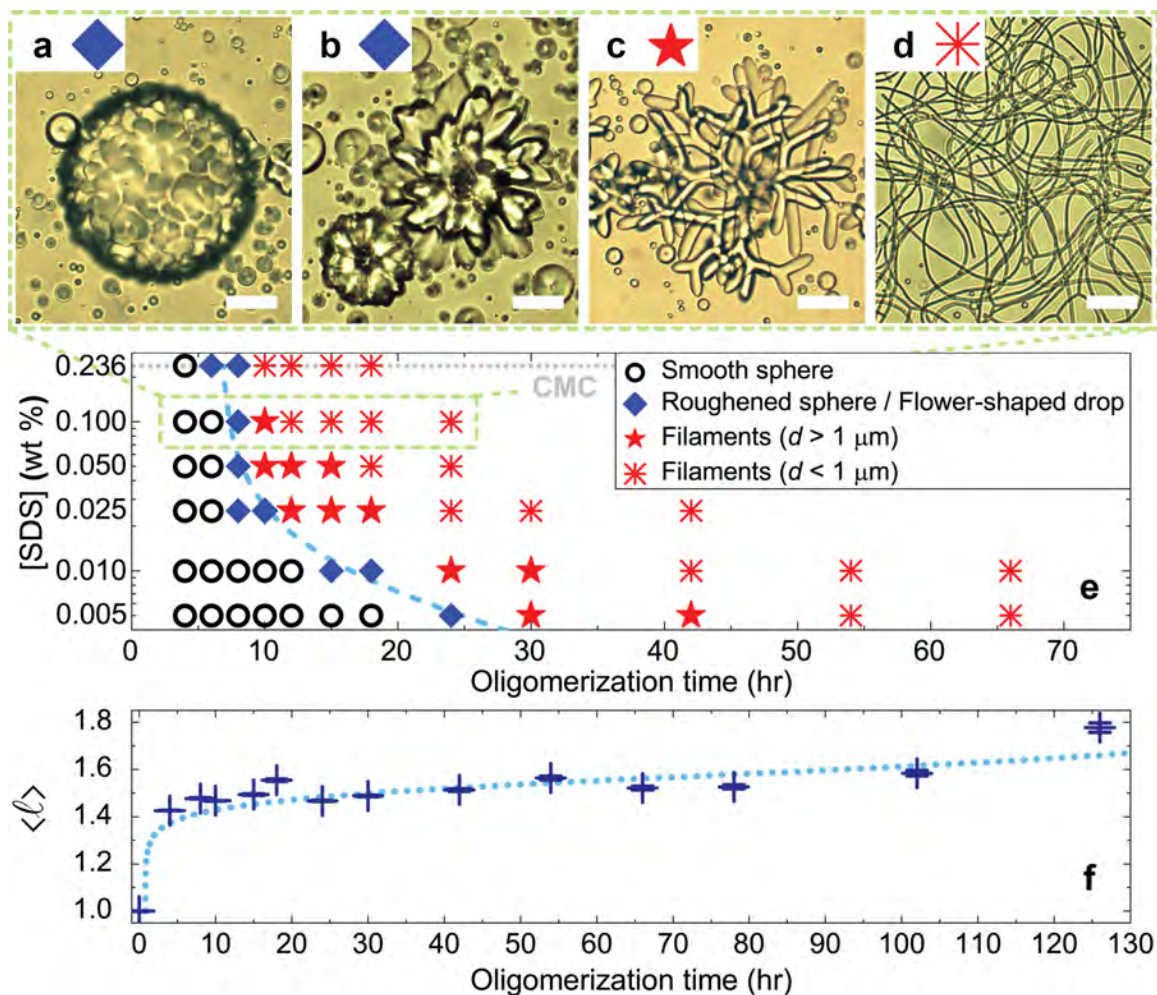


Figure 31: **Equilibrium nematic liquid crystal oligomer drop morphologies as function of mean oligomer chain length and surfactant concentration.** **a-d**, Optical images of common NLCO drop morphologies at room temperature in a 0.1 wt% SDS solution. With increasing  $\langle \ell \rangle$ , the morphologies shown are (a) a roughened sphere, (b) flower-shaped drops, and (c-d) filamentous structures with decreasing diameter. **e**, The state diagram, constructed from the data, exhibits the equilibrium morphology (examples in (a-d)) versus  $\langle \ell \rangle$  and surfactant concentration. Increasing either parameter better facilitates filament formation. The dashed curve roughly separates spherical and non-spherical drop regimes. **f**, Size exclusion chromatography shows that  $\langle \ell \rangle$  (in units of monomer length) increases with oligomerization processing time (horizontal axis of plots in (e), (f)). Bars indicate the spread in  $\langle \ell \rangle$ , which mainly arises from our inability to detect the longer-chain components. Dotted curve is to guide the eye. Scale bar in (a-d),  $20 \mu\text{m}$ .

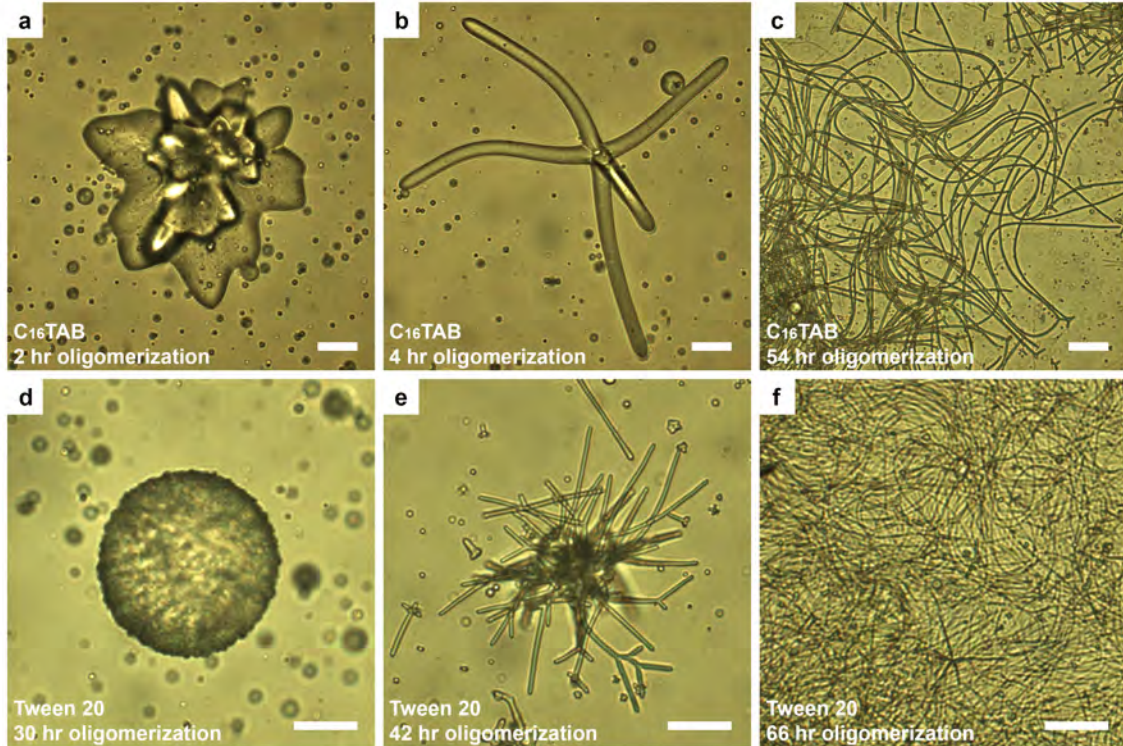


Figure 32: **Nematic liquid crystal oligomer structures in aqueous solutions of different surfactants as a function of the mean oligomer chain length,  $\langle \ell \rangle$ .** NLCO drops in aqueous solutions with different surfactants, *i.e.*, with either cationic (hexadecyltrimethylammonium bromide, C<sub>16</sub>TAB) or nonionic (Polysorbate 20, Tween 20) surfactants. These systems exhibit a drop morphology evolution similar to that from SDS, *i.e.*, with respect to cooling and an increase of  $\langle \ell \rangle$ . After cooling from 90 °C to 20 °C, a representative NLCO drop in a 0.5 mM C<sub>16</sub>TAB aqueous solution (below CMC, **a-c**) and a representative NLCO drop in a 0.03 mM Tween 20 aqueous solution (below CMC, **d-f**). Both evolve with increasing  $\langle \ell \rangle$  (consult **Fig. 31f** for relation between the oligomerization time and  $\langle \ell \rangle$ ). In all cases, it is important that NLCOs should favor homeotropic anchoring at the drop interface. Images are taken at the room temperature. Scale bars: 20  $\mu\text{m}$ .

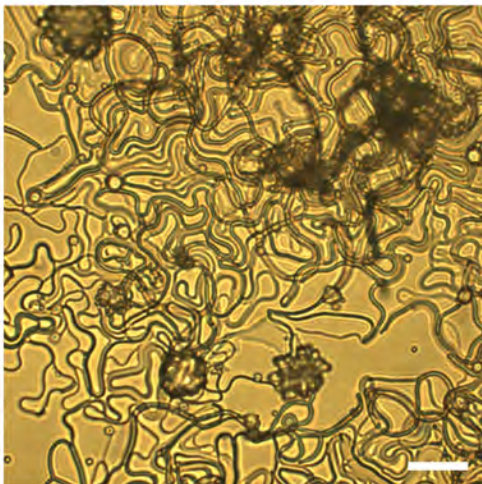


Figure 33: **Aggregated nematic liquid crystal oligomer filamentous structures for SDS concentrations above critical micelle concentration.** In a 1 wt% SDS aqueous solution, the NLCO drops exhibit similar but more complicated shape transition behaviors than those below CMC (critical micelle concentration), *i.e.*, after cooling from 90 °C to 20 °C. For example, *aggregated* filamentous structures form and sometimes stick to the substrate due, in part, to micelle-induced depletion. (For comparison, expanded filamentous structures form in aqueous solutions below CMC, see example in **Fig. 28f** and **Fig. 31c-d**.) The scale bar is 20  $\mu\text{m}$ .

work on *non-equilibrium* LC filament formation [130, 131, 132], our experiments were largely carried out below the critical micelle concentration (CMC) of SDS wherein increasing SDS concentration will lower  $\gamma$  and help facilitate interfacial roughening and filament formation (see Fig. 31e). Additional experiments confirmed the primary phenomena are not unique to SDS surfactant (Fig. 32), nor limited to surfactant concentrations below CMC (Fig. 33).

## 4.5 Director Configurations within Spherical and Filamentous Structures

Given this emerging qualitative picture, we sought to understand the shape tran-

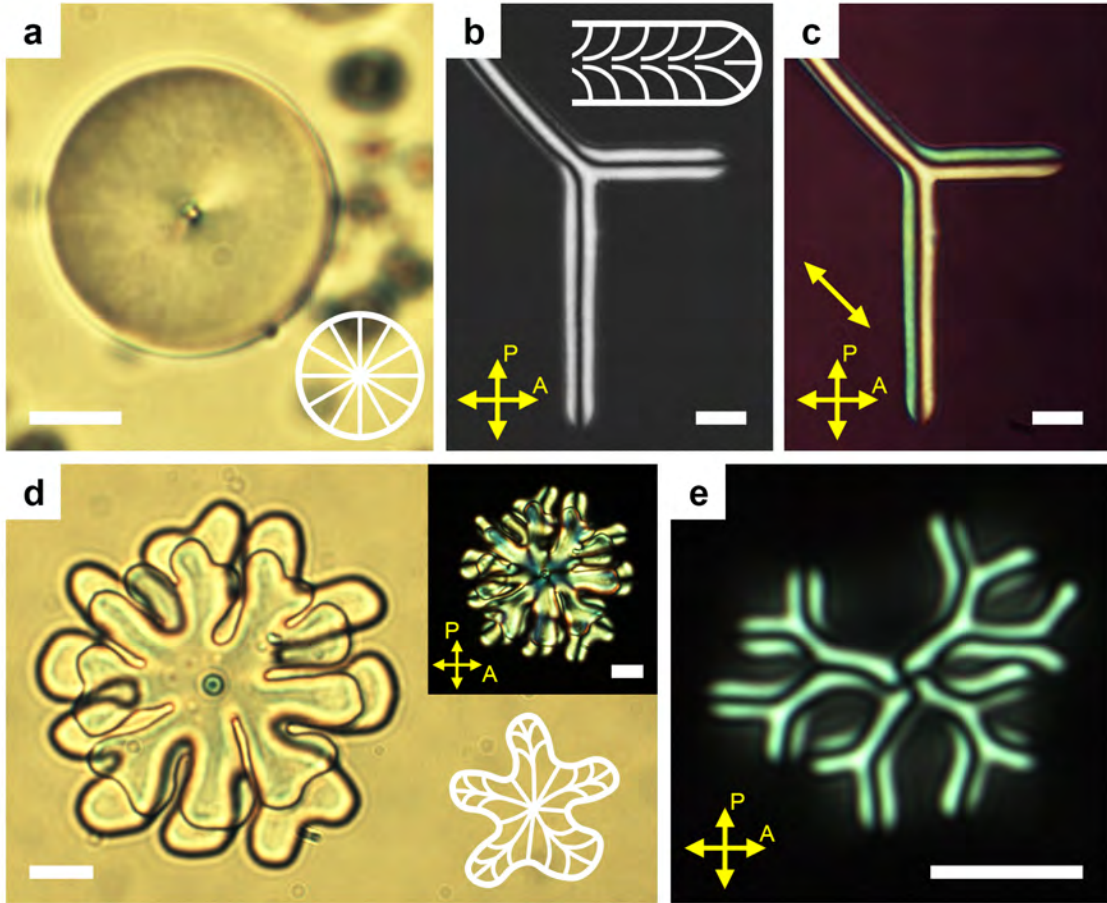


Figure 34: **Director configurations within nematic liquid crystal oligomer structures.** **a**, Bright-field image of spherical NLCO drop with a single, central radial hedgehog defect. **b-c**, POM coupled with a full-wave retardation plate enables identification of nematic director configurations within a section of a y-branched NLCO filamentous structure. Yellow indicates northwest–southeast alignment; cyan indicates northeast–southwest alignment. Inset: 2D projected director field schematic. **d-e**, The hedgehog always remains at the center of drop, even for complex structures, *e.g.*, after evolving to a flower-shape (bright-field (**d**); POM image and director field schematic (inset)) or a filamentous structure (hedgehog appears as the cross-pattern in POM (**e**)). Note, structures in (**d-e**) were weakly confined in a quasi-2D chamber so the filaments tended to grow perpendicular to optical axis, providing easy observation of the point defect. Scale bar is 10  $\mu\text{m}$ .

sitions more quantitatively. To this end, we determined NLCO director configurations using polarization optical microscopy (POM) with a full-wave retardation plate. We then applied simple models (please consult next section) to determine free energies for each case.

Here we focus on the two limiting morphologies: spherical versus filamentous drops. Spheres exhibit the classic POM texture corresponding to a radial hedgehog director configuration with topological charge +1 (point defect) at its center (Fig. 34a). Filaments exhibit an *escaped-radial* director configuration (Fig. 34b-c). For all geometries, the single point defect always remains at the drop center (see Fig. 34a, d, e).

## 4.6 Heterogeneity and Chain-length-dependent Oligomer Segregation Drive Drop Shape Transitions

To predict shape transition phenomena, modeling must account for energetics associated with both interfacial tension and elastic bulk free energy of the confined NLCO. The calculations thus require knowledge about the splay ( $K_{11}$ ), twist ( $K_{22}$ ), bend ( $K_{33}$ ), and saddle-splay ( $K_{24}$ ) NLCO elastic constants, as well as interface anchoring strength. We utilize well known models for the sphere with radial hedgehog director configuration [145] and for cylinders with escaped-radial director configuration [146, 147, 148, 149, 150]. Importantly, all models assume a homogeneous, *monodisperse chain length distribution* for the NLCOs. The models employ  $\gamma$  from pendant drop experiments, measured drop dimensions, and estimates of elastic constants and interfacial anchoring strength based on small molecule LCs [151]. Calculations then yield conditions for the sphere-filament free energy instability.

Surprisingly, we found that free energy instabilities only occur (according to the model) if our system has either an unphysically large saddle-splay elastic constant ( $K_{24} > 30 \times K_{11}$ ), or a value of  $\gamma$  that is much smaller ( $\sim 10x$ ) than those obtained in the pendant drop experiments. Given this discrepancy, we were compelled to consider other effects. In the process we uncovered the importance of NLCO *chain length polydispersity* (*molecular heterogeneity*), which can profoundly impact interface and core energetics.

In the rest part of this section, we provide details of our model free energy calculations. Note, we employ equilibrium models because the observed effects were reversible with slow temperature cycling, and the structures were stable. For rapid quenching (non-equilibrium) though, it is still possible to generate a transient negative surface tension which could also drive the effect.

#### 4.6.1 System Free Energy for Nematic Liquid Crystal Oligomer Drops & Filaments

The Frank free energy for a nematic liquid crystal is given below; it accounts for the elastic energy associated with spatial distortions of the director  $\hat{\mathbf{n}}$  in the liquid crystal [152], that is:

$$F_v = \frac{1}{2} \int d^3r \{ K_{11}(\hat{\mathbf{n}} \nabla \cdot \hat{\mathbf{n}})^2 + K_{22}(\hat{\mathbf{n}} \cdot \nabla \times \hat{\mathbf{n}})^2 + K_{33}[\hat{\mathbf{n}} \times (\nabla \times \hat{\mathbf{n}})]^2 - K_{24} \nabla \cdot [\hat{\mathbf{n}} \times (\nabla \times \hat{\mathbf{n}}) + \hat{\mathbf{n}}(\nabla \cdot \hat{\mathbf{n}})] \} . \quad (4.1)$$

Here  $K_{11}$ ,  $K_{22}$  and  $K_{33}$  are elastic constants for splay, twist and bend deformations, respectively. The final term, with the elastic constant  $K_{24}$ , is called the saddle-splay; it is absent from the corresponding Euler–Lagrange equation but contributes to the total free energy. Note, for simple solutions, the so-called splay-bend  $K_{13}$  elastic

deformation and other second derivatives (or higher-order terms) of the director field [153, 154] are usually not included — for example, inclusion of  $K_{13}$  without higher order terms can lead to paradoxes [155, 156] — nevertheless, interested readers can find free energy models which include  $K_{13}$  and discuss these issues [149]. To simplify calculations even further, a one-constant limit of the Frank free energy [145] is often applied, that is,  $K_{11}$ ,  $K_{22}$  and  $K_{33}$  are set equal and expressed as a single value,  $K$ .

In addition to liquid crystal elastic free energy, our modeling includes interfacial free energy,

$$F_{\sigma-iso} = \gamma \int dS \quad , \quad (4.2)$$

and liquid crystal interface anchoring energy [157],

$$F_{\sigma-aniso} = \frac{1}{2} W_a \int dS \sin^2 \Phi \quad , \quad (4.3)$$

where  $\gamma$  is the interfacial tension,  $W_a$  is the anchoring energy coefficient at the interface, and  $\Phi$  is the angle between the liquid crystal director at the interface and the interface normal. Both terms are integrated over the surface.

Starting with these elastic energy expressions, and using well-established elastic models for a sphere (with radial director configuration) [145] and for a cylindrical filament (with escaped-radial director configuration) [146, 147, 148, 149, 150], one can derive expressions for total system free energy.

For the sphere (one-constant approximation):

$$F_s = 8\pi \left( K - \frac{1}{2} K_{24} \right) R + \gamma 4\pi R^2 \quad , \quad (4.4)$$

or, if  $K_{11} \neq K_{33}$ ,

$$F_s = 8\pi \left( K_{11} - \frac{1}{2}K_{24} \right) R + \gamma 4\pi R^2 . \quad (4.5)$$

For the filament (one-constant approximation),

$$F_f = \pi K \left( 3 - \frac{K_{24}}{K} - \frac{1}{\sigma} \right) L + \gamma 2\pi r L , \quad (4.6)$$

where  $\sigma \equiv \frac{W_a r}{K} + \frac{K_{24}}{K} - 1 > 1$  .

Or, if  $K_{11} < K_{33}$ ,

$$F_f = \pi K_{11} \left[ 2 + \frac{k}{\sqrt{k-1}} \tan^{-1} \sqrt{k-1} - \frac{k}{\sqrt{k-1}} \tan^{-1} \left( \frac{\sqrt{k-1}}{\sigma} \right) - \frac{K_{24}}{K_{11}} \right] L$$

+  $\gamma 2\pi r L$  , (4.7)

where  $k \equiv \frac{K_{33}}{K_{11}}$  and  $\sigma \equiv \frac{W_a r}{K_{11}} + \frac{K_{24}}{K_{11}} - 1 > 1$  .

Or, if  $K_{11} > K_{33}$ ,

$$F_f = \pi K_{11} \left[ 2 + \frac{k}{\sqrt{1-k}} \tanh^{-1} \sqrt{1-k} - \frac{k}{\sqrt{1-k}} \tanh^{-1} \left( \frac{\sqrt{1-k}}{\sigma} \right) - \frac{K_{24}}{K_{11}} \right] L$$

+  $\gamma 2\pi r L$  . (4.8)

Here  $K$  is the composite elastic constant (that is, in the one-constant approximation) of the NLCO mixture.  $R$  is the radius of the spherical NLCO drop, and  $r$  and  $L$  are the radius and length of the NLCO cylindrical filament, respectively. The twist elasticity,  $K_{22}$ , makes no contribution to the free energy of either the sphere or the cylinder, and the anchoring energy term (Eq. (4.3)) arises for cylinders with an escaped-radial director configuration, but not for spheres with radial director con-

figurations. Note that in Eq. (4.1), Eq. (4.4) and Eq. (4.6), the saddle-splay ( $K_{24}$ ) term is sometimes ignored, but for our system  $K_{24}$  is essential. Ignoring saddle-splay would require a negative interfacial tension ( $\gamma$ ) for the spontaneous shape transitions, which is inconsistent with our measurements of  $\gamma$  and with the reversible, equilibrium shape transition phenomenology observed.

### 4.6.2 Criteria for Drop Shape Transitions Predicted by The Homogeneous Model

Since we observed a spontaneous transition from spherical to filamentous drops during cooling, we anticipate that an energetically favorable spontaneous process must have  $F_f < F_s$ . We next examine the parameter values needed to favor this spontaneous process.

Among these parameters,  $\gamma$  was measured by the pendant drop technique using large (millimeter-size) drops. For example, the measured  $\gamma$  is 4.64 mN/m at 80 °C and 2.36 mN/m at 30 °C for the sample NLCO#2 which had 7 h of oligomerization time (see Fig. 30 and **Section 4.2.4**; consult Refs. [129, 136, 137, 138, 139] for details of this unusual temperature-dependent trend). In one (typical) sample,  $R$  and  $r$  were measured by bright-field optical microscopy to be 13.0  $\mu\text{m}$  and 0.65  $\mu\text{m}$ , respectively. Because it is difficult to directly measure the elastic constants and anchoring energy coefficients of our NLCOs, we estimate their values at room temperature:  $K \approx 10^{-10}$  N and  $W_a \approx 10^{-4}$  J/m<sup>2</sup>. These numbers are chosen based on the values, and on the relationships between parameters, in drops of monodisperse small molecule liquid crystals. When interfacial free energy is dominant (for example, at high temperature or with short  $\langle \ell \rangle$ ), we expect the NLCO droplets to remain spherical. Then, knowing the interfacial tension, we can compute an estimate for  $K$ . Similarly, since the

droplet adopts a radial configuration with a hedgehog defect at its center [151],  $W_a$  is estimated by assuming that the extrapolation length,  $\xi_S \equiv K/W_a \approx 1 \mu\text{m}$ , for the spherical drop is much smaller than the drop diameter. Note that  $W_a$  typically ranges from  $10^{-6}$  to  $10^{-3} \text{ J/m}^2$  for weak to strong anchoring. (For reader reference, we list experimental values for important parameters. For thermotropic LCs: (1) 5CB has  $K_{11} \approx 6.2 \times 10^{-12} \text{ N}$  and  $K_{33} \approx 8.25 \times 10^{-12} \text{ N}$  ( $\sim 25 \text{ }^\circ\text{C}$ ); (2) 8CB has  $K_{11} \approx 6.0 \times 10^{-12} \text{ N}$  and  $K_{33} \approx 6.4 \times 10^{-12} \text{ N}$  ( $\sim 35 \text{ }^\circ\text{C}$ ) [158]. For lyotropic LCs: (1) DSCG has  $K_{11} \approx 10.2 \times 10^{-12} \text{ N}$  and  $K_{33} \approx 24.9 \times 10^{-12} \text{ N}$  (16 wt%, within  $\sim 4 \text{ }^\circ\text{C}$  of  $T_{NI}$ ); (2) SSY has  $K_{11} \approx 4.3 \times 10^{-12} \text{ N}$  and  $K_{33} \approx 6.1 \times 10^{-12} \text{ N}$  (29 wt%, within  $\sim 2 \text{ }^\circ\text{C}$  of  $T_{NI}$ ) [159]. For LC monomers that are molecularly similar to RM82:  $K \approx 2.6 \times 10^{-12} \text{ N}$  ( $\sim 97 \text{ }^\circ\text{C}$ ) [160]. For anchoring energy: (1) 5CB/SiO interfaces have  $W_a \approx 4.0 \times 10^{-5} \text{ J/m}^2$  ( $\sim 35 \text{ }^\circ\text{C}$ ) [161]; LC mixture (Merck-BDH, MLC 6608)/lecithin interfaces have  $W_a \approx 4.6 \times 10^{-4} \text{ J/m}^2$  ( $\sim 23.1 \text{ }^\circ\text{C}$ ) [162]; 8OCB/DMOAP-treated-glass interfaces have  $W_a \approx 1.0 \times 10^{-4} \text{ J/m}^2$  ( $\sim 75 \text{ }^\circ\text{C}$ ) [163].)

The models and criteria above, along with the experimental and estimated parameters, lead to well-defined constraints. A spontaneous shape transition is only possible, for example, when  $K_{24} \gtrsim 32 \times K_{11}$ , which is far too large for most liquid crystal materials. Note that abandoning the one-constant approximation does not affect this conclusion. In addition, varying  $K$  and  $W_a$  over a reasonable range — for example, from  $5 \times 10^{-11}$  to  $10^{-10} \text{ N}$  and  $5 \times 10^{-5}$  to  $5 \times 10^{-4} \text{ J/m}^2$ , respectively — does not affect the conclusion (see details in Fig. 35).

Revisiting the initial comparison between Eq. (4.4) and Eq. (4.6) suggests that a smaller “true”  $\gamma$  is needed to significantly increase the probability of a shape transition. We next consider how this situation can be realized through oligomer polydispersity and spatial segregation.

$\gamma_{\text{measured; mm-drop}}$ (mN/m)	$K$ (N)	$W_a$ (J/m <sup>2</sup> )	Required $K_{24}$ for shape transition	Reduction factor of $\gamma_{\text{measured; mm-drop}}$ gives $\gamma_{\text{true; micro-emulsion}}$	Required $K_{24}$ for shape transition with reduced $\gamma$
2.36	$5 \times 10^{-11}$	$10^{-5} \sim 10^{-4}$	$60.2 \times K_{11}$	20x	$5.7 \times K_{11}$
2.36	$10^{-10}$	$10^{-5} \sim 10^{-4}$	$31.6 \times K_{11}$	10x	$5.7 \times K_{11}$
2.36	$5 \times 10^{-10}$	$10^{-4}$	$8.6 \times K_{11}$	2x	$5.7 \times K_{11}$

Figure 35: **Range of required interfacial tension reduction needed for spontaneous shape transitions of NLCO drops with “physical” saddle-splay modulus.** This table summarizes parameter values that permit shape transitions (with reasonable saddle-splay elastic constants) based on our model free energy calculations. We fix the interfacial tension ( $\gamma_{\text{measured; mm-drop}}$ ) at 30°C measured by the pendant drop technique. A fairly wide range of estimated elastic constants ( $K$ ) and anchoring energy coefficients ( $W_a$ ) are employed in the calculations too. Per criteria for a spontaneous shape transition, we demand that the required saddle-splay elastic constant ( $K_{24}$ ) be of order  $\sim 6$  times the splay modulus (or less). The calculations show that a smaller “true” interfacial tension,  $\gamma_{\text{true; micro-emulsion}}$  (expressed as reduction factor of  $\gamma_{\text{measured; mm-drop}}$  in the Table), will significantly relax the saddle-splay requirement. This reduction of  $\gamma$  can be realized through oligomer polydispersity and resultant oligomer spatial segregation in the elastic stress field. Note, a reasonable range for  $K$  is  $5 \times 10^{-11}$  N to  $10^{-10}$  N; a value of  $K = 10^{-11}$  N is too small since it is the same order of magnitude as small molecule LCs such as 5CB.

### 4.6.3 Criteria for Drop Shape Transitions Predicted by The Heterogeneous Model

In applying Eq. (4.4) and Eq. (4.6), the simple models treated the bulk NLCO as a homogeneous material with monodisperse chain length. However, the NLCO mixture is polydisperse; it is composed of oligomers with a broad distribution of chain lengths (as demonstrated in Fig. 27a). This new degree of freedom offers the possibility for spatial rearrangement of the oligomers within the drops, wherein the long-chain-length oligomers move preferentially to the interface and the short-chain-length oligomers move to be closer to the drop center (see Fig. 26). For micrometer-size NLCO emulsion drops, molecules can easily diffuse and segregate within the confining structure on experimental timescales.

On the basis of simple energy considerations, spontaneous segregation to produce

a long-chain-rich shell (near the surface or interface) and a short-chain-rich core (for example, near the sphere center, or central axis of a filament or cylinder) will lower the system free energy. Consider a quantitative example. For spherical drops of radius  $R$ , one can compute the elastic free energy density in the shell and core regions using the relation:  $F_{elastic} = 8\pi K_{11}R$ . If we define the core as the central region with a radius ranging from 0 to  $R/2$ , and the shell as the remainder of the sphere, then the splay elastic energy density in the core is  $\sim 7$ x greater than that in the shell. In our experiments, the bulk elastic energy is lowered because short-chain NLCOs, which have smaller elastic constants, preferentially occupy the core regions which have very substantial director distortions (that is, large splay or splay/bend elastic distortions). This phenomenon can be understood as a chain-length-dependent “driving force” due to the elastic energy density gradient within the drop. This energy gradient between core and shell regions leads to spatial rearrangement of oligomers with different chain lengths.

Moreover, the segregation of long-chain oligomers to the drop surface will reduce the interfacial energy of the drop (compared to a drop containing a homogeneous mixture, as is the case for the millimeter-size drops). We thus expect  $\gamma_{true; micro-emulsion}$  to be less than the corresponding millimeter-size droplet interfacial tension,  $\gamma_{measured; mm-drop}$ , measured in the pendant drop experiments:

$\gamma_{true; micro-emulsion} < \gamma_{measured; mm-drop}$ . NLCO polydispersity, and its consequences for chain-length-dependent spatial segregation of oligomers within the drop, generates a critical new feature in the micro-emulsion that influences shape transitions and self-assembly. The resultant reduction of interfacial tension reduces the unphysically large  $K_{24}$  requirement (calculated in the previous section) and thus resolves concerns raised by the simple shape instability model calculations for homogeneous, monodisperse liquid crystals.

For example, using the same parameters for  $K$  and  $Wa$ , but with a reduction of  $\gamma$  by 10x, we obtain the requirement  $K_{24} \gtrsim 5.5 \times K_{11}$ , which is in an acceptable range for saddle-splay modulus. Of course, further reduction of  $\gamma$  (as long as interfacial energy still dominates at high temperature) decreases the required  $K_{24}$  value even more and renders shape transitions to be even more likely. (Note also that the segregation-induced decrease in bulk elastic energy will further reduce the requirements for  $\gamma$  reduction, because the decrease in elastic free energy in filaments is greater than in spherical drops.)

Before giving an estimation about how could the oligomer segregation lead to reduction of  $\gamma$ , I would like to introduce a simple bidisperse demixing model. The model provides an easy way to better understand the system; it also serves as a supplementary experiment for our main result.

#### 4.6.4 Macromer–monomer Mixing Experiments

These experiments were designed to confirm the influence of oligomer polydispersity on the shape transition phenomenology of NLCO drops. Specifically, we investigated how the average chain length of the oligomers in the NLCO mixture affects the shape transitions. For this study, however, we employed a synthetic approach to make the NLCO drop mixtures that was different from the methods mentioned elsewhere in this chapter (*i.e.*, the protocol mentioned in **Section 4.2.1**).

We first synthesized a main-chain liquid crystal macromer with a number-average molecular weight of approximately 6,900 Da; following the work by Ware et al. [133], this macromer had a mean chain length,  $\langle \ell \rangle$ , of  $\sim 9$ , that is, a mean chain length roughly 9 times the monomer length. This sample had a polydispersity index (PDI) of 1.3 (see Fig. 27). Note, PDI is defined as the ratio between weight-average molecular

weight ( $\overline{M}_w$ ) and number-average molecular weight ( $\overline{M}_n$ ). PDI = 1 implies uniform polymer chain length.

The macromers thus obtained were then mixed with pure RM82 monomer at different weight ratios in chloroform (chloroform : liquid crystal mixture = 3:1 wt/wt). The mixture was then emulsified in 0.1 wt% SDS aqueous solution, and then the chloroform was evaporated in a 90 °C water bath. No further chain growth occurred during this process (confirmed by  $^1\text{H-NMR}$ ) because the chain-extender, n-butylamine, was not added to the mixture. When all chloroform was removed, temperature cycling was carried out following the same protocol described in **Step 3** of **Section 4.2.1**. The resulting drop shapes and micro-structures were observed in bright-field and polarization optical microscopy (POM).

Upon cooling, the macromer–monomer NLCO drops transitioned from smooth spheres to roughened spheres, flower-like structures, and filamentous structures (see Fig. 36). These effects were dependent on the monomer : macromer weight ratio. Specifically, with increased mean oligomer chain length,  $\langle \ell \rangle$ , droplet structures with larger surface area are preferred (for example, longer, thinner filaments). The observed phenomenology agrees very well with observations in our main experiment. We have argued that the increased bulk elasticity and decreased interfacial tension accompanying increased  $\langle \ell \rangle$  promotes shape transitions. Quantitatively, as shown in Fig. 36b, the droplet’s tendency towards non-sphericity commences when  $\langle \ell \rangle \approx 1.4$ . This supplementary macromer–monomer mixing experiment thus exhibits the same tendency as the experiments that employed the synthesis-in-emulsion scheme. In the latter case, the droplet’s tendency towards non-sphericity commenced when  $\langle \ell \rangle \approx 1.5$ . Note, the  $\langle \ell \rangle$  at which non-sphericity commences can vary slightly with drop size.

We also carried out experiments with monomers only. Pure RM82 monomer ( $\langle \ell \rangle = 1$ ) crystallizes during cooling; it is nematic only above 86 °C. Thus, shape transi-

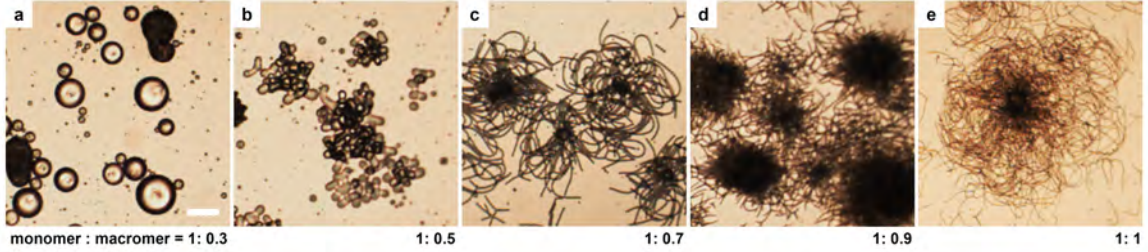


Figure 36: **Drop morphologies obtained from mixtures of macromers ( $\langle \ell \rangle \approx 9$ ) and monomers (RM82) at different weight ratios in a 0.1 wt% SDS aqueous solution after cooling.** With a fixed amount of RM82, increasing the concentration of macromers in the drop leads to longer  $\langle \ell \rangle$ , larger bulk elasticity, and lower interfacial tension. The latter two factors favor interfacial roughening and filament formation. Images are taken at the room temperature after cooling. Scale bar: 50  $\mu\text{m}$ .

tions are not seen with drops containing only monomer. Furthermore, experiments with drops containing only macromers ( $\langle \ell \rangle \approx 9$ ) did not exhibit shape transitions. Evidently, the surface tension in drops with pure macromer is too large to permit shape transitions, presumably due to poor anchoring at the surface [164]. Moreover, the macromer-only system viscosity is much larger [165] than the drops with smaller average chain length, making texture formation/reformation kinetics very slow.

By contrast, the NLCO mixtures we studied maintain good packing at the drop interface, probably because of different formation processes. The NLCOs were synthesized within each SDS stabilized drop. Thus, we expect that homeotropic director “pre-alignment” could already exist at early stages of the oligomerization process in these drops, that is, when most of the oligomer chains are short and the surfactants can induce good anchoring. Thus, importantly, the monomers are approximately locked into their interfacial structure at the outset. Then as the chains grow longer throughout the drop, the longer oligomers spatially segregate to an already partially ordered surface at high coverage and can help increase order at the interface in a perturbative manner. This segregation and greater molecular packing/order reduces

interfacial tension and ultimately induces shape transitions when interfacial tension becomes sufficiently small. In principle, the shape transformation process could still happen for a monodisperse system with very small surface tension. Our polydisperse NLCO mixtures, however, provide an easy segregation-driven route to lowering interfacial tension and elastic energy.

#### 4.6.5 Polydispersity and Oligomer Segregation Reduce Interfacial Tension and Facilitate Drop Shape Transitions

As promised at the end of **Section 4.6.3**, we can estimate the reduction of  $\gamma$  induced by oligomer segregation using a simple bidisperse demixing model (alluded in **Section 4.6.4**).

In the model, one component of the mixture is a monomer ( $\langle \ell \rangle = 1$ ), and the other component is a macromer with  $\langle \ell \rangle \approx 9$ . As shown in Fig. 36c, for a monomer:macromer mixture weight ratio of 1:0.7, the overall mean chain length is  $\langle \ell \rangle_{whole} \approx 1.53$ . This condition gives rise to filamentous drop structures. Taking this condition to be exemplary for filament formation, we next show how the macromers and monomers segregate into core and shell regions with uneven chain length distributions in order to lower overall system elastic energy.

Because the total amount of monomer and macromer is conserved during segregation, we readily generate an equation relating the monomer:macromer weight ratio and  $\langle \ell \rangle_{whole}$  of the initial homogeneously distributed mixture to the final, segregated long-chain-rich shell with  $\langle \ell \rangle_{shell}$  and the short-chain-rich core with  $\langle \ell \rangle_{core}$ . The re-

sulting relation is

$$\begin{aligned} \frac{0.7}{1 + 0.7} = & \frac{V_{shell}}{V_{total}} \times \frac{6641 (\langle \ell \rangle_{shell} - 1)}{6641 (\langle \ell \rangle_{shell} - 1) + 673 (9 - \langle \ell \rangle_{shell})} \\ & + \frac{V_{core}}{V_{total}} \times \frac{6641n}{6641n + 673 (1 - n)} . \end{aligned} \quad (4.9)$$

Here  $n$  is the number fraction of macromer in the core region, and  $V_{shell}$  and  $V_{core}$  are volume of shell and core regions, respectively:  $V_{shell} + V_{core} = V_{total}$ . The mean chain length of the core can also be written in a simple form

$$\langle \ell \rangle_{core} = 1 \times (1 - n) + 9n . \quad (4.10)$$

For simplicity, we assume that segregation leads to equal volumes of core and shell, and we set  $\langle \ell \rangle_{shell} = 1.70$ . Eqs. (4.9) and (4.10) then give  $n \approx 4.9 \%$  and  $\langle \ell \rangle_{core} \approx 1.39$ . Note that it is straightforward to use this model with other assumptions about the volume segregation ratio and the mean oligomer chain length in the shell; the general qualitative conclusions about system free energy reduction (compared to the homogeneous drop) will be the same for sensible parameters.

To quantify how the chain length redistribution within the structure affects the system's overall bulk elastic energy, we take  $\langle \ell \rangle_{core} \approx 1.39$  and  $\langle \ell \rangle_{shell} = 1.70$ , and we compute the elastic free energy volume integrals over the target geometry (for example, radial/sphere and escaped-radial/filament) using the Frank free energy equation (Eqs. (4.1)). We then compare the Frank free energy of the segregated system to that of the homogeneously distributed system with  $\langle \ell \rangle_{whole} \approx 1.53$ . For this calculation, we assume that the elastic constant is proportional to oligomer mean chain length [141, 142]. The comparison reveals that this reduction in  $\langle \ell \rangle_{core}$  will decrease bulk elastic energy by  $\sim 5 \%$  for the sphere and  $> 8 \%$  for the filament (that is, compared

to the homogeneously distributed systems).

Most importantly, as a result of oligomer segregation (for example, an increase of local mean chain length near interface from 1.53 to 1.70, by  $\sim 0.17$ ), the interfacial tension is lowered dramatically. To better appreciate this assertion, consider the homogeneous mixtures NLCO #2 (7 h oligomerization) and NLCO #5 (24 h oligomerization) in Fig. 30. For these samples, the interfacial tension (for example, at 30 °C) of the drops made with NLCO #5 (0.12 mN/m) is significantly much smaller, by a factor of  $\sim 20x$ , compared to that of NLCO #2 (2.36 mN/m), whereas the average chain length changed by only  $\sim 0.10$ . Indeed, from the pendant drop experiments, one would expect that a long-chain-rich interface (with local increase of mean chain length of  $\sim 0.17$ ) would reduce  $\gamma$  substantially, that is,  $\gamma$  would be reduced by at least a factor of 20x. Hence, our earlier statement that “a reduction of  $\gamma$  by 10x to approximately 0.1 mN/m yields sphere–filament instabilities with reasonable saddle-splay moduli” is a conservative estimate of the expected change of interfacial tension.

Last, we reiterate that in the millimeter-size drops measured by the pendant technique, we expect the chain-length-dependent segregation to be insignificant. Macroscopically, the drop is approximately homogeneous because the millimeter-size drops have many nematic microdomains (each with a director oriented uniformly along a different direction) and many randomly situated disclination lines. The larger drops have lower curvatures too, and therefore director distortion is reduced near their surfaces. The largest distortions that could drive segregation should occur locally near disclinations and at domain walls distributed roughly uniformly throughout the drop; thus, they will not promote net migration to the surface. Moreover, the required molecular diffusion over long distances will be small because of extremely long diffusion times (domain walls would also act as barriers to oligomer diffusion, and

so on). Thus, interfacial tension derived from the pendant drop experiments is set by the macroscopic “average” of the whole droplet, that is,  $\langle \ell \rangle$  of the initial (source) NLCO distributions.

## 4.7 Analogue in Biological Matter: Polydispersity and Phase-separation Drive Surface Patterning

Generally, in the world around us, most materials are intrinsically heterogeneous (polydisperse). Natural polymers like rubber, wood cellulose, and silk are composed of long-chain molecules with different lengths. Natural and practical dispersions (*e.g.*, solid particles in liquids, liquid drops in liquids or in gasses) are also comprised of constituents with a wide distribution of sizes. Since it is widely observed, it will not be surprised if the molecular heterogeneity plays a key role in some important phenomena in biological objects. For example, molecular heterogeneity driven segregation and phase separation were reported to promote formation of the diverse surface patterns and morphologies in pollen grains, insect cuticles, fungal spores, and the photonic structures in butterfly wing scales as well as bird feathers [117, 118, 119, 120].

As discussed earlier in this chapter, we have found that the drop morphology changes were driven by the polydispersity of the molecules contained inside the drop as well as the chain-length-dependent oligomer segregations. Future studies of branching behaviors thus provide new insights into drop assembly and stabilization, and, possibly, could reveal connections to molecular heterogeneity driven segregation and phase separation for function in biological matter.

## 4.8 Summary and Future Directions

We have developed a technique that allows for equilibrium transitions among a rich set of non-spherical morphologies in drop suspensions consisting of NLCOs. At high temperature, the drops have spherical shape because of the domination of interfacial tension. Upon cooling, the drops evolve reversibly from spheres to roughened spheres, flowers, and branched filamentous network. Observations and modelling reveal that molecular heterogeneity plays a crucial role in this process; spatial segregation of oligomer chains of varying length tips the balance between free energies, driving the morphogenic phenomena. Specifically, induced by elastic energy gradients of the director within the drop, short-chain NLCOs, which have smaller associated elastic constants, will migrate towards the core, and long-chain NLCOs, which have larger associated elastic constants, will migrate towards the drop surface. As a result, interfacial tension of the drop is lowered dramatically due to stronger nematic ordering at the interface driven by the greater numbers of long-chain oligomers; meanwhile, the elastic energy also decreases slightly because of reduced average rod-length in the core. *Spatial redistribution of polydisperse oligomers* in the drops and the consequent reduction of interfacial tension thus yield sphere-filament instabilities with reasonable saddle-splay moduli.

Although rarely studied, some shape transitions have been observed in molecularly heterogeneous systems [166], and the phenomenon of segregation by size, broadly defined, has been reported in lipid membrane systems [167], near topological defects in LC simulations [168], and in much larger LC polymer systems mediated by size-dependent nematic/isotropic-transition temperatures [165]. It is perhaps useful to reconsider these phenomena in light of the new results revealed by our experiments.

To conclude, while polydispersity and molecular heterogeneity are often avoided

in synthetic systems, here they facilitate equilibrium transitions among dramatically different morphological structures. This ability can be exploited to create soft materials such as highly branched networks with uniform filament size, *i.e.*, simply by tuning chain length distribution, temperature, and surfactant concentration. Further studies of branching behaviors may provide new insights about drop assembly and stabilization.

Moreover, the self-assembly processes are reversible, and the network structures can be permanently locked by UV crosslinking. Simple rules revealed by the experiments offer new concepts for creation of programmed spatio-temporal networks. Currently, my work is directed toward the exploitation of these possibilities, which will be discussed in **Chapter 5**.

# Chapter 5

## Liquid Crystal Elastomers from Flower-like and Filamentous Drops

### 5.1 Introduction

In **Chapter 4**, we discovered and characterized a novel temperature-tunable soft system. These samples consisted of nematic drops containing liquid crystal oligomers and suspended in aqueous phase; the shapes of these drops could be reversibly switched from sphere-like to filamentous network-like (Fig. 28). The shape transition phenomenon provided new insights into drop assembly and stabilization, and it revealed new connections to the surface patterning processes of biological matter. In this chapter, we further explore the potential of this effect and this system as a platform to make new functional materials.

Thus far, the nematic morphologies (see Fig. 31a-d for examples) have been liquid-like. They are quite stable and can survive for days, but they still deform like a fluid. The precursor materials, however, have the potential to become solid-like. We thus modified the synthesis procedure to this end. Specifically, we added crosslinkers into the existing synthesis sequence to enable “solidification” of the structures (*i.e.*, by crosslinking the nematic liquid crystal oligomers (NLCOs) into solid nematic liquid crystal elastomers (NLCEs)). The augmented scheme thus provides a new solid material in a variety of shapes and with a broad range of operation potential. The resultant materials also offer an opportunity for us to carefully characterize the resultant liquid crystalline structures microscopically, *i.e.*, with resolution beyond that of the diffraction limit of optical microscopy.

Previously, we demonstrated that the drop morphology can be tuned by NLCO

chain length distribution, system temperature, and surfactant concentration in the background aqueous phase. In the first part of this chapter, our primary experiments show how to lock-in and study the resulting structures. Additionally, in preliminary experiments presented in the second part of this chapter, we show that a cholesteric nematic could be a promising candidate to make the self-assembled drop-constructions programmable. Specifically, the surface patterning on the cholesteric nematic drops is found to be coupled to subsurface disclination loops, which arise from the interplay between surface homeotropic anchoring and bulk chiral twist. This new degree of freedom could enable bottom-up fabrication of functional materials.

Finally, we report on preliminary research that seeks to develop potential optical/photonic applications of NLCO/NLCE substrates embedded with laser dyes, nano-particles, and quantum dots. The novel morphologies of the nematic networks, as well as their temperature-tunable geometries, could serve as templates with which to organize functional materials in a controllable manner, and could potentially endow the system with unique functionalities.

## 5.2 Method and Materials

The synthesis setup in this chapter is similar to that in **Chapter 4**. In short, the experiments employ modified NLCO drops (or NLCO composite drops), tens of micrometers in diameter, dispersed in water containing 0.1 wt% sodium dodecyl sulfate (SDS) surfactant. Each surfactant-stabilized emulsion contains a mixture of 1,4-bis-[4-(6-acryloyloxyhexyloxy)benzoyloxy]-2-methylbenzene (RM82) monomers and RM82 oligomers with variable chain lengths. The detailed component ratio between oligomers with different chain lengths is controlled by oligomerization time.

As discussed in **Section 4.2.1**, the modified NLCO (or NLCO composite) emul-

sions were made in three steps. In this case, we make a few modifications compared to our original procedure: (1) preparation of emulsion drops (suspended in a SDS aqueous solution) containing monomer (RM82), chain-extender (n-butylamine), and *a dopant*; (2) oligomerization within individual drops to link LC monomers together into liquid crystal oligomers (LCOs); (3) creation of a final, modified, NLCO (or NLCO composite) drop suspensions in water.

The specific modifications are described below. Note, all chemicals were used as received, without further purification or modification.

### **5.2.1 Crosslinking the Nematic Liquid Crystal Oligomer Structures to Make Nematic Liquid Crystal Elastomer Structures**

To convert fluid-like NLCOs into solid NLCEs, 2 wt% (by RM82 concentration) 2,2-Dimethoxy-2-phenylacetophenone (radical photoinitiator, Sigma-Aldrich) was added into the initial RM82/butylamine/chloroform mixture. Then the same oligomerization-cooling method described in **Section 4.2.1** was performed to make the oligomer structures.

After the NLCO emulsions reached their final (or desired) equilibrium morphologies, the NLCOs were crosslinked into elastomers by UV radiation (365 nm) for a few minutes. We then evaporated the background solution, sputter-coated thin metallic films (palladium/gold or iridium) onto the structures, and observed the resulting NLCEs via SEM (dual-beam FEI Strata DB235 Focused Ion Beam / SEM) using a 5.00 kV electron beam.

## 5.2.2 Cholesteric Nematic Liquid Crystal Oligomer / Elastomer Structures

To make cholesteric nematic liquid crystal oligomer drops, chiral dopants were added into the initial RM82/butylamine/chloroform mixture. Then the same oligomerization and cooling method described in **Section 4.2.1** was performed.

Two different types of chiral dopant were employed: (R)-2-Octyl 4-[4-(Hexyloxy)benzoyloxy]benzoate (R811, Tokyo Chemical Industry TCI) and (S)-2-Octyl 4-[4-(Hexyloxy)benzoyloxy]benzoate (S811, Tokyo Chemical Industry TCI). The amount of chiral dopant within RM82/butylamine/chloroform mixture is between 1-10 wt% by RM82 concentration. Note also, radical photoinitiators could be added (as detailed in **Section 5.2.1**), if cholesteric nematic liquid crystal elastomer structures were the target products.

## 5.2.3 Laser Dye Doped Nematic Liquid Crystal Elastomer Filamentous Networks

In this set of experiments, the laser dye Rhodamine 6G (Sigma-Aldrich) was added into the initial RM82/butylamine/chloroform mixture with a 1-5 wt% by RM82 concentration. The radical photoinitiator was also added (see details in **Section 5.2.1**). Then the same oligomerization and cooling method described in **Section 4.2.1** was performed.

## 5.2.4 Quantum Dot Doped Nematic Liquid Crystal Elastomer Filamentous Networks

In this set of experiments, CdSe/CdS core/shell quantum dots (QDs) was added into the initial RM82/butylamine/chloroform mixture. The CdSe/CdS QDs were

initially suspended in toluene at 7 mg/mL and were transferred to chloroform before the experiment. The final concentration of CdSe/CdS QDs within sample was 0.5-2 wt% (by RM82 weight).

The same oligomerization and cooling process described in **Section 4.2.1** was then performed. Radical photoinitiator was also added (as detailed in **Section 5.2.1**) when we were targeting NLCE-QD composite structures.

### **5.2.5 Gold Nanorods Doped Nematic Liquid Crystal Oligomer & Elastomer Filamentous Networks**

In this set of experiments, gold nanorods (AuNRs) with variable aspect ratios were added into the initial RM82/butylamine/chloroform mixture. The AuNRs were synthesized following schemes described in Ref. [169] and were suspended in chloroform. The concentration of AuNRs within samples was 0.5-2 wt% by RM82 weight.

The same oligomerization and cooling process described in **Section 4.2.1** was then performed. Radical photoinitiator was also added (as detailed in **Section 5.2.1**) when we were targeting NLCE-AuNR composites.

A Varian Cary 5000 UV-VIS-NIR Spectrophotometer was then employed to measure the optical absorption spectra of the resultant sample suspensions.

## **5.3 Self-assembled Nematic Liquid Crystal Elastomer Constructions with Desired Morphology**

As a short reminder, in **Chapter 4** we demonstrated the shape transitions of NLCO drops upon cooling (and heating). As the system temperature decreases, the

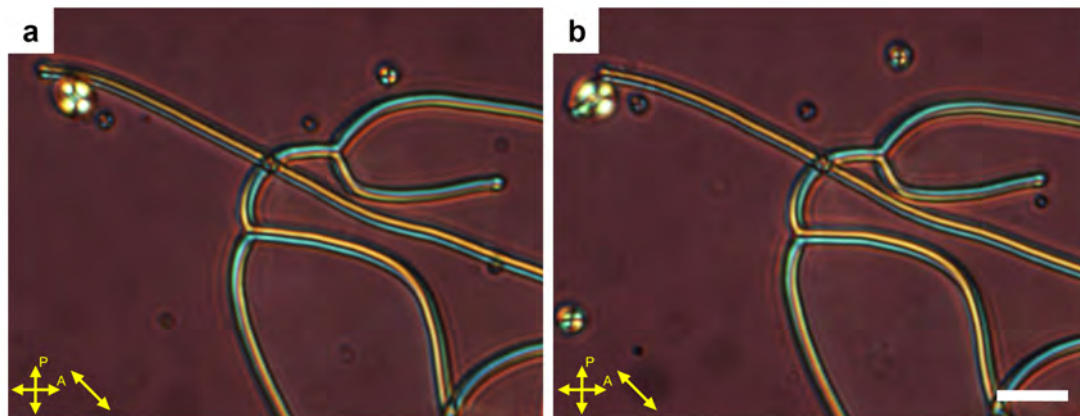


Figure 37: **Well-maintained morphology and director configuration during crosslinking of nematic liquid crystal oligomer structures into nematic liquid crystal elastomers.** POM (coupled with a full-wave retardation plate) images of **a**, NLCO filamentous structures and **b**, fully crosslinked NLCE structures in the same field-of-view. The two images were taken approximately 145 seconds (with continuous UV exposure for crosslinking) apart. A slight morphological difference between the NLCO and NLCE structures arises from thermal fluctuations of NLCO fibers before they are fully crosslinked. Scale bar: 10  $\mu\text{m}$ .

surface tension and bulk elasticity vary, and their interplay destabilizes the drop, thereby facilitating spontaneous polymorphic transitions to non-spherical structures (Fig. 28). Fig. 31a-d exhibit the rich and repeatable drop morphologies that could be achieved by fine-tuning oligomerization time (*i.e.*, mean oligomer chain length within drops), as well as SDS surfactant concentration in the background water solution. The resultant drop morphologies include smooth/roughened spheres, flowers, and large and small diameter filament networks.

To further harvest these self-assembled morphologies for functional materials, we UV-crosslinked the NLCOs into nematic liquid crystal elastomers (NLCEs). By comparing POM images of corresponding NLCE and NLCO structures, we confirmed that director configurations are well-maintained (see Fig. 37) during crosslinking.

Representative scanning electron microscopy (SEM) images of the NLCEs are shown in Fig. 38a-d. All these structures were achieved by cooling NLCO drops to

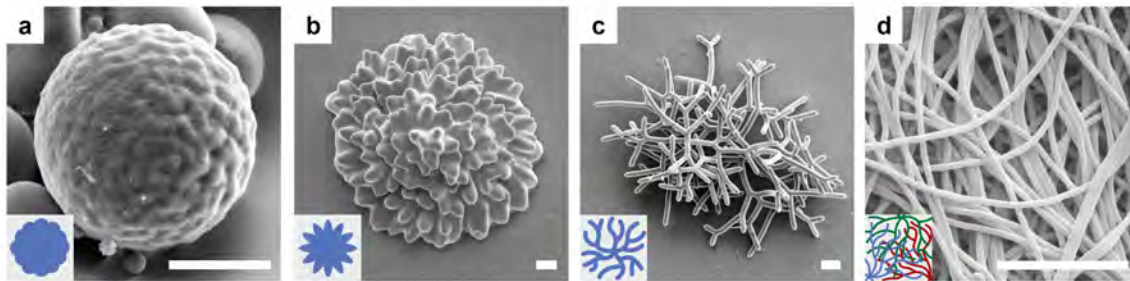


Figure 38: **Self-assembled nematic liquid crystal elastomer structures as a function of mean oligomer chain length within drops.** SEM images of the crosslinked NLCEs: **a**, roughened sphere, **b**, flower, and **c-d**, filamentous structures with decreasing diameter. See Fig. 31a-d for corresponding NLCO morphologies observed in bright-field optical microscopy. The objects shown in (**a-c**) were evolved from a single drop and are depicted in inset schematics. Thin filamentous structures grown from several drops are shown (intertwined) in (**d**). (Inset of (**d**): filaments with different colors grew from different drops.) Scale bars: 5  $\mu\text{m}$ .

room temperature and curing by UV illumination. With increasing mean oligomer chain length within the drops, the resultant morphology evolves from a sphere to roughened sphere, flower, and then to filaments with decreasing diameter.

We next demonstrate that these NLCE fibers can be densely packed into centimeter-wide and few-micron-thick, non-woven, free-standing NLCE mats (Fig. 39) by sedimentation. Such structures could find applications in responsive filtration and smart fabrics. Lastly, a NLCE yarn consisting of well-aligned fibers (Fig. 40) was made by directly pulling fibers out of the aqueous solution. These yarn-like objects could find use in artificial muscles [170, 171], or as tunable optical waveguides.

Compared to electrospinning [173], extrusion [170], and wet-spinning [171], this new approach for making fibrous structures is simple and scalable without need for sophisticated tools. Moreover, the nematic filamentous structures could serve as templates to organize nano-particles (NPs), nanorods (NRs), quantum dots (QDs), and quantum rods (QRs). The achieved composite constructions, together with their

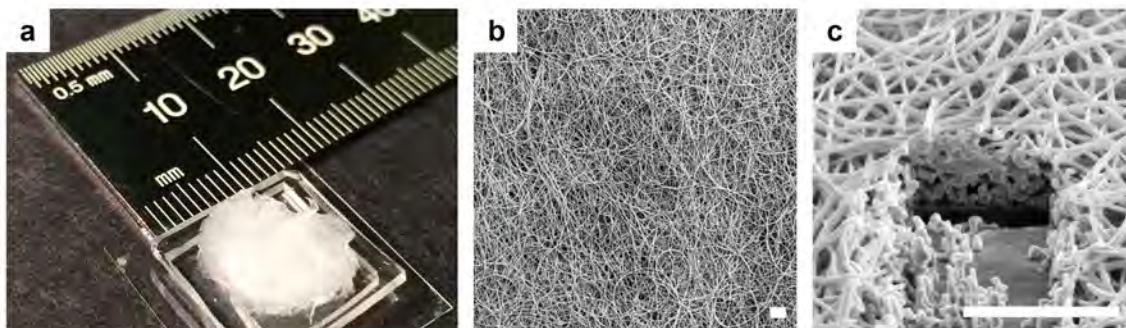


Figure 39: **Self-assembled nematic liquid crystal elastomer fibrous mat.** NLCE fibers can be densely packed into centimeter-wide and few-micron-thick, non-woven, free-standing mats by sedimentation. **a**, An image of the fibrous mat (mounted on a hollowed holder) with diameter greater than 1 cm is shown. **b-c**, Partial view of the free-standing NLCE fibrous mat and its cross section (cut by a gallium focused-ion-beam) viewed by SEM. Scale bar in **(b-c)**:  $5\ \mu\text{m}$ .

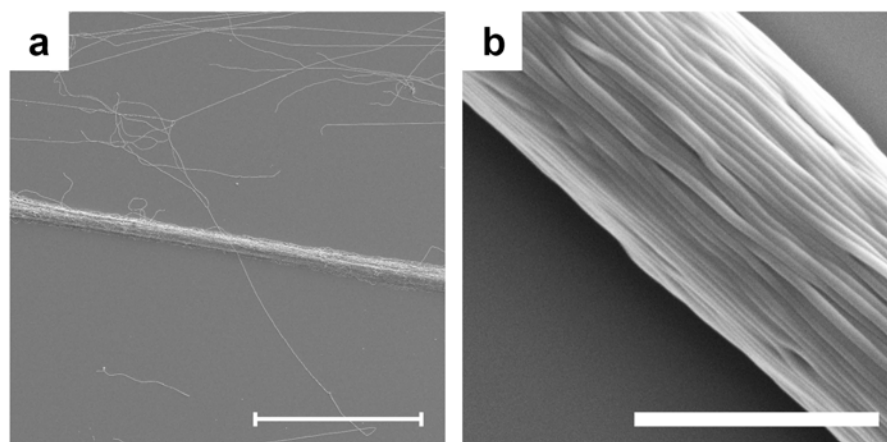


Figure 40: **Oriented nematic liquid crystal elastomer fiber yarn.** An oriented NLCE yarn consisting of well-aligned fibers was made by directly pulling fibers out of the aqueous solution. Scale bar in **(a)**:  $100\ \mu\text{m}$ . Scale bar in **(b)**:  $5\ \mu\text{m}$ .

temperature-tunable configuration and geometry, are expected to demonstrate novel photonic response. For example, the dye-doped filamentous networks are promising architectures for random lasers. I will briefly discuss these applications in the following sections.

Note, actuation effects with the current fibers are not as yet apparent in our preliminary studies. We believe this is because of the high crosslinking density in these samples due to insufficient oligomerization. Variation of LCO chemistry [172] could address this issue (*e.g.*, by decreasing crosslinking density or increasing oligomer chain “flexibility”), and work is underway along these lines.

## 5.4 Programmable Surface Patterning with Chiral Dopants

By combining the techniques discussed in **Chapter 4** and **Section 5.3**, we can generate micro-structures with desired morphologies, which can then be “solidified” for applications. Nevertheless, we still need more/better capabilities to “guide” construction. For example, in the current system, the surface roughening and budding arise at random positions on the NLCO drop surface; similarly, the fibers grow from random spots on the NLCO-water interface. In this section we describe research to introduce another degree of freedom for control.

Our work was inspired by non-trivial topological states that were reported to arise within cholesteric nematic droplets with homeotropic anchoring (*e.g.*, by adding chiral dopants into an achiral nematic mesophase). The observations showed linked disclination loops (*i.e.*, free-standing knots) locating just below the drop surface (together with layered structures in the bulk region of the drop) [174, 175, 176]. The discli-

nations near the surface were shown to be able to alter local director configurations and redistribute interfacial surfactant molecules as well as nano-particle assemblies [177, 178]. Building on this work, we added chiral dopants to convert the NLCOs to cholesteric NLCOs, and we investigated associated 3D textures in our system.

Following the scheme described in **Section 5.2.2**, we added the chiral dopant R811, or S811, at various concentrations into the oligomer mixture. We thus made cholesteric NLCO (CNLCO) drops. We then studied these drops, which were tens of micrometers in diameter and dispersed in a 0.1 wt% SDS water solution. All observations shown in this section were performed after cooling the drops slowly to room temperature.

First, we focus on the low-oligomerization stage, *i.e.*, the stage with drops containing short oligomer chains and exhibiting spherical shape after cooling. In this case, the topological defect textures in the cholesteric nematics are profoundly different from those in nematics. Instead of forming a single radial hedgehog at the NLCO drop center, typical CNLCO drops demonstrate sub-surface spiraling disclinations (see Fig. 41a-d; interested readers might also want to consult Ref. [174, 175, 176] for possible director configurations of these complicated topological structures, under various conditions). The detailed topological structures are determined by the ratio between droplet size and “pitch” size [175], which, in practice, can be controlled by the concentration of chiral dopant (see comparison between Fig. 41a & Fig. 41e). Note, these disclination loops with different links could be metastable; the transitions from one topological class to another are still not completely understood.

Surprisingly, these subsurface disclinations can be easily visualized by SEM after UV curing. Fig. 42 exhibits exemplary crosslinked cholesteric NLCE structures, with grooves winded around the smooth spherical surface. To the best of our knowledge, this is the first report wherein disclinations within nematic LC bulk physically affect

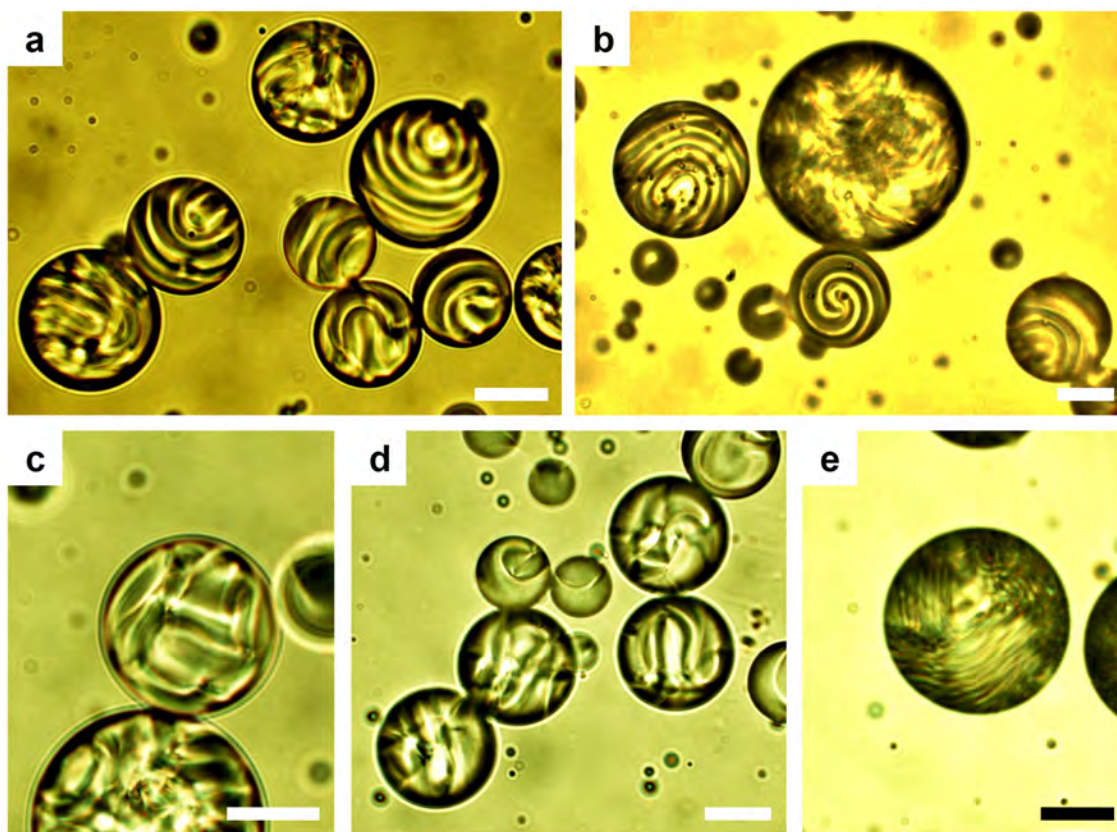


Figure 41: **Cholesteric nematic liquid crystal oligomer drops with spiralling subsurface disclinations.** Bright-field optical images of common cholesteric NLCO drops at room temperature after cooling in a 0.1 wt% SDS solution. Different chiral dopants and different doping concentrations are employed: **a-b**, 2 wt% R811. **c-d**, 2 wt% S811. **e**, 5.5 wt% R811. Note, all drops contain the same oligomer chain length distribution, *i.e.*, they have the same degree of oligomerization. Scale bar: 20  $\mu\text{m}$ .

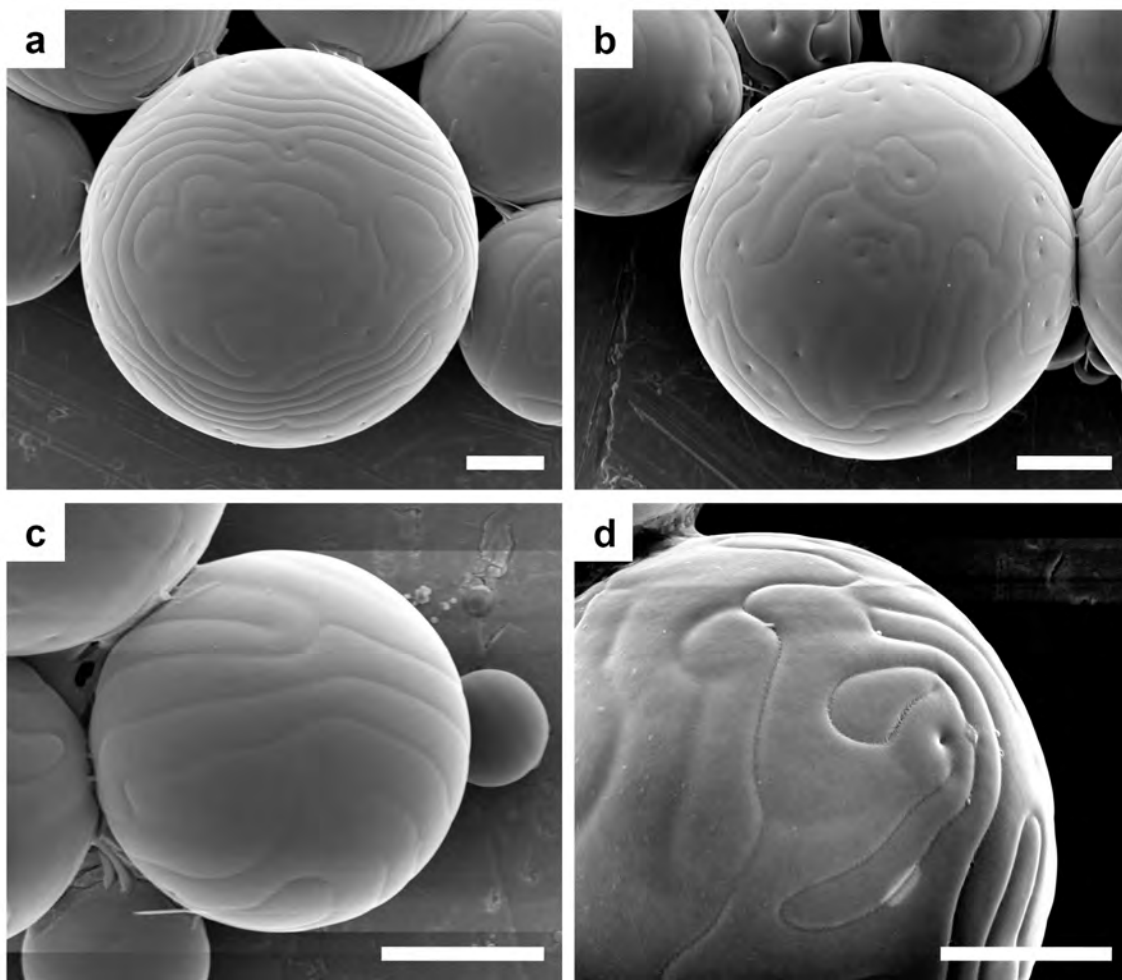


Figure 42: **Surface grooves associated with subsurface disclinations on cholesteric nematic liquid crystal elastomer spheres.** SEM images of the crosslinked cholesteric NLCE spheres showing grooves winding on their smooth surface. All samples are doped with 5.5 wt% R811. Scale bar: 10  $\mu\text{m}$ .

local topographic features at a liquid interface (although similar effects in smectic phase are known). We propose that the neighboring grooves represent a  $180^\circ$  turn of the helix; the dimples surrounded by grooves, on the other hand, represent double twist cylinder structures with axes pointing normal to the sphere surface. Potentially, the technique to generate surface grooves that coincide with the disclinations, which are readily crosslinked, could serve as a powerful tool for defect studies; SEM provides a much higher resolution, beyond diffraction limit of optical microscopy, and SEM imaging (of the 3D-spanning defect lines) from different observation angles is readily possible by simply rotating the solidified sample. The observations demonstrate potential connections, but more work is needed to clarify the relation between interfacial grooves and corresponding subsurface disclination loops. It is still unclear, for example, whether the grooves already exist on the CNLCO drop surface, or if they arise upon crosslinking; the latter is possible, potentially, because of buckling associated with anisotropic mechanical properties driven by local director deviations.

To trigger the spontaneous polymorphic transitions to non-spherical morphologies, we then increase oligomer mean chain length within the drops (consult **Section 4.3** & **Section 4.4** for the case without chiral dopant). Amazingly, in the cholesteric nematic case, the surface roughening and filament growing processes appear to be coupled to the local subsurface disclination loops. The drop exhibits surface roughening and spiraling stripe patterns which coincide with the spatial distribution of underlying disclination loops (see Fig. 43b-c).

Arguably, the major factor driving this “localized roughening” phenomena is the local interfacial anchoring change from homeotropic to planar, originating from the chiral nature of cholesteric nematics. Specifically, the LC molecules tend to twist against their neighbors in nematic LCs with chiral dopants. When the system has a cavity wall with a degenerate planar anchoring, the pitch axis can orient perpendicular

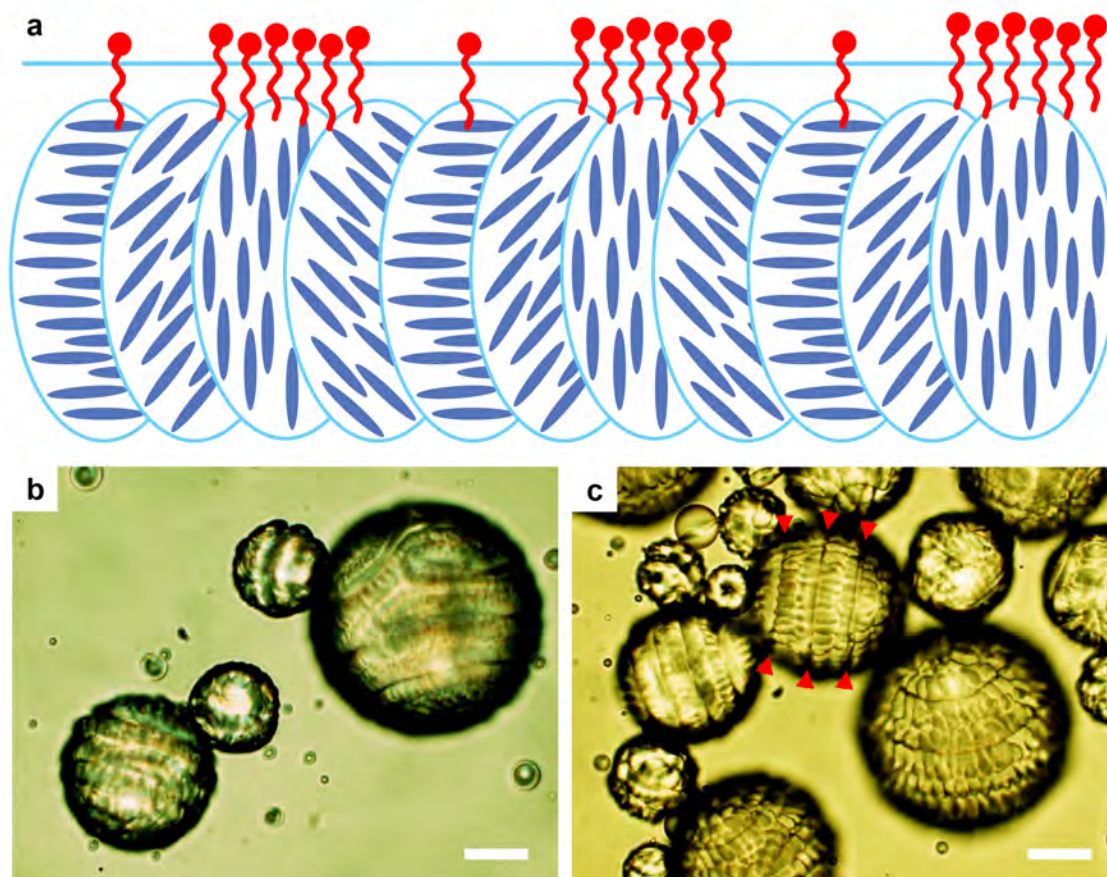


Figure 43: **Surface roughening coupled with spatial distribution of underlying disclination loops.** **a**, Schematic depicting a cholesteric nematic-water interface. The pitch axis orient parallel to the interface; blue ellipses represent LC molecules. (For simplicity, the oligomer chain length polydispersity is not illustrated.) The concept of uneven interfacial packing fraction of SDS molecules (red symbols) is illustrated. **b-c**, With increasing oligomer mean chain length within the drops, surface roughening increasingly emerges after cooling. The roughened patterns evolve from the regions between spiraling “stripes” on the drop surface (see example in **(c)**), as indicated by red arrows), which coincide with the underlying disclination loops. The samples are doped with 2 wt% R811. Scale bar: 20  $\mu\text{m}$ .

to the boundary to satisfy both the anchoring condition and the tendency of the cholesteric to twist. However, for a system with homeotropic anchoring, no direction exists wherein the pitch axis can orient to fulfill both interfacial anchoring and bulk twist. The homeotropic boundary therefore competes with cholesteric twist. As a result, the LC directors cannot be perpendicular to the entire boundary as sketched in Fig. 43a. The disclination loops thus form near regions wherein local directors deviate from preferred alignment.

The essential feature driven by local director deviations, *i.e.*, the emergence of subsurface disclinations, is the rearrangement of surfactant molecules absorbed at the drop interface. In particular, SDS molecules “prefer” to stay in the region with homeotropic anchoring (because of their molecular structure). The surfactant molecules redistribute, displaying lower packing fraction near disclination loops while having higher concentration in regions without disclinations. Consequently, the drop *sustains an uneven interfacial tension distribution, i.e.*, lower interfacial tension arises between observed spiraling stripes, wherein the surfactant molecules have higher packing fraction. The small interfacial tension, in turn, facilitates surface roughening and filament growing, as revealed in **Chapter 4**. Therefore, the surface roughening and budding now start from the region between neighboring disclinations/stripes, as shown in Fig. 43b-c.

Finally, a further increase in oligomer mean chain length within the drops eventually led to production of coiled filamentous structures after cooling (Fig. 44). Note, for the current procedure, only a few coiled fibers are observed within individual samples; most of the drops still evolve into straight filaments. Careful tuning of the pitch size, *i.e.*, concentration of chiral dopant, may be critical in order to consistently fabricate coiled structures. More work is needed to characterize the detailed mechanism associated with this unusual effect. With more understanding, the ability to

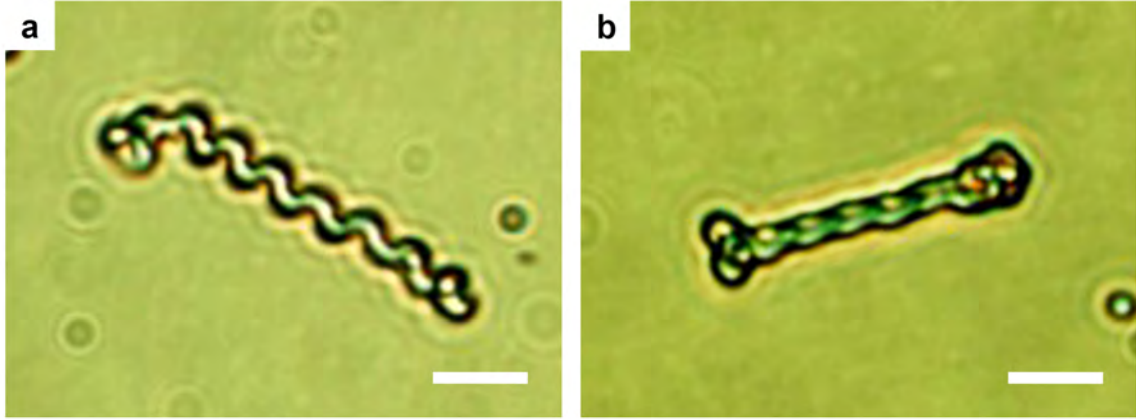


Figure 44: **Coiled filamentous structures formed by cholesteric nematics.** For cholesteric NLCO drops containing oligomers with a long enough mean chain length, coiled filamentous structures were sometimes found after cooling. The sample is doped with 5.5 wt% R811. Scale bar: 5  $\mu\text{m}$ .

spatially control detailed topological disclination textures could further enable the programmable surface patterning with richer functionalities.

## 5.5 Photonics in Nematic Filamentous Networks & Fibrous Nematic - Quantum Dot Composites

The inclusion of functional dopants, such as nanoparticles and fluorescent dyes, into polymer fibers is known to be a method to realize novel light sources. Lasing, for example, can occur. Recently, it has been demonstrated that lasing can arise from within the randomly distributed cavities of polymer fiber networks [179, 180]. The nanophotonic networks that support lasing consist of subwavelength waveguides (*i.e.*, individual fiber sections or links) connected at multiple nodes. However, all of the demonstrated systems were limited to 2D flattened fiber meshes, and the combination of high optical gain in small waveguide diameters has been proven to be challenging.

Our fibrous networks offer a new system in which to explore these types of effects.

As briefly discussed in **Section 5.3**, our scheme provides a simple and scalable approach for making fibrous structures, compared with the traditional electrospinning [173], extrusion [170], and wet-spinning [171] techniques. In addition, another great advantage of our setup is its 3D and highly branched filamentous structure. Moreover, the ability to tune detailed network morphology could offer new knobs to control the lasing action, such as the light localization length and threshold.

We have started preliminary experimentation to explore these issues. Specifically, we doped the NLCE network (see example in Fig. 38c) with laser dye, Rhodamine 6G, thereby creating a potential architecture for a so-called random laser [179, 180]. Thus far, we have successfully created the composite fibrous networks; however, we have not tested their optical/lasing properties. Our ongoing work is directed toward probing the localized modes sustained by the 3D fibrous network. For example, we would like to understand how different modes occupying different network links depend on the branch structure and node number. It is also interesting to study the potentially strong light scattering by the disordered network (*e.g.*, strong scattering compared to a sphere of the same volume of material).

We are also exploring replacement of the fluorescent dyes with light emitting quantum dots or quantum rods. The rationale for this substitution is that the doped laser dyes can suffer from photobleaching during the UV curing procedure, which is necessary for NLCE fabrication. By adopting quantum dots such as CdSe/CdS core/shell structures, the issue is ameliorated. Moreover, the escaped radial director configurations within individual NLCE fiber could further align anisotropic quantum rods into a special and tunable arrangements that could exhibit interesting photonic responses. The corresponding experiment, however, is still in its preliminary stage. A few NLCO/NLCE-QD composites have been fabricated, but whether the doped

QDs were well-dispersed within the liquid crystalline substrates is not yet clarified. Further photonic characterization such as emission measurements are needed, and work is underway along these lines.

## 5.6 Fibrous Nematic-Gold Nanorod Composites

Finally, we briefly introduce our work to make fibrous NLCO-gold nanorod (AuNR) composites, wherein the NLCO structures serve as a template to organize AuNRs.

AuNRs are well known to exhibit strong surface plasmon resonances in the visible light portion of the electromagnetic spectrum; these resonances are induced by the optical-driven collective oscillations of free (conduction) electrons in the metal particles. Their unique optical and electronic properties depend on particle shape, size, aspect ratio, and interparticle separation [181]. AuNRs have also been demonstrated to be aligned either by the local director field of the background liquid crystalline medium [182, 183, 184], or by shear forces during electrospinning processes [185, 186, 187]. These aligned nanoparticle systems exhibit direction-dependent longitudinal surface plasmon resonances (LSPRs). By combining the plasmonic behavior of AuNRs together with our established NLCO structures, whose configuration and geometry are temperature sensitive, we aim to create NLCO-AuNR (and corresponding NLCE-AuNR) composite constructions with novel plasmonic responses.

Following schemes described in Ref. [169], my colleague, Yuchen Wang, synthesized AuNRs with various aspect ratios, which were coated with poly(ethylene glycol) (PEG) ligand (Fig. 45). These AuNRs were then doped into NLCO suspensions following the protocol described in **Section 5.2.5**.

Based on our preliminary result, we found that the doped AuNRs do not alter the

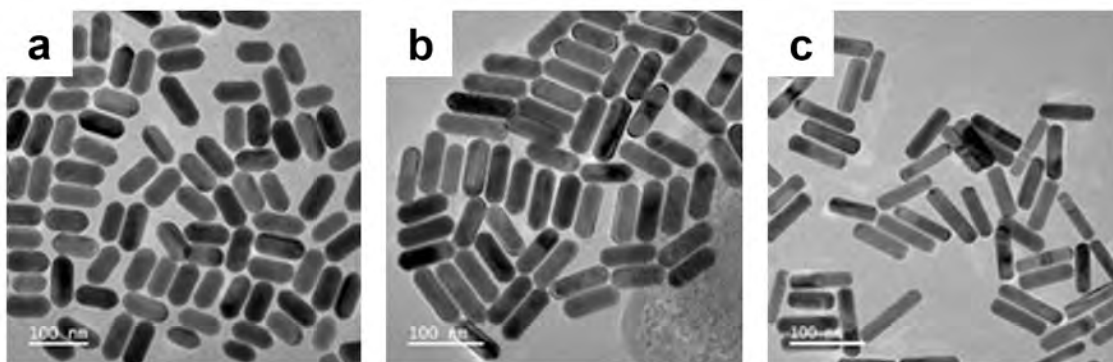


Figure 45: **Gold nanorods with various aspect ratios.** a-c, Transmission electron microscopy (TEM) images of gold nanorods with highly uniform shape. The aspect ratio of AuNRs can be fine-tuned; three of the exemplary batches are shown here. The peak value of their longitudinal surface plasmon resonances are 699 nm, 740 nm, and 800 nm, respectively. Scale bars are 100 nm. These TEM images were taken by my colleague, Yuchen Wang.

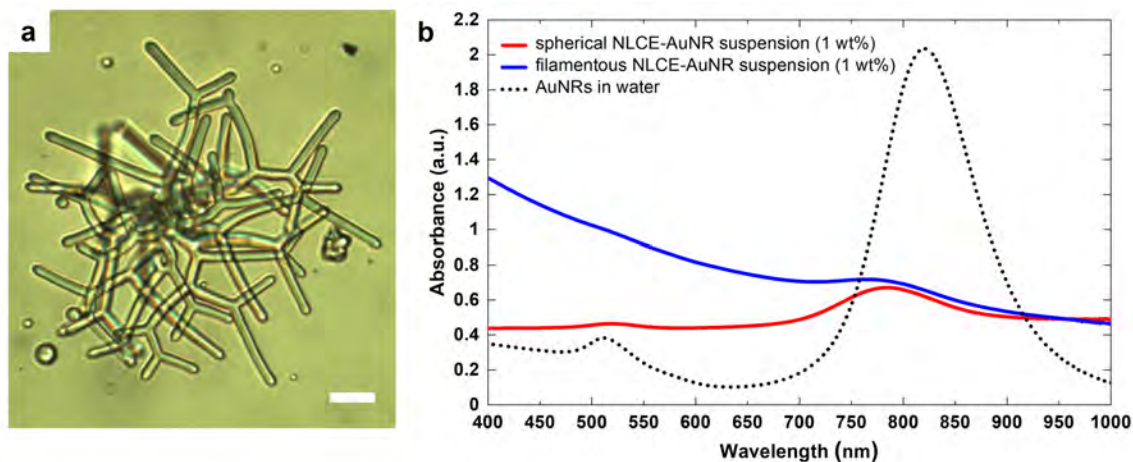


Figure 46: **Gold nanorods doped nematic liquid crystal elastomer structures and UV-VIS-NIR absorption spectra.** a, Optical image of a crosslinked filamentous NLCE-AuNR network suspended in water. Scale bar: 10  $\mu\text{m}$ . b, The UV-VIS-NIR absorption spectra through the sample cells. The red & blue solid curves represent suspensions of the NLCE-AuNR spheres and filamentous NLCE-AuNR network, respectively. The black dotted curve shows the pure AuNRs suspended in water as a reference.

thermo-response of NLCO emulsion drops, which exhibit spherical shapes and radial director configurations at high temperature and filamentous shapes with escaped radial configuration at low temperature (see Fig. 46a; consult **Section 4.3** & **Section 4.5** for results without AuNR dopants). However, as revealed by the UV-VIS-NIR (ultraviolet - visible light - near infrared) absorption spectra, the LSPR signals of the current NLCO/NLCE-AuNR constructions, in both spherical and filamentous geometries, are not yet apparent (see Fig. 46b). The origin of the insignificant absorption spectra may arise from poor dispersion and aggregation of AuNRs within NLCO/NLCE medium. Variation and improvement of detailed synthetic procedure should address this issue; work is underway along these lines. Note, a blue-shift in LSPR caused by AuNR reshaping was also observed (see comparison between the peak value of red/blue solid curve and black dotted curve in Fig. 46b). The reshaping phenomena of AuNRs (*i.e.*, the nanorods will shorten along the long axis) are due to the heating process of NLCO oligomerization [188, 189]. The issue could be resolved by decreasing temperature during oligomerization.

Our ongoing work is directed toward characterizing the thermo-responsive plasmon resonances sustained by the NLCO/NLCE-AuNR composites. Benefit from the temperature-tunable morphology and director configuration of the NLCO substrates, the organization of embedded AuNRs should transform dramatically with respect to temperature. Compared to previous work [190, 191, 192], the features could thus give rise to a more substantial switching in LSPR spectra.

## 5.7 Summary and Future Directions

We utilized the thermo-responsive NLCO suspensions as a platform to make functional materials. Together with their crosslinkable capability and tunable geometry,

the ability of the established micro-structures to “template” embedded functional materials indeed opens up interesting possibilities for creation of responsive soft materials.

First, we demonstrated that the various nematic structures can be crosslinked by UV light into the so-called nematic liquid crystal elastomers. This process occurs within tens of seconds. This goal was our motivation at the outset when designing the experiments discussed in **Chapter 4**. With this method, we realized various “frozen” nematic structures and complex constructions, such as oriented fibrous yarns and free-standing mats. The technique not only enables a simple and scalable approach to make fibers, it also offers a means to study their liquid crystalline structures in detail, with resolution beyond limit of optical microscopy. The actuation issue still needs to be resolved, and this will require attention to the LC polymer chemistry. Once resolved, new functional materials such as tunable waveguides, responsive filtration, and smart fabrics could be achieved.

Secondly, we explored the effects of chiral dopants on the NLC drop morphologies. In particular, the resulting cholesteric nematic develops subsurface spiraling disclination loops and associated redistribution of surfactant molecules absorbed at the interface. The uneven surfactant packing, in turn, gives rise to irregular and spatially patterned interfacial tension. As a result, the samples with longer mean oligomer chain length bud and grow into filaments (after cooling) from the region without underlying disclinations. This type of guidance of detailed topological disclination textures is of fundamental interest and could enable a programmable patterned constructions. Moreover, the same trick can be applied to flat LC-water interface (instead of micro-emulsion drops) for broader applications.

Lastly, we pointed out future research directions regarding functionalities of the fibrous nematic composites. Based on our preliminary experiments, the filamentous

nematic structures serve as templates to organize laser dyes and functional nanoparticles. Specifically, the nanophotonic 3D networks could provide a conceptually new architecture for designing and fabricating random lasers as well as strong light scattering objects. With the quantum dots/rods and gold nanorods embedded in the nematic substrates, we hope to demonstrate novel photonic responses such as temperature-tunable plasmonic devices. Currently, work is directed toward the exploration of these possibilities.

# Chapter 6

## Conclusion and Future Directions

The research presented in this thesis connected elastic properties, containment geometry, and boundary conditions of liquid crystals (LCs) to various associated assemblies. Of particular importance for these experiments and analyses, is the influence of surface anchoring and interfacial tension. The uncovered features suggest new routes to create novel and potentially useful programmable soft materials.

In this concluding chapter, we summarize these results (briefly). In addition, we suggest avenues for further research (briefly).

### **6.1 Textures of Confined Liquid Crystals: Interplay between Elasticity, Surface Anchoring, and Boundary Geometry**

The first research problems, presented in **Chapter 2**, centered on how LCs in Janus drops are influenced by containment geometry and anchoring boundary conditions. This interplay drove assembly/formation of fascinating director configurations/textures in the confined geometries. In this set of experiments, both the nematic LC 5CB and the smectic-A LC 8CB were investigated in the spherical-cap like confinements of Janus LC droplets. These containment geometries are hard to achieve via other approaches. The LCs in the cavities relaxed into stable/metastable textures, and we experimentally analyzed the textures and their relative energies.

The confined nematic LCs in spherical-caps exhibited textures similar to those typically observed in spherical droplets. Specifically, we observed textures with

a single surface boojum defect and with a hedgehog point defect for planar and homeotropic anchoring, respectively.

The smectic LCs confined in homeotropic-anchored Janus drops exhibited much richer behaviors than the nematics. Surprisingly, upon initial formation, instead of settling into a single equilibrium configuration (as occurred for the nematic LCs), three classes of SmA LC textures were recognized and classified. These textures included focal conic domain (FCD) flowers, dislocation rings, and undulations plus dislocation rings. Our research suggested that, of these, the first two textures were metastable. The FCD flowers were the most energetically costly texture, while the texture with dislocation rings plus smectic layer undulations was the cheapest (energetically). A follow-up study showed how the LC texture stability and evolution depend on synthesis procedure in addition to well-known factors such as confinement geometry, boundary anchoring, and bulk LC elasticity. To achieve lowest energy configurations, sufficient time is needed.

The observations thus suggest ways for fabricating complex smectic LC structures in Janus droplets and other confined geometries. Moreover, to the best of our knowledge, the only existing way to generate FCDs in suspended droplets requires interfacial *planar anchoring*. Ours is the first work to report “geometry-driven” FCD textures in a homeotropic-anchored micro-emulsion, which expands possibilities for study smectics in confinement.

The experiments and analyses we performed generate questions for future research. For example, does drop morphology affect LC configuration or vice versa, especially during the texture transition process? What are the quantitative rules for packing FCDs within a cavity? Are there other uses for the ability to precisely control LC defect/texture formation and its evolution in Janus droplets and other containing environments? In the process of carrying out these studies, our preliminary observa-

tions also suggested that the SmA textures tend to form and occupy the entire cavity in a sequential manner; study of texture formation dynamics will be an interesting subject of future work.

## 6.2 Self-assembled Colloidal Packings: Interactions Mediated by Topological Defects in Liquid Crystals

The second study, outlined in **Chapter 3**, investigated LC-driven assembly of embedded colloidal particles. In the experiment, a two-dimensional crystalline packing of colloidal particles residing at the air-nematic (5CB) interface was investigated. Here, the interparticle interactions were produced by topological defects in the LC, *i.e.*, director distortions that extended from the particles on the surface into the bulk LC. We characterized the spatiotemporal dynamics of the 2D colloidal lattice as a function of temperature using video microscopy.

The particles in the self-assembled colloidal monolayer exhibited short-time diffusive motion. Their diffusion coefficients were consistent with a Stokes-Einstein model, wherein the effective viscosity is predominantly that of 5CB. We also quantitatively analyzed the collective motions of the monolayer; that is, we measured the vibrational phonon modes of the crystalline packings which yielded information about the interparticle forces, whose temperature dependence was consistent with expectations based on the temperature-dependence of the elastic moduli of 5CB. The work thus demonstrated a qualitatively new methodology to probe LC properties by measuring the dynamics of trapped colloidal particles.

Specifically, using the particle displacement correlations (displacement covari-

ances), we learned about phonon behaviors of the LC-mediated crystal packings which share similar features to other 2D colloidal crystals with different interaction potentials. For example, the phonon density of states (DOS) exhibited Debye scaling at low frequencies and van Hove-like singularities at higher frequencies. We also uncovered some features about the phonon modes which are new and are perhaps related to quenched disorder in this system class.

Future work, over a larger dynamic range of interparticle separations, could permit a more accurate determination of interaction potentials on the quasi-2D LC-mediated colloidal lattice. It should then be interesting to investigate phase transitions and possible hexatic states in this new class of 2D crystal. Additionally, more work is needed to understand the phonon behaviors with respect to temperature. A rough analysis showed that the range of eigenfrequencies becomes wider as the system temperature decreases, which may partially reflect heterogeneous particle wetting and contact lines relaxation. Potentially, this scenario could offer an experimental technique for study of connections between phonon spectra and disorder.

### **6.3 Shape Transitions of Liquid Crystal Micro-emulsions: Competition between Elasticity and Interfacial Tension**

The third set of experiments, presented in **Chapter 4**, explored how the competition between LC elasticity and interfacial tension can lead to spontaneous and reversible shape transitions of micro-droplets. In this study, micro-emulsion drops containing RM82 NLCOs (with polydisperse chain length distributions) and suspended in a SDS aqueous solution were fabricated. We analyzed the drop morphology with

respect to several control parameters, including temperature, oligomer mean chain length, and surfactant concentration in the aqueous background.

Specifically, at high temperature, the NLCO drops have spherical shape because interfacial tension is dominant. Upon cooling, the interfacial tension decreased while the bulk LC elasticity increased. As a result, the drops evolve from spheres to roughened spheres, flowers, and branched filamentous networks as oligomer mean chain length increased. Surprisingly, our experiments and modeling suggested that molecular heterogeneity (*i.e.*, oligomer chain length polydispersity) is a key feature in the process which leads to chain-length-dependent oligomer segregation within the microdroplet, and thereby tips the balance between interfacial and bulk free energies to drive the observed morphological transitions.

This finding about the role of molecular heterogeneity is unusual. The molecular polydispersity does not disrupt order or impede self-assembly, as it often does in traditional materials. Instead, the molecular heterogeneity facilitates equilibrium transitions among dramatically different morphological structures. Moreover, study of these synthetic systems offers insight about the origin of complex morphologies in the biological world. The diverse surface patterns of pollen grains, for example, have been reported to be promoted by the molecular heterogeneity driven segregation and phase separation, which make connections to our reported mechanism.

Looking to the future, the revealed abilities can be exploited to create soft and highly branched networks with uniform filament size. Further studies of branching behaviors may also provide new insights about assembly and stabilization. Finally, some potential applications based on the setup will be discussed in the following section.

## 6.4 Functionalities of Liquid Crystal Templated Composites

The last set of experiments, presented in **Chapter 5**, initiated exploration of potential functional materials based on the established nematic filamentous networks described in **Chapter 4**. Specifically, we utilized the thermo-responsive NLCO structures as a platform, exploring its potential for crosslinking and the potential uses of resultant crosslinked materials for “templating” embedded functional materials.

In the first and primary experiment, various nematic structures with desired morphologies were permanently locked into liquid crystal elastomers (LCEs) by UV curing. Some complex constructions based on the LCE filamentous structures, such as oriented fibrous yarns and free-standing mats, were also demonstrated. The scheme thus enables a simple and scalable approach to make fibers. Further, the reported technique to rapidly “freeze-in” any desired nematic director configuration (within tens of seconds) offers a means to study the liquid crystalline structures in detail by SEM, whose spatial resolution is much better than that of optical microscopy.

In our preliminary studies, the actuation of the current NLCE fibers were not as yet apparent. Variation of the synthetic chemistry to resolve the issue (*e.g.*, by decreasing crosslinking density or increasing oligomer chain “flexibility”) is therefore a critical subject for future work. Once resolved, new functional materials such as tunable waveguides could be achieved from the yarn-like objects. In a different vein, with its temperature-tunable pore size, the fibrous mats could find use in responsive filtration and smart fabrics.

In a different experiment with the same system, we explored how the chiral dopants can enhance guidance of NLCO surface patterning. Specifically, cholesteric nematics within micro-droplets were demonstrated to generate subsurface spiraling

disclination loops and to redistribute surfactant molecules adsorbed to the interface. The resultant irregular and spatially patterned interfacial tension provides a new way to use programmable surface patterning for filament nucleation and growth from the drops. Looking to the future, the connections between topological disclination textures and surface patterning will also be of fundamental interest. With more understanding, control could enable a programmable constructions. Moreover, the same technique could be applied to other geometries.

Lastly, work directed toward exploration of photonic properties of the self-assembled nematic structures may be promising in the future. Our preliminary experiments revealed that the filamentous nematic networks could serve as templates to organize laser dye and functional nano-particles. For example, the dye-doped nanophotonic 3D networks could serve as a new architecture for random lasers and disordered media with strong scattering. The NLCO/NLCE - quantum dot and NLCO/NLCE - gold nanorod composites, could also potentially exhibit novel photonic responses as temperature-tunable plasmonic devices.

Though the research described in **Chapter 5** is unpublished, these preliminary experiments nucleate ideas for future experiments and point to future research directions.

# Bibliography

- [1] Jeong, J., Gross, A., Wei, W.-S., Tu, F., Lee, D., Collings, P. J. & Yodh, A. G. Liquid crystal Janus emulsion droplets: preparation, tumbling, and swimming. *Soft Matter* **11**, 6747-6754 (2015).
- [2] Wei, W.-S., Gharbi, M. A., Lohr, M. A., Still, T., Gratale, M. D., Lubensky, T. C., Stebe, K. J. & Yodh, A. G. Dynamics of ordered colloidal particle monolayers at nematic liquid crystal interfaces. *Soft Matter* **12**, 4715-4724 (2016).
- [3] Wei, W.-S., Xia, Y., Ettinger, S., Yang, S. & Yodh, A. G. Molecular heterogeneity drives reconfigurable nematic liquid crystal drops. *Nature* **576**, 433-436 (2019).
- [4] Wei, W.-S., Jeong, J., Collings, P. J. & Yodh, A. G. Focal conic, dislocation ring, and undulation textures in smectic liquid crystal Janus droplets. *in prep.*
- [5] White, T. J. & Broer, D. J. Programmable and adaptive mechanics with liquid crystal polymer networks and elastomers. *Nature Mater.* **14**, 1087-1098 (2015).
- [6] Lopez-Leon, T. & Fernandez-Nieves, A. Drops and shells of liquid crystal. *Colloid Polym. Sci.* **289**, 345-359 (2011).
- [7] Ryu, S. H. & Yoon, D. K. Liquid crystal phases in confined geometries. *Liquid Crystals* **43**, 1951-1972 (2016).
- [8] Urbanski, M., Reyes, C. G., Noh, J., Sharma, A., Geng, Y., Jampani, V. S. R. & Lagerwall, J. P. Liquid crystals in micron-scale droplets, shells and fibers. *J. Phys.: Condens. Matter* **29**, 133003 (2017).
- [9] Pratibha, R. & Madhusudana, N. V. Cylindrical growth of smectic A liquid crystals from the isotropic phase in some binary mixtures. *J. Phys. II France* **2**, 383-400 (1992).
- [10] Kim, Y. H., Yoon, D. K., Choi, M. C., Jeong, H. S., Kim, M. W., Lavrentovich, O. D. & Jung, H. T. Confined self-assembly of toric focal conic domains (the effects of confined geometry on the feature size of toric focal conic domains). *Langmuir* **25**, 1685-1691 (2009).
- [11] Honglawan, A., Beller, D. A., Cavallaro, M., Kamien, R. D., Stebe, K. J. & Yang, S. Pillar-assisted epitaxial assembly of toric focal conic domains of smectic-A liquid crystals. *Adv. Mater.* **23**, 5519-5523 (2011).

- [12] Meyer, C., Le Cunff, L., Belloul, M. & Foyart, G. Focal conic stacking in smectic a liquid crystals: Smectic flower and Apollonius tiling. *Materials* **2**, 499-513 (2009).
- [13] Gharbi, M. A., Liu, I. B., Luo, Y., Serra, F., Bade, N. D., Kim, H. N., Xia, Y., Kamien, R. D., Yang, S. & Stebe, K. J. Smectic gardening on curved landscapes. *Langmuir* **31**, 11135-11142 (2015).
- [14] Serra, F., Gharbi, M. A., Luo, Y., Liu, I. B., Bade, N. D., Kamien, R. D., Yang, S. & Stebe, K. J. Curvature-driven, one-step assembly of reconfigurable smectic liquid crystal compound eye lenses. *Adv. Optical Mater.* **3**, 1287-1292 (2015).
- [15] Beller, D. A., Gharbi, M. A., Honglawan, A., Stebe, K. J., Yang, S. & Kamien, R. D. Focal conic flower textures at curved interfaces. *Phys. Rev. X* **3**, 041026 (2013).
- [16] Gharbi, M. A., Beller, D. A., Sharifi-Mood, N., Gupta, R., Kamien, R. D., Yang, S. & Stebe, K. J. Elastocapillary driven assembly of particles at free-standing smectic-A films. *Langmuir* **34**, 2006-2013 (2018).
- [17] Lavrentovich, O. D. Hierarchy of defect structures in space filling by flexible smectic-A layers. *Sov. Phys. JETP* **64**, 1666-1676 (1986).
- [18] Blanc, C. & Kleman, M. The confinement of smectics with a strong anchoring. *Eur. Phys. J. E* **4**, 241-251 (2001).
- [19] Lee, G., Araoka, F., Ishikawa, K., Momoi, Y., Haba, O., Yonetake, K. & Takezoe, H. Photoinduced ordering transition in microdroplets of liquid crystals with azo-dendrimer. *Part. Part. Syst. Charact.* **30**, 847-852 (2013).
- [20] Concellón, A., Zentner, C. A. & Swager, T. M. Dynamic complex liquid crystal emulsions. *J. Am. Chem. Soc.* **141**, 18246-18255 (2019).
- [21] Umbanhowar, P. B., Prasad, V. & Weitz, D.A. Monodisperse emulsion generation via drop break off in a coflowing stream. *Langmuir* **16**, 347-351 (2000).
- [22] Jeong, J., Um, E., Park, J. K. & Kim, M. W. One-step preparation of magnetic Janus particles using controlled phase separation of polymer blends and nanoparticles. *RSC Adv.* **3**, 11801-11806 (2013).
- [23] Guzowski, J., Korczyk, P. M., Jakiela, S. & Garstecki, P. The structure and stability of multiple micro-droplets. *Soft Matter* **8**, 7269-7278 (2012).
- [24] de Gennes, P. G., & Prost, J. *The Physics of Liquid Crystals*. 2nd. Ed. (Clarendon Press, Oxford, 1993).

- [25] Drzaic, P. S. *Liquid Crystal Dispersions*. (World Scientific, Singapore, 1995).
- [26] Evans, J. S., Ackerman, P. J., Broer, D. J., van de Lagemaat, J. & Smalyukh, I. I. Optical generation, templating, and polymerization of three-dimensional arrays of liquid-crystal defects decorated by plasmonic nanoparticles. *Phys. Rev. E* **87**, 032503 (2013).
- [27] Kim, Y. H., Lee, J. O., Jeong, H. S., Kim, J. H., Yoon, E. K., Yoon, D. K., Yoon, J. B. & Jung, H. T. Optically selective microlens photomasks using self-assembled smectic liquid crystal defect arrays. *Adv. Mater.* **22**, 2416-2420 (2010).
- [28] Kim, Y. H., Jeong, H. S., Kim, J. H., Yoon, E. K., Yoon, D. K. & Jung, H.T. Fabrication of two-dimensional dimple and conical microlens arrays from a highly periodic toroidal-shaped liquid crystal defect array. *J. Mater. Chem.* **20**, 6557-6561 (2010).
- [29] Kim, J. H., Kim, Y. H., Jeong, H. S., Srinivasarao, M., Hudson, S. D. & Jung, H. T. Thermally responsive microlens arrays fabricated with the use of defect arrays in a smectic liquid crystal. *RSC Adv.* **2**, 6729-6732 (2012).
- [30] Friedel, G. Les états mésomorphes de la matière. *Ann. Phys. Paris* **9**, 273-474 (1922).
- [31] Bragg, W. Liquid crystals. *Nature* **133**, 445-456 (1934).
- [32] Sethna, J. P. & Kléman, M. Spheric domains in smectic liquid crystals. *Phys. Rev. A* **26**, 3037 (1982).
- [33] Kléman, M. & Lavrentovich, O. D. Grain boundaries and the law of corresponding cones in smectics. *Eur. Phys. J. E* **2**, 47-57 (2000).
- [34] Williams, C. E. & Kléman, M. Dislocations, grain boundaries and focal conics in smectics A. *J. Phys. Colloq.* **36**, C1-315 (1975).
- [35] Aharoni, H., Machon, T. & Kamien, R. D. Composite dislocations in smectic liquid crystals. *Phys. Rev. Lett.* **118**, 257801 (2017).
- [36] Clark, N. A. & Meyer, R. B. Strain-induced instability of monodomain smectic A and cholesteric liquid crystals. *Appl. Phys. Lett.* **22**, 493-494 (1973).
- [37] Delaye, M., Ribotta, R. & Durand, G. Buckling instability of the layers in a smectic-A liquid crystal. *Phys. Lett. A* **44**, 139-140 (1973).

- [38] Conradi, M., Zihlerl, P., Šarlah, A. & Mušević, I. Colloids on free-standing smectic films. *Eur. Phys. J. E* **20**, 231-236 (2006).
- [39] Liang, H. L., Schymura, S., Rudquist, P. & Lagerwall, J. Nematic-smectic transition under confinement in liquid crystalline colloidal shells. *Phys. Rev. Lett.* **106**, 247801 (2011).
- [40] Lopez-Leon, T., Fernandez-Nieves, A., Nobili, M. & Blanc, C. Nematic-smectic transition in spherical shells. *Phys. Rev. Lett.* **106**, 247802 (2011).
- [41] Selmi, M., Loudet, J. C., Dolganov, P. V., Othman, T. & Cluzeau, P. Structures in the meniscus of smectic membranes: the role of dislocations. *Soft Matter* **13**, 3649-3663 (2017).
- [42] Schüring, H., Thieme, C. & Stannarius, R. Surface tensions of smectic liquid crystals. *Liquid Crystals* **28**, 241-252 (2001).
- [43] P. Oswald & P. Pieranski. *Smectic and Columnar Liquid Crystals: Concepts and Physical Properties illustrated by Experiments* (Taylor & Francis, Boca Raton, 2005).
- [44] Peddireddy, K., Kumar, P., Thutupalli, S., Herminghaus, S. & Bahr, C. Solubilization of thermotropic liquid crystal compounds in aqueous surfactant solutions. *Langmuir* **28**, 12426-12431 (2012).
- [45] Herminghaus, S., Maass, C. C., Krüger, C., Thutupalli, S., Goehring, L. & Bahr, C. Interfacial mechanisms in active emulsions. *Soft Matter* **10**, 7008-7022 (2014).
- [46] Pieranski, P. Two-dimensional interfacial colloidal crystals. *Phys. Rev. Lett.* **45**, 569–572 (1980).
- [47] Aveyard, R., Clint, J. H., Nees, D. & Paunov, V. N. Compression and structure of monolayers of charged latex particles at air/water and octane/water interfaces. *Langmuir* **16**, 1969–1979 (2000).
- [48] Nikolaidis, M. G., Bausch, A. R., Hsu, M. F., Dinsmore, A. D., Brenner, M. P., Gay, C. & Weitz, D. A. Electric-field-induced capillary attraction between like-charged particles at liquid interfaces. *Nature* **420**, 299–301 (2002).
- [49] Aveyard, R., Binks, B., Clint, J., Fletcher, P., Horozov, T., Neumann, B., Paunov, V., Annesley, J., Botchway, S., Nees, D., Parker, A., Ward, A. & Burgess, A. Measurement of long-range repulsive forces between charged particles at an oil-water interface. *Phys. Rev. Lett.* **88**, 246102 (2002).

- [50] Park, B. J., Pantina, J. P., Furst, E. M., Oettel, M., Reynaert, S. & Vermant, J. Direct measurements of the effects of salt and surfactant on interaction forces between colloidal particles at water-oil interfaces. *Langmuir* **24**, 1686–1694 (2008).
- [51] Zahn, K., Wille, A., Maret, G., Sengupta, S. & Nielaba, P. Elastic properties of 2D colloidal crystals from video microscopy. *Phys. Rev. Lett.* **90**, 155506 (2003).
- [52] Assoud, L., Ebert, F., Keim, P., Messina, R., Maret, G. & Löwen, H. Ultrafast quenching of binary colloidal suspensions in an external magnetic field. *Phys. Rev. Lett.* **102**, 238301 (2009).
- [53] Gasser, U., Eisenmann, C., Maret, G. & Keim, P. Melting of crystals in two dimensions. *Chem. Phys. Chem.* **11**, 963–970 (2010).
- [54] Brown, A. B. D., Smith, C. G. & Rennie, A. R. Fabricating colloidal particles with photolithography and their interactions at an air-water interface. *Phys. Rev. E* **62**, 951–960 (2000).
- [55] Stamou, D., Duschl, C. & Johannsmann, D. Long-range attraction between colloidal spheres at the air-water interface: The consequence of an irregular meniscus. *Phys. Rev. E* **62**, 5263–5272 (2000).
- [56] Loudet, J. C., Alsayed, A. M., Zhang, J. & Yodh, A. G. Capillary interactions between anisotropic colloidal particles. *Phys. Rev. Lett.* **94**, 018301 (2005).
- [57] Oettel, U. M. & Dietrich, S. Colloidal interactions at fluid interfaces. *Langmuir* **24**, 1425–1441 (2008).
- [58] Smalyukh, I. I., Chernyshuk, S., Lev, B. I., Nych, A. B., Ognysta, U., Nazarenko, V. G. & Lavrentovich, O. D. Ordered Droplet structures at the liquid crystal surface and elastic-capillary colloidal interactions. *Phys. Rev. Lett.* **93**, 117801 (2004).
- [59] Nych, A. B., Ognysta, U. M., Pergamenschchik, V. M., Lev, B. I., Nazarenko, V. G., Mušević, I., Škarabot, M. & Lavrentovich, O. D. Coexistence of two colloidal crystals at the nematic-liquid-crystal–air interface. *Phys. Rev. Lett.* **98**, 057801 (2007).
- [60] Yamamoto, T. & Yoshida, M. Self-assembled pseudo-hexagonal structures of colloidal particles at air–liquid crystal interface. *Appl. Phys. Express* **2**, 101501 (2009).

- [61] Koenig, G. M., Lin, I.-H. & Abbott, N. L. Chemoresponsive assemblies of microparticles at liquid crystalline interfaces. *Proc. Natl. Acad. Sci. USA* **107**, 3998–4003 (2010).
- [62] Bai, Y. & Abbott, N. L. Recent advances in colloidal and interfacial phenomena involving liquid crystals. *Langmuir* **27**, 5719–5738 (2010).
- [63] Gharbi, M. A., Nobili, M., In, M., Prévot, G., Galatola, P., Fournier, J.-B. & Blanc, C. Behavior of colloidal particles at a nematic liquid crystal interface. *Soft Matter* **7**, 1467–1471 (2011).
- [64] Cavallaro, M., Gharbi, M. A., Beller, D. A., Čopar, S., Shi, Z., Baumgart, T., Yang, S., Kamien, R. D. & Stebe, K. J. Exploiting imperfections in the bulk to direct assembly of surface colloids. *Proc. Natl. Acad. Sci. USA* **110**, 18804–18808 (2013).
- [65] Karat, P. P. & Madhusudana, N. V. Elasticity and orientational order in some 4'-n-alkyl-4-cyanobiphenyls: Part II. *Mol. Cryst. Liq. Cryst.* **40**, 239–245 (1977).
- [66] Bunning, J. D., Faber, T. E. & Sherrell, P. L. The Frank constants of nematic 5CB at atmospheric pressure. *J. Phys.* **42**, 1175–1182 (1981).
- [67] Madhusudana, N. V. & Pratibha, R. Elasticity and orientational order in some cyanobiphenyls: Part IV. Reanalysis of the data. *Mol. Cryst. Liq. Cryst.* **89**, 249–257 (1982).
- [68] Chen, G.-P., Takezoe, H. & Fukuda, A.. Determination of  $K_i$  ( $i = 1-3$ ) and  $\mu_j$  ( $j = 2-6$ ) in 5CB by observing the angular dependence of Rayleigh line spectral widths. *Liq. Cryst.* **5**, 341–347 (1989).
- [69] Cui, M. & Kelly, J. R. Temperature dependence of visco-elastic properties of 5CB. *Mol. Cryst. Liq. Cryst. Sci. Technol., Sect. A* **331**, 49–57 (1999).
- [70] Chmielewski, A. G. Viscosity coefficients of some nematic liquid crystals. *Mol. Cryst. Liq. Cryst.* **132**, 339–352 (1986).
- [71] Letcher, S. V. Ultrasonic measurements in liquid crystals. *J. Acoust. Soc. Am.* **53**, 307 (1973).
- [72] Kiry, F. & Martinoty, P. Ultrasonic investigation of anisotropic viscosities in a nematic liquid-crystal. *J. Phys.* **38**, 153–157 (1977).
- [73] Skarp, K., Lagerwall, S. T. & Stebler, B. Measurements of hydrodynamic parameters for nematic 5CB. *Mol. Cryst. Liq. Cryst.* **60**, 215–236 (1980).

- [74] Herba, H., Szymański, A. & Drzymala, A.. Experimental test of hydrodynamic theories for nematic liquid crystals. *Mol. Cryst. Liq. Cryst.* **127**, 153–158 (1985).
- [75] Orr, R. & Pethrick, R. A. Viscosity coefficients of nematic liquid crystals: I. Oscillating plate viscometer measurements and rotational viscosity measurements: K15. *Liq. Cryst.* **38**, 1169–1181 (2011).
- [76] Blanc, C., Coursault, D. & Lacaze E. Ordering nano- and microparticles assemblies with liquid crystals. *Liq. Cryst. Rev.* **1**, 83-109 (2013).
- [77] Gharbi, M. A., Nobili, M. & Blanc, C. Use of topological defects as templates to direct assembly of colloidal particles at nematic interfaces. *J. Colloid Interface Sci.* **417**, 250-255 (2014).
- [78] Crocker, J. C. & Grier, D. G. Methods of digital video microscopy for colloidal studies. *J. Colloid Interface Sci.* **179**, 298-310 (1996).
- [79] Chen, K., Ellenbroek, W. G., Zhang, Z., Chen, D. T. N., Yunker, P. J., Henkes, S., Brito, C., Dauchot, O., van Saarloos, W., Liu, A. J. & Yodh, A. G. Low-frequency vibrations of soft colloidal glasses. *Phys. Rev. Lett.* **105**, 025501 (2010).
- [80] Ghosh, A., Chikkadi, V. K., Schall, P., Kurchan, J. & Bonn, D. Density of states of colloidal glasses. *Phys. Rev. Lett.* **104**, 248305 (2010).
- [81] Kaya, D., Green, N. L., Maloney, C. E. & Islam, M. F. Normal modes and density of states of disordered colloidal solids. *Science* **329**, 656-658 (2010).
- [82] Brito, C., Dauchot, O., Biroli, G. & Bouchaud, J.-P. Elementary excitation modes in a granular glass above jamming. *Soft Matter* **6**, 3013-3022 (2010).
- [83] Schindler, M. & Maggs, A. C. Truncated correlations in video microscopy of colloidal solids. *Soft Matter* **8**, 3864-3874 (2012).
- [84] Alexander, S. Amorphous solids: their structure, lattice dynamics and elasticity. *Phys. Rep.* **296**, 65-236 (1998).
- [85] DiDonna, B. A. & Lubensky, T. C. Nonaffine correlations in random elastic media. *Phys. Rev. E* **72**, 066619 (2005).
- [86] Burda, Z., Görlich, A., Jarosz, A. & Jurkiewicz, J. Signal and noise in correlation matrix. *Phys. A* **343**, 295-310 (2004).

- [87] Hasan, A. & Maloney, C. E. Inferring elastic properties of an fcc crystal from displacement correlations: Subspace projection and statistical artifacts. *Phys. Rev. E* **90**, 062309 (2014).
- [88] Lemarchand, C. A., Maggs, A. C. & Schindler, M. Elastic fluctuations as observed in a confocal slice. *EPL* **97**, 48007 (2012).
- [89] Henkes, S., Brito, C. & Dauchot, O. Extracting vibrational modes from fluctuations: a pedagogical discussion. *Soft Matter* **8**, 6092-6109 (2012).
- [90] Chen, K., Still, T., Schoenholz, S., Aptowicz, K. B., Schindler, M., Maggs, A. C., Liu, A. J. & Yodh, A. G. Phonons in two-dimensional soft colloidal crystals. *Phys. Rev. E* **88**, 022315 (2013).
- [91] Russel, W. B., Saville, D. A. & Schowalter, W. R. *Colloidal Dispersions* (Cambridge University Press, 1992).
- [92] Miesowicz, M. The three coefficients of viscosity of anisotropic liquids. *Nature* **158**, 27 (1946).
- [93] Ericksen, J. L. Anisotropic fluids. *Arch. Ration. Mech. Anal.* **4**, 231-237 (1959).
- [94] Leslie, F. M. Some constitutive equations for liquid crystals. *Arch. Ration. Mech. Anal.* **28**, 265-283 (1968).
- [95] Ruhwandl, R. W. & Terentjev, E. M. Friction drag on a particle moving in a nematic liquid crystal. *Phys. Rev. E* **54**, 5204-5210 (1996).
- [96] Stark, H. & Ventzki, D. Stokes drag of spherical particles in a nematic environment at low Ericksen numbers. *Phys. Rev. E* **64**, 031711 (2001).
- [97] Loudet, J. C., Hanusse, P. & Poulin, P. Stokes drag on a sphere in a nematic liquid crystal. *Science* **306**, 1525 (2004).
- [98] Rey, A. D. A model of capillary rise of nematic liquid crystals. *Langmuir* **19**, 3677-3685 (2003).
- [99] Bottger, A., Frenkel, D., Van De Riet, E. & Zijlstra, R. Diffusion of brownian particles in the isotropic phase of a nematic liquid crystal. *Liq. Cryst.* **2**, 539-547 (1987).
- [100] Danov, K., Aust, R., Durst, F. & Lange, U. Influence of the surface viscosity on the hydrodynamic resistance and surface diffusivity of a large Brownian particle. *J. Colloid Interface Sci.* **175**, 36-45 (1995).

- [101] Ashcroft, N. W. & Mermin, N. D. *Solid State Physics* (Holt, Rinehart and Winston, New York, 1976).
- [102] Keim, P., Maret, G., Herz, U. & von Grünberg, H. H. Harmonic lattice behavior of two-dimensional colloidal crystals. *Phys. Rev. Lett.* **92**, 215504 (2004).
- [103] Silbert, L. E., Liu, A. J. & Nagel, S. R. Normal modes in model jammed systems in three dimensions. *Phys. Rev. E* **79**, 021308 (2009).
- [104] Vitelli, V., Xu, N., Wyart, M., Liu, A. J. & Nagel, S. R. Heat transport in model jammed solids. *Phys. Rev. E* **81**, 021301 (2010).
- [105] Still, T., Goodrich, C. P., Chen, K., Yunker, P. J., Schoenholz, S., Liu, A. J. & Yodh, A. G. Phonon dispersion and elastic moduli of two-dimensional disordered colloidal packings of soft particles with frictional interactions. *Phys. Rev. E* **89**, 012301 (2014).
- [106] Kittel, C. *Introduction to Solid State Physics* (Wiley, New York, 1976).
- [107] Poulin, P., Cabuil, V. & Weitz, D. A. Direct measurement of colloidal forces in an anisotropic solvent. *Phys. Rev. Lett.* **79**, 4862-4865 (1997).
- [108] Smalyukh, I. I., Lavrentovich, O. D., Kuzmin, A. N., Kachynski, A. V. & Prasad, P. N. Elasticity-mediated self-organization and colloidal interactions of solid spheres with tangential anchoring in a nematic liquid crystal. *Phys. Rev. Lett.* **95**, 157801 (2005).
- [109] Kotar, J., Vilfan, M., Osterman, N., Babič, D., Čopič, M. & Poberaj, I. Interparticle potential and drag coefficient in nematic colloids. *Phys. Rev. Lett.* **96**, 207801 (2006).
- [110] Nazarenko, V. G., Nych, A. B. & Lev, B. I. Crystal structure in nematic emulsion. *Phys. Rev. Lett.* **87**, 075504 (2001).
- [111] Oettel, M., Domínguez, A., Tasinkevych, M. & Dietrich, S. Effective interactions of colloids on nematic films. *Eur. Phys. J. E* **28**, 99-111 (2009).
- [112] Sacanna, S. & David, D. J. Shape-anisotropic colloids: Building blocks for complex assemblies. *Curr. Opin. Colloid Interface Sci.* **16**, 96-105 (2011).
- [113] Rossi, L., Sacanna, S., Irvine, W. T., Chaikin, P. M., Pine, D. J. & Philipse, A. P. Cubic crystals from cubic colloids. *Soft Matter* **9**, 4139-4142 (2011).

- [114] Beller, D. A., Gharbi, M. A. & Liu, I. B. Shape-controlled orientation and assembly of colloids with sharp edges in nematic liquid crystals. *Soft Matter* **11**, 1078-1086 (2015).
- [115] Shields IV, C. W., Kim, Y.-K., Han, K., Murphy, A. C., Scott, A. J., Abbott, N. L. & Velev, O. D. Control of the folding dynamics of self-reconfiguring magnetic microbots using liquid crystallinity. *Adv. Intell. Syst.* **2**, 1900114 (2020).
- [116] Kaz, D. M., McGorty, R., Mani, M., Brenner, M. P. & Manoharan, V. N. Physical ageing of the contact line on colloidal particles at liquid interfaces. *Nat. Mater.* **11**, 138-142 (2012).
- [117] Dufresne, E. R., Noh, H., Saranathan, V., Mochrie, S. G. J., Cao, H. & Prum, R. O. Self-assembly of amorphous biophotonic nanostructures by phase separation. *Soft Matter* **5**, 1792-1795 (2009).
- [118] Saranathan, V., Osuji, C. O., Mochrie, S. G., Noh, H., Narayanan, S., Sandy, A., Dufresne, E. R. & Prum, R. O. Structure, function, and self-assembly of single network gyroid ( $I4_132$ ) photonic crystals in butterfly wing scales. *Proc. Natl. Acad. Sci. USA* **107**, 11676-11681 (2010).
- [119] Lavrentovich, M. O., Horsley, E. M., Radja, A., Sweeney, A. M. & Kamien, R. D. First-order patterning transitions on a sphere as a route to cell morphology. *Proc. Natl. Acad. Sci. USA* **113**, 5189-5194 (2016).
- [120] Radja, A., Horsley, E. M., Lavrentovich, M. O. & Sweeney, A. M. Pollen cell wall patterns form from modulated phases. *Cell* **176** 856-868 (2019).
- [121] Fasolo, M. & Sollich, P. Equilibrium phase behavior of polydisperse hard spheres. *Phys. Rev. Lett.* **91**, 068301 (2003).
- [122] Zaccarelli, E., Valeriani, C., Sanz, E., Poon, W. C. K., Cates, M. E. & Pusey, P. N. Crystallization of hard-sphere glasses. *Phys. Rev. Lett.* **103**, 135704 (2009).
- [123] Liddle, S. M., Narayanan, T. & Poon, W. C. K. Polydispersity effects in colloid-polymer mixtures. *J. Phys. Condens. Matter* **23**, 194116 (2011).
- [124] Lavrentovich, O. D., Nastishin, Y. A., Kulishov, V. I., Narkevich, Y. S., Tolochko, A. S. & Shiyonovskii, S. V. Helical smectic A. *Europhys. Lett.* **13**, 313-318 (1990).
- [125] Mejia, A. F., He, P., Netemeyer, M., Luo, D., Marquez, M. & Cheng, Z. Surface-controlled shape design of discotic micro-particles. *Soft Matter* **6**, 4885-4894 (2010).

- [126] Gibaud, T., Barry, E., Zakhary, M. J., Henglin, M., Ward, A., Yang, Y., Berciu, C., Oldenbourg, R., Hagan, M. F., Nicastrò, D., Meyer, R. B. & Dogic, Z. Reconfigurable self-assembly through chiral control of interfacial tension. *Nature* **481**, 348–351 (2012).
- [127] Jeong, J., Davidson, Z. S., Collings, P. J., Lubensky, T. C. & Yodh, A. G. Chiral symmetry breaking and surface faceting in chromonic liquid crystal droplets with giant elastic anisotropy. *Proc. Natl. Acad. Sci. USA* **111**, 1742–1747 (2014).
- [128] Denkov, N., Tcholakova, S., Lesov, I., Cholakova, D. & Smoukov, S. K. Self-shaping of oil droplets via the formation of intermediate rotator phases upon cooling. *Nature* **528**, 392–395 (2015).
- [129] Guttman, S., Sapir, Z., Schultz, M., Butenko, A. V., Ocko, B. M., Deutsch, M. & Sloutskin, E. How faceted liquid droplets grow tails. *Proc. Natl. Acad. Sci. USA* **113**, 493–496 (2016).
- [130] Virchow, R. Ueber das ausgebreitete Vorkommen einer dem Nervenmark analogen Substanz in den thierischen Geweben. *Virchows Arch.* **6**, 562–572 (1854).
- [131] Toquer, G., Phou, T., Monge, S., Grimaldi, A., Nobili, M. & Blanc, C. Colloidal shape controlled by molecular adsorption at liquid crystal interfaces. *J. Phys. Chem. B* **112**, 4157–4160 (2008).
- [132] Peddireddy, K., Kumar, P., Thutupalli, S., Herminghaus, S. & Bahr, C. Myelin structures formed by thermotropic smectic liquid crystals. *Langmuir* **29**, 15682–15688 (2013).
- [133] Ware, T. H., McConney, M. E., Wie, J. J., Tondiglia, V. P. & White, T. J. Voxelated liquid crystal elastomers. *Science* **347**, 982–984 (2015).
- [134] Adamson, A. W. & Gast, A. P. *Physical Chemistry of Surfaces* Ch. 2. (Wiley & Sons, New York 6th ed. 1997).
- [135] Daerr, A. & Mogne, A. Pendent\_drop: an imagej plugin to measure the surface tension from an image of a pendent drop. *J. Open Res. Softw.* **4**, e3 (2016).
- [136] Gannon, M. G. J. & Faber, T. E. The surface tension of nematic liquid crystals. *Philos. Mag. A* **37**, 117–135 (1978).
- [137] Wu, J. & Mather, P. T. Interfacial tension of a liquid crystalline polymer in an isotropic polymer matrix. *Macromolecules* **38**, 7343–7351 (2005).
- [138] Li, X. & Denn, M. M. Interface between a liquid crystalline polymer and a flexible polymer. *Macromolecules* **35**, 6446–6454 (2002).

- [139] Butt, H. J., Graf, K. & Kappl, M. *Physics and Chemistry of Interfaces* Ch. 3. (Wiley & Sons, Weinheim 2006).
- [140] Schiele, K. & Trimper, S. On the elastic constants of a nematic liquid crystal. *Phys. Status. Solidi. B* **118**, 267–274 (1983).
- [141] Ciferri, A., Krigbaum, W. R. & Meyer, R. B. *Polymer Liquid Crystals* Ch. 6 (Academic, New York, 1982).
- [142] Kamien, R. D. & Toner, J. Anomalous elasticity of polymer cholesterics. *Phys. Rev. Lett.* **74**, 3181–3184 (1995).
- [143] Kasten, H. & Strobl, G. Nematic wetting at the free surface of 4-cyano-4'-n-alkyl-biphenyls. *J. Chem. Phys.* **103**, 6768–6774 (1995).
- [144] Tintaru, M., Moldovan, R., Beica, T. & Frunza, S. Surface tension of some liquid crystals in the cyanobiphenyl series. *Liq. Cryst.* **28**, 793–797 (2001).
- [145] Lubensky, T. C., Pettey, D., Currier, N. & Stark, H. Topological defects and interactions in nematic emulsions. *Phys. Rev. E* **57**, 610–625 (1998).
- [146] Cladis, P. E. & Kléman, M. Non-singular disclinations of strength  $S = +1$  in nematics. *J. Phys. France* **33**, 591–598 (1972).
- [147] Meyer, R. B. On the existence of even indexed disclinations in nematic liquid crystals. *Phil. Mag.* **27**, 405–424 (1973).
- [148] Allender, D. W., Crawford, G. P. & Doane, J. W. Determination of the liquid-crystal surface elastic constant  $K_{24}$ . *Phys. Rev. Lett.* **67**, 1442–1445 (1991).
- [149] Crawford, G. P., Allender, D. W. & Doane, J. W. Surface elastic and molecular-anchoring properties of nematic liquid crystals confined to cylindrical cavities. *Phys. Rev. A* **45**, 8693–8708 (1992).
- [150] Burylov, S. V. Equilibrium configuration of a nematic liquid crystal confined to a cylindrical cavity. *J. Exp. Theor. Phys.* **85**, 873–886 (1997).
- [151] Muševič, I. *Liquid Crystal Colloids* Ch. 7 (Springer, Switzerland 2017).
- [152] Frank, F. C. I. Liquid crystals. On the theory of liquid crystals. *Discuss. Faraday Soc.* **25**, 19–28 (1958).
- [153] Oseen, C. W. The theory of liquid crystals. *Trans. Faraday Soc.* **29**, 883–899 (1933).

- [154] Nehring, J. & Saupe, A. On the elastic theory of uniaxial liquid crystals. *J. Chem. Phys.* **54**, 337–343 (1971).
- [155] Barbero, G. & Oldano, C. Derivative-dependent surface-energy terms in nematic liquid crystals. *Nuovo Cimento D* **6**, 479–493 (1985).
- [156] Sparavigna, A., Komitov, L. & Strigazzi, A. Hybrid aligned nematics and second order elasticity. *Phys. Scr.* **43**, 210 (1991).
- [157] Rapini, A. & Papoular, M. Distorsion d’une lamelle nématique sous champ magnétique conditions d’ancrage aux parois. *J. Phys. Colloques* **30**, C4-54–56 (1969).
- [158] Bradshaw, M. J., Raynes, E. P., Bunning, J. D. & Faber, T. E. The Frank constants of some nematic liquid crystals. *J. Phys. France* **46**, 1513–1520 (1985).
- [159] Zhou, S., Neupane, K., Nastishin, Y. A., Baldwin, A. R., Shiyankovskii, S. V., Lavrentovich, O. D., & Sprunt, S. Elasticity, viscosity, and orientational fluctuations of a lyotropic chromonic nematic liquid crystal disodium cromoglycate. *Soft Matter* **10**, 6571–6581 (2014).
- [160] Xia, Y., Serra, F., Kamien, R. D., Stebe, K. J. & Yang, S. Direct mapping of local director field of nematic liquid crystals at the nanoscale. *Proc. Natl Acad. Sci. USA* **112**, 15291–15296 (2015).
- [161] Yokoyama, H. & van Sprang, H. A. A novel method for determining the anchoring energy function at a nematic liquid crystal-wall interface from director distortions at high fields. *J. Appl. Phys.* **57**, 4520–4526 (1985).
- [162] Yang, F., Ruan, L. & Sambles, J. R. Homeotropic polar anchoring energy of a nematic liquid crystal using the fully leaky waveguide technique. *J. Appl. Phys.* **88**, 6175–6182 (2000).
- [163] Škarabot, M., Osmanagić, E. & Mušević, I. Surface anchoring of nematic liquid crystal 8OCB on a DMOAP-silanated glass surface. *Liq. Cryst.* **33**, 581–585 (2006).
- [164] Terentjev, E. M. Density functional model of anchoring energy at a liquid crystalline polymer–solid interface. *J. Phys. II France* **5**, 159-170 (1995).
- [165] Elias, F., Clarke, S. M., Peck, R. & Terentjev, E. M. Nematic order drives phase separation in polydisperse liquid crystalline polymers. *Macromolecules* **33**, 2060-2068 (2000).

- [166] Cholakova, D., Valkova, Z., Tcholakova, S., Denkov, N. & Smoukov, S. K. “Self-shaping” of multicomponent drops. *Langmuir* **33**, 5696-5706 (2017).
- [167] Shimshick, E. J. & McConnell, H. M. Lateral phase separation in phospholipid membranes. *Biochemistry* **12**, 2351-2360 (1973).
- [168] Sidky, H. & Whitmer, J. K. Elastic response and phase behavior in binary liquid crystal mixtures. *Soft Matter* **12**, 4489-4498 (2016).
- [169] Ye, X., Zheng, C., Chen, J., Gao, Y. & Murray, C. B. Using binary surfactant mixtures to simultaneously improve the dimensional tunability and monodispersity in the seeded growth of gold nanorods. *Nano Lett.* **13**, 765-771 (2013).
- [170] Ahir, S. V., Tajbakhsh, A. R. & Terentjev, E. M. Self-assembled shape-memory fibers of triblock liquid-crystal polymers. *Adv. Funct. Mater.* **16**, 556–560 (2006).
- [171] Ohm, C., Morys, M., Forst, F.R., Braun, L., Eremin, A., Serra, C., Stanarius, R. & Zentel, R. Preparation of actuating fibres of oriented main-chain liquid crystalline elastomers by a wet spinning process. *Soft Matter* **7**, 3730–3734 (2011).
- [172] Xia, Y., Zhang, X. & Yang, S. Instant locking of molecular ordering in liquid crystal elastomers by oxygen-mediated thiol–acrylate click reactions. *Angew. Chem.* **130**, 5767-5770 (2018).
- [173] Krause, S., Dersch, R., Wendorff, J. H. & Finkelmann, H. Photocrosslinkable liquid crystal main-chain polymers: Thin films and electrospinning. *Macromol. Rapid Commun.* **28**, 2062–2068 (2007).
- [174] Seç, D., Čopar, S. & Žumer, S. Topological zoo of free-standing knots in confined chiral nematic fluids. Nature communications. *Nature Comm.* **5**, 1-7 (2014).
- [175] Orlova, T., Aβhoff, S. J., Yamaguchi, T., Katsonis, N. & Brasselet, E. Creation and manipulation of topological states in chiral nematic microspheres. *Nature Comm.* **6**, 1-9 (2015).
- [176] Posnjak, G., Čopar, S. & Muševič, I. Points, skyrmions and torons in chiral nematic droplets. Scientific reports. *Scientific reports* **6**, 26361 (2016).
- [177] Tran, L., Lavrentovich, M. O., Durey, G., Darmon, A., Haase, M. F., Li, N., Lee, D., Stebe, K. J., Kamien, R. D. & Lopez-Leon, T. Change in stripes for cholesteric shells via anchoring in moderation. *Phys. Rev. X* **7**, 041029 (2017).

- [178] Tran, L. & Bishop, K. J. M. Swelling cholesteric liquid crystal shells to direct the assembly of particles at the interface. *ACS Nano*. **14**, 5459-5467 (2020).
- [179] Krämmer, S., Vannahme, C., Smith, C. L., Grossmann, T., Jenne, M., Schierle, S., Jørgensen, L., Chronakis, I. S., Kristensen, A. & Kalt, H. Random-cavity lasing from electrospun polymer fiber networks. *Adv. Mater.* **26**, 8096-8100 (2014).
- [180] Gaio, M., Saxena, D., Bertolotti, J., Pisignano, D., Camposeo, A. & Sapienza, R. A nanophotonic laser on a graph. *Nature Comm.* **10**, 1-7 (2019).
- [181] Vigderman, L., Khanal, B. P. & Zubarev, E. R. Functional gold nanorods: synthesis, self-assembly, and sensing applications. *Adv. Mater.* **24**, 4811-4841 (2012).
- [182] Liu, Q., Tang, J., Zhang, Y., Martinez, A., Wang, S., He, S., White, T. J. & Smalyukh, I. I. Shape-dependent dispersion and alignment of nonaggregating plasmonic gold nanoparticles in lyotropic and thermotropic liquid crystals. *Phys. Rev. E* **89**, 052505 (2014).
- [183] Zhang, Y., Liu, Q., Muntoor, H., Yuan, Y. & Smalyukh, I. I. 2015. Metal nanoparticle dispersion, alignment, and assembly in nematic liquid crystals for applications in switchable plasmonic color filters and e-polarizers. *ACS Nano* **9**, 3097-3108 (2015).
- [184] Hauser, A. W., Liu, D., Bryson, K. C., Hayward, R. C. & Broer, D. J. Reconfiguring nanocomposite liquid crystal polymer films with visible light. *Macromolecules* **49**, 1575-1581 (2016).
- [185] Lee, C. H., Tian, L., Abbas, A., Kattumenu, R. & Singamaneni, S. Directed assembly of gold nanorods using aligned electrospun polymer nanofibers for highly efficient SERS substrates. *Nanotechnology* **22**, 275311 (2011).
- [186] Roskov, K. E., Kozek, K. A., Wu, W. C., Chhetri, R. K., Oldenburg, A. L., Spontak, R. J. & Tracy, J. B. Long-range alignment of gold nanorods in electrospun polymer nano/microfibers. *Langmuir* **27**, 13965-13969 (2011).
- [187] Zhang, C. L., Lv, K. P., Cong, H. P. & Yu, S. H. Controlled assemblies of gold nanorods in PVA nanofiber matrix as flexible free-standing SERS substrates by electrospinning. *Small* **8**, 648-653 (2012).
- [188] Liu, Y., Mills, E. N. & Composto, R. J. Tuning optical properties of gold nanorods in polymer films through thermal reshaping. *J. Mater. Chem.* **19**, 2704-2709 (2009).

- [189] Mahoney, C., Park, K., Jawaid, A., Kowalski, B., Gillman, A., Tondiglia, V., Treml, B., White, T. & Vaia, R. A. Low-energy, nanoparticle reshaping for large-area, patterned, plasmonic nanocomposites. *J. Mater. Chem. C* **6**, 7157-7169 (2018).
- [190] Han, X., Liu, Y. & Yin, Y. Colorimetric stress memory sensor based on disassembly of gold nanoparticle chains. *Nano Lett.* **14**, 2466-2470 (2014).
- [191] Fernández-López, C., Polavarapu, L., Solís, D. M., Taboada, J. M., Obelleiro, F., Contreras-Cáceres, R., Pastoriza-Santos, I. & Pérez-Juste, J. Gold nanorod–pnipam hybrids with reversible plasmon coupling: Synthesis, modeling, and sers properties. *ACS Appl. Mater. Interfaces* **7**, 12530-12538 (2015).
- [192] Shi, Y., Zhu, C., Li, J., Wei, J. & Guo, J. A color-changing plasmonic actuator based on silver nanoparticle array/liquid crystalline elastomer nanocomposites. *New J. Chem.* **40**, 7311-7319 (2016).